Brain-Derived Extracellular Vesicles for Applications in Psychiatry and Neurology

A thesis submitted by

Maia Norman

in partial fulfillment of the requirements for the degree of

PhD

in

Neuroscience

Tufts University

Graduate School of Biomedical Sciences

May 2023

Advisor: David R. Walt, PhD

Abstract

Progress in developing diagnostics and therapeutics for neurological and psychiatric conditions has lagged far behind other medical specialties. While this is due, at least in part, to the complexity of the brain, it also stems from an inability to access and assess the biochemistry of brain cells. Analysis of post-mortem brain tissue and the genome, in conjunction with animal, cell and organoid models, has yielded substantial progress. Still, neuroscientists lack the capability to track biochemical changes in living patients as they experience disease and as they respond to treatment. Developing noninvasive methods of sampling brain cells would fundamentally transform our ability to diagnose and treat neurological and psychiatric conditions.

One proposed strategy involves utilizing brain-derived extracellular vesicles (EVs). EVs are nanometer scale vesicles that bud from all cell-types and which contain proteins, RNA, lipids and other critical macromolecules that regulate cell function. EVs can be obtained from several easily accessible biofluids such as plasma, cerebrospinal fluid and urine, and have been used as markers of disease for conditions like prostate cancer. Before brain-derived EVs can serve as diagnostic markers, three major challenges must be overcome: EVs are present at low concentrations in peripheral biofluids and thus hard to detect; it can be challenging to separate EVs from contaminating proteins in complex biofluids; and immunocapture procedures must be validated to show that the EVs are coming from specific brain cells.

In this thesis, I describe how I developed methods for analysis and purification of EVs from complex biological fluids as well as techniques to evaluate candidate immunocapture markers for brain-derived EVs. I then conducted a comprehensive

analysis of targets proposed in the literature and demonstrate that many previously identified markers are in fact not EV-associated. On the other hand, CNPase, a marker of Oligodendrocytes and Schwann cells, is membrane-bound. Furthermore, I established methods for determining whether proteins are internal or external to EVs, a critical component in assessing the contents of cell-type-specific EVs. While substantial work remains before EVs can be used to diagnose neurological and psychiatric conditions, the methods developed herein may serve as a foundation for this burgeoning field.

Acknowledgements

First and foremost, I would like to thank my thesis advisor, Dr. David Walt for the incredible guidance he has provided during my PhD. Dr. Walt has been a mentor both personally and professionally. From my time as a rotation student, he challenged me to build my project around my interests, not his, and to pursue projects based on the real-world impact they would have for patients. My ability to formulate and test hypotheses has advanced tremendously due to his advice and support. On a personal note, working for Dr. Walt has been a joy. He was always there for me when an experiment failed or the research was challenging, and he would remind me of the importance of taking care of myself before taking care of the science. Finally, he could not have been more supportive as I started a family and had my first child, and for that I will be forever grateful.

I would also like to extend my gratitude to the chair of my thesis committee Dr. James Schwob, who has guided me through my journey towards academic medicine since my first CIBR, and my committee members Dr. Giuseppina Tesco and Dr. Joshua Kritzer. My committee meetings were always fun as we debated the recent data and considered various hypotheses and explanations. As my project shifted more towards technology development, I was excited to hear the suggestions of my committee members, each of whom brought a unique perspective. On the same note, I would like to thank my outside examiner, Dr. Clemens Scherzer for fruitful discussions about strategies for diagnosing neurodegenerative diseases. It was a pleasure getting to know you at PDBP meetings and discussing new ideas and directions for the field.

Science is an inherently collaborative effort, and I have had the true pleasure to work with incredible biologists, chemists and engineers during my time in the Walt Lab.

Specifically, I would like to thank 'Team Exosome': Dr. Dmitry Ter-Ovanesyan, Wendy Trieu and Roey Lazarovitz with whom I conducted the majority of the work described in this thesis. Through many late nights at the Wyss Institute we managed to accomplish a lot together, constantly learning from each other while also having a fair bit of laughs. I would also like to thank Dr. Tal Gilboa, Dr. Limor Cohen and Dr. Liangxia Xie for their friendship and mentoring. Even when they were not directly involved in the project at hand, we would spend hours debating ideas. No matter how busy they were, they would always take the time to explain concepts in chemistry and engineering or to look over my data. I am sure that what I learned from them both personally and professionally will guide me throughout my next steps.

I would also like to thank the funding sources that allowed the work in this thesis to be conducted: The National Institute for Neurological Diseases and Stroke, The Michael J. Fox Foundation, The Chan Zuckerberg Initiative, Good Ventures and The Massachusetts Consortium for Pathogen Readiness. The leadership at each of these organizations worked with us directly to facilitate the science and allow platforms for its dissemination through meetings, lectures and conferences. These forums gave me the opportunity to meet incredible scientists who would open my mind to new ways of thinking.

I want to thank the programs and institutions that have made my MD/PhD possible. First the amazing mentorship of the Tufts MSTP directors, Dr. James Schwob, Dr. Michael Chin and Dr. Gordon Huggins who provided immense support over the past seven years while constantly challenging me to think as a physician-scientist. Similarly,

the Neuroscience Department at Tufts which provided fantastic courses and learning opportunities over the past five years.

Most importantly, I want to thank my family. My parents have been an incredible source of love and support throughout my life. Any success I have had is a direct consequence of their investment in my development and growth, reminding me constantly to “think different”, and to do so in a way that would help others. I am so thankful I was able to attend school close to home and still make it to Friday night dinners with the family, reminding me what is really important in life. To Jon, my husband and partner in every aspect of life, I could never have done this without you. You are my love, my best friend and recently my best editor. It is a testament to your dedication and support that you know almost as much about Simoa and exosomes as I do. To Della, the greatest source of joy I could ever imagine, I know this thesis has taken some of mommy’s time, but please don’t let your first word be “exosome”.

Table of Contents

List of Figures

List of Tables

List of Copyrighted Materials Used

Norman M, Gilboa T, Ogata AF, Maley AM, Cohen L, Busch EL, Lazarovits R, Mao CP, Cai Y, Zhang J, Feldman JE, Hauser BM, Caradonna TM, Chen B, Schmidt AG, Alter G, Charles RC, Ryan ET, Walt DR. *Ultrasensitive high-resolution profiling of early seroconversion in patients with COVID-19.* Nat Biomed Eng. 2020 Dec;4(12):1180-1187. doi: 10.1038/s41551-020-00611-x. Epub 2020 Sep 18. PMID: 32948854; PMCID: PMC7498988.

Norman M, Gilboa T, Walt DR. *High-Sensitivity Single Molecule Array Assays for Pathological Isoforms in Parkinson's Disease.* Clin Chem. 2022 Mar 4;68(3):431-440. doi: 10.1093/clinchem/hvab251. PMID: 35064661.

Norman M, Ter-Ovanesyan D, Trieu W, Lazarovits R, Kowal EJK, Lee JH, Chen-Plotkin AS, Regev A, Church GM, Walt DR. *L1CAM is not associated with extracellular vesicles in human cerebrospinal fluid or plasma.* Nat Methods. 2021 Jun;18(6):631-634. doi: 10.1038/s41592-021-01174-8. Epub 2021 Jun 3. PMID: 34092791; PMCID: PMC9075416.

Ter-Ovanesyan D, Norman M, Lazarovits R, Trieu W, Lee JH, Church GM, Walt DR. *Framework for rapid comparison of extracellular vesicle isolation methods.* Elife. 2021 Nov 16;10:e70725. doi: 10.7554/eLife.70725. PMID: 34783650; PMCID: PMC8651285.

List of Abbreviations

AEB - Average Enzyme per Bead
AUC - Area Under the Curve
BDEV - Brain Derived Extracellular Vesicle
CI - Confidence Interval
COVID-19 - Coronavirus Disease 2019
CSF - Cerebrospinal Fluid
CV - Coefficient of Variation
DGC - Density Gradient Centrifugation
DNA - Deoxyribonucleic Acid
DLS - Dynamic Light Scattering
EDC - 1-Ethyl-3-(3-dimethylaminopropyl) carbodiimide
ELISA - Enzyme Linked Immunosorbent Assay
EM - Electron Microscopy
EST- Expressed Sequence Tags
EV - Extracellular Vesicle
GCV - Generalized Cross-Validation
GTEx - Genotype-Tissue Expression
IgG - Immunoglobulin G
iPSC - Induced Pluripotent Stem Cell
LLOQ - Lower Limit of Quantification
LOD - Limit of Detection
MS - Multiple Sclerosis
NAAT - Nucleic Acid Amplification Test
NC - Neurological Control
NDEV - Neuron Derived Extracellular Vesicle
NPV - Negative Predictive Value
NTA - Nanoparticle Tracking Analysis
PD - Parkinson's Disease
PPV - Positive Predictive Value
PTM - Post Translational Modification
RBD - Receptor Binding Domain
RGP - Resorufin ß-D-galactopyranoside
RNA - Ribonucleic Acid
ROC - Receiver Operator Characteristic
RT-PCR - Polymerase Chain Reaction with Reverse Transcription
RT-QuiC - Real-Time Quaking-Induced Conversion
SARS-CoV-2 - Severe Acute Respiratory Syndrome Coronavirus 2
SBG - Streptavidin- ß -galactosidase
SEC - Size Exclusion Chromatography
Simoa - Single Molecule Array
TRPS - Tunable Resistive Pulse Sensing
VI - Variable Importance

Chapter 1: Introduction

1.1 Challenges in diagnosing and monitoring neurological and psychiatric conditions

Progress in treating neurological and psychiatric diseases has lagged far behind maladies outside the central nervous system. There are many reasons for this, not least among them that the brain is a complicated organ. However, it is also because the brain is uniquely inaccessible for study in living patients. This creates several challenges. First, it is difficult to understand the underlying mechanism of diseases without access to the proteomic and transcriptomic changes that occur at onset and during progression. Second, in most diseases, after a therapy is administered, researchers can assess the change in the intended organ to evaluate the effects of the treatment. This allows researchers to surmise whether the treatment worked, and if it didn't, whether the failure was due to lack of accessibility to the organ, lack of target engagement at the intended organ, or lack of anticipated downstream effects. Finally, many neurological diseases are only diagnosed after substantial neurodegeneration has occurred, limiting our ability to effectively treat them. Having access to the underlying biochemistry of brain cells in living patients would fundamentally transform our ability to diagnose, manage and treat psychiatric and neurological diseases. In lieu of this access, we use surrogate measures to study the brain and provide clinical guidance.

1.1.1 How we currently learn about the brain

Our understanding of neurological and psychiatric diseases comes from diverse sources including neuroimaging, genetic sequencing, and analysis of postmortem brain tissue and cerebrospinal fluid. The insights gained from these techniques are then modeled in animals, induced pluripotent stem cells, and organoids. These models allow for an in-depth molecular understanding, which improves our ability to design therapeutic compounds with specificity, potency and efficacy. Below, I summarize how these techniques are used to enrich our understanding of brain diseases.

Neuroimaging methods are central to how we learn about spatial localization of brain diseases. Historically, neuroimaging techniques uncovered only structural brain abnormalities; however, as novel techniques are invented, the precision and diversity of what can be evaluated is increasing. These advances have had profound effects on the management of disease. For example, until the 1990s, many clinical trials for Multiple Sclerosis (MS) were conducted without finding any effect, likely because the long periods of relapse and remission made it difficult to quantitate differences between drug and placebo. However, once trials began to incorporate diffusion-weighted imaging, scientists could count the number of newly formed lesions and could thus clearly identify which drugs were having clinically significant effects[1]. The addition of diffusion-weighted imaging to clinical trials led to a plethora of drug approvals for MS, which now is a largely manageable condition. This example underscores how biomarkers can be key to transforming the lives of patients by enabling novel therapeutic development.

Recent advances in neuroimaging have also allowed for biochemical measurements with techniques such as Positron Emission Tomography (PET) tracers and

Magnetic Resonance Spectroscopy (MRS). These techniques detect changes in key neurotransmitters and proteins, which has been particularly useful in understanding certain psychiatric diseases. However, the specificity of these techniques does not permit in-depth analysis of biochemical changes in brain cells. Thus, while neuroimaging is furthering our knowledge of brain biology, we still lack an understanding of the molecular basis for most brain diseases.

With the advent of next-generation sequencing, Genome Wide Association studies (GWAS) proliferated. It was predicted that these studies would answer many of the open questions in the field and lead directly to treatments. However, we quickly learned that only a small fraction of the risk of developing diseases could be accounted for with genetic sequencing. This is likely because the majority of brain diseases are multifactorial, and changes in environment as well as epigenetic regulation play important roles. Consequently, GWAS have not yet become the molecular key to unlock neuropsychiatric treatments.

Biochemical assessment of post-mortem brain tissues has yielded major advances in our understanding of neurological and psychiatric diseases. For example, these analyses identified Lewy Bodies as the main pathological feature in Parkinson's Disease. Detailed biochemical analysis later showed differential protein modifications within these Lewy Bodies such as increased phosphorylation of alpha-synuclein at Serine 129, and this, in turn, has led to several proposed therapeutics. The primary limitation with post-mortem analysis is that it only illuminates the biochemistry of end-stage disease. For example, it is not known whether the change in phosphorylation of alpha-synuclein is causative to Lewy Body formation or protective of it. Without understanding the

biochemical changes that lead to the initial stages of disease, it will be challenging to identify therapies to stop disease or prevent it from progressing. An additional issue with analysis of post-mortem brain tissue is that there typically are substantial cell death processes taking place due to death of the donor, and it is difficult to isolate the processes that are disease-specific. While many important observations have been made using post-mortem biochemical assessment, the field is still in need of techniques that look at earlier stages of disease.

To obtain this earlier disease viewpoint, analysis of cerebrospinal fluid, the fluid encasing the brain, has been used. For some diseases this has led to useful insights and diagnostics. For example, cerebrospinal fluid analysis in patients with Creutzfeldt-Jakob Disease enables rapid identification of prions using a technique called Real-Time Quaking-Induced Conversion (RT-QuiC), which involves a fluorescence change in response to the presence of pathological PrP[2]. Recently, this technique was adapted to detect aggregated forms of alpha synuclein for diagnosis of Parkinson's Disease, Dementia with Lewy Bodies, and Multiple Systems Atrophy[3]. However, many of the changes seen in post-mortem tissue are not reflected in the Cerebrospinal Fluid (CSF). For example, since there are stark differences in phosphorylation states in post-mortem neurodegenerative disease patients compared to neurological controls, there has been a major effort to detect these same phosphorylation changes in the CSF. This effort has largely failed, though, as either no differences are seen, or change is seen in the opposite direction of what is observed in the brain. As a result of this discrepancy, it has been hypothesized that kinases and phosphatases present in the CSF are modifying the proteins after they leave the cell. Therefore, free fluids in which proteins can be modified and

mRNA is freely digested may not reflect underlying brain pathology. Furthermore, it is not possible to use CSF as a screening test for early diagnosis of these diseases because lumbar puncture is painful and carries risk of central nervous system infection. Accordingly, CSF is not an ideal option to identify important post-translational modifications or other important biochemical changes, nor is it possible to use for early diagnosis, which is critical for proper treatment.

Together the aforementioned techniques of neuroimaging, GWAS and analysis of post-mortem brain tissue and cerebrospinal fluid have led to important observations in neurological and psychiatric diseases. Many of these observations have been subsequently modeled in animals allowing for further mechanistic understanding of the biochemical changes. These animal models have been crucial in testing novel therapeutics, but they have limited utility due to substantial differences in the brains of animals relative to humans. Furthermore, it is challenging to assess psychiatric diseases such as anorexia and schizophrenia as constructs such as body image or hallucinations cannot be evaluated. Nonetheless these models have generated substantial advances in our understanding of receptors and pathways, which have helped elucidate mechanisms of disease and test therapeutic compounds.

Recently, as an alternative platform for drug discovery, induced pluripotent stem cells (iPSC) have become an area of great interest. In this technique, accessible cells such as fibroblasts or blood cells from patients and controls are cultured. Using a series of biochemical manipulations, these cells are induced to revert back to stem cell-like entities, from which they can be converted to neurons and other nervous system cell-types specific to the patient from whom they were derived[4]. This technique lets

researchers look at molecular differences between cultured neurons in individuals with and without specific diseases and see how they respond to therapeutic compounds. A recent improvement upon iPSC technology is brain organoids in which these individualized models are put in a 3D system with multiple CNS cell-types causing them to increasingly behave like they do in the individual's brain[4]. While these models may yield interesting insights, the conversion back to stem cells may not preserve the epigenetic changes that line the genome and may thus miss key environmental regulators of these disease processes.

1.1.2 Novel opportunities for understanding brain-based diseases

The techniques described above have led to important advances in our understanding of neurological and psychiatric diseases. However, many questions remain unanswered and novel tools are required for therapeutic target identification and disease diagnosis. One of the greatest needs is understanding the changes that occur early in disease processes. For example, there is still no consensus on whether amyloid-beta aggregation is central to the development of Alzheimer's Disease or whether it is simply a side effect of a different pathological feature[5]. This amyloid-beta hypothesis has been debated for many years as the aggregation of amyloid-beta into plaques is the main pathological feature in post-mortem AD brains, and yet dozens of trials targeting this process have shown little to no improvement in the pathology[6]. Identification of biochemical changes in the early stages of Alzheimer's Disease is still a critical need in neurology, and this paradigm applies to the majority of neurodegenerative diseases for which we still lack effective treatments.

Another major challenge in advancing novel therapeutics is determining if there is target engagement during clinical trials. It is often unclear whether a drug successfully penetrates the intended brain cell-type, and if it has the intended effect on its target or the intended downstream effect on disease. This lack of understanding of pathway engagement in the target cells makes it difficult to interpret why a given clinical trial failed and how to proceed in the next one[7]. Access to the biochemistry of these cells before, during, and after candidate drug administration will be key to improving clinical trial efficacy in neurological and psychiatric diseases.

Finally, it has been hypothesized that the failure of many trials is due to recruitment of individuals only after symptom onset when significant neurodegeneration has already occurred[8]. To truly stop neurodegeneration, it may be necessary to recruit pre-symptomatic individuals. However, to date, it has been difficult to validate tests that identify individuals who will develop neurodegenerative disease before symptom onset[7].

One strategy that has been proposed in recent years as a complementary method of noninvasively sampling the biochemical changes occurring in brain cells of living patients is to use Brain-Derived Extracellular Vesicles (BDEVs)[9]. However, many obstacles exist in utilizing these entities as a way of learning about the brain. Below, I introduce the biology of extracellular vesicles, detail the challenges of isolating and quantifying these vesicles, and survey the work that has been conducted using Brain-Derived Extracellular Vesicles.

1.2 Biology of Extracellular Vesicles

Extracellular vesicles (EVs) are nanometer scale compartments that bud off from all cell-types in the body. The term EV encompasses several vesicle types including

exosomes, microvesicles and apoptotic bodies[10]. Exosomes, which tend to be smaller in size, ranging from 30-100nm, are formed from the release of intraluminal vesicles in the endosomal system into the extracellular environment when the multivesicular endosome fuses with the plasma membrane[11]. Both the formation and contents of exosomes are primarily regulated by the ESCRT complex, a series of proteins that orchestrate the packing, budding and fusion processes[11]. Microvesicles, on the other hand are larger, ranging in diameter from 50-1000nm, and are formed from the outward budding and fusion of the plasma membrane[11]. This process of outward budding is highly regulated by a series of calcium-dependent enzymatic steps involving aminophopholipid translocases, scramblases and calpain[11]. Together these enzymes cause the physical bending of the membrane allowing for budding[11]. Finally, apoptotic bodies are released by dying cells into the extracellular environment due to increased hydrostatic pressure that occurs with cell contraction[10]. They range in size from 50 to 5000nm in diameter[10]. Due to the recycling of membrane-bound proteins between the plasma membrane and the endosomal system, all three of these vesicle types are enriched for transmembrane proteins. Some of these proteins are common across vesicles while others may be specific to the cell-type they originate from. CD9, CD63 and CD81, specifically, are members of the tetraspanin family and are enriched in EVs. Therefore, they are frequently utilized as 'EV markers' [10]. While the biogenesis of exosomes, microvesicles and apoptotic bodies are distinct, once they have been secreted from a cell it is generally not possible to distinguish their origin based on characteristics such as size or protein content due to substantial overlap. Accordingly, we use the term EV to account for all three species of vesicle.

EVs contain protein, nucleic acids and lipids[10]. The nucleic acid contents of EVs include both coding mRNA and noncoding species such as microRNA, in addition to DNA sequences[11]. While the content of exosomes and microvesicles is generally similar, apoptotic bodies can also contain intact organelles and chromatin[10]. The specific contents of EVs released by a given cell can be influenced by factors such as hypoxia, inflammation and glucose content[12,13]. This property makes them particularly useful in diagnosing disease and in monitoring changes after administration of potential therapeutic compounds.

Historically, EVs were believed to be a way for cells to dispose of unwanted materials. Recent research, however, has illuminated their role in cell-cell communication, cell maintenance, tissue repair and regeneration, tumor progression and stimulation of immune responses[10]. Once EVs are released from cells they can deliver their contents to recipient cells. This is accomplished either via endocytosis or via fusion with the plasma membrane, and it can produce functional changes in the recipient cell. This uptake, and its cell-type specificity, is believed to be mediated by receptors at the plasma membrane. However, the majority of EVs are still thought to be targeted to the lysosome for degradation[10].

The utility of EVs for diagnostic applications derives from the fact that they are secreted into accessible biofluids such as plasma, urine, semen, saliva, bronchial fluid, cerebral spinal fluid, breast milk, serum, amniotic fluid, synovial fluid, tears, lymph, bile, and gastric acid[10]. In order to be useful for these applications, EVs must be consistently isolated and rigorously characterized. Below, I describe current methods for isolation and analysis of EVs.

1.3 Methods in EV biology

The use of EVs for diagnostic purposes is challenging because EVs are found in biofluids at extremely low concentrations compared to abundant proteins such as albumin and immunoglobulins. Furthermore, EVs are heterogeneous both in their size and surface protein composition and overlap in size with other macromolecules such as lipoproteins and protein aggregates. This creates two related problems; it is difficult to quantify EVs, and it is hard to find efficient means of isolating them. Below, is a summary of current techniques used in the field of EV biology.

1.3.1 Techniques for EV Visualization, Quantification and Size Distribution Analysis

Due to their small size, most EVs fall below the diffraction limit of visible light and cannot be visualized with standard optical microscopy techniques. Instead, electron microscopy is the gold standard for visualizing EVs, enabling study of the distributions of their size and shape[14]. EM utilizes an electron beam to image nanoscale objects and encompasses two related techniques—scanning EM and transmission EM[15]. However, EM does not allow for quantitation of EVs in complex biofluids due to interference created by highly viscous and proteinaceous environments. Instead, to image EVs samples must be fixed and dried, making interpretation of the results complex. While EM is the gold standard for EV visualization, emerging technologies for this purpose now include atomic force microscopy and small angle X-ray scattering[14]. These novel techniques improve resolution, but still require the sample to be dried. Additionally, they are low-throughput and require highly specialized equipment and expertise, not available in most laboratories[15].

Optical techniques to analyze the number and size distribution of EVs include Dynamic Light Scattering (DLS) and Nanoparticle Tracking Analysis (NTA). DLS quantifies the size distribution of EV based on changes in light scattering intensity when a solution of EVs is illuminated by a laser beam[14]. However, the accuracy of DLS in biological fluids has been called into question because the technique works well only for relatively monodispersed size distributions, due to assumptions made to input into the mathematical models used. The requirement for monodispersity, a property that does not apply to the complex biological fluids, restricts the utility of DLS[15]. The technique also cannot distinguish EVs from lipoproteins and protein aggregates, which is a further constraint.[14].

NTA uses conventional microscopy to assess individual particles via illumination with a laser beam and relies on analysis of Brownian motion in a static solution. However, because NTA analyzes particles on an individual not averaged basis, it can analyze polydisperse samples[15]. Nonetheless, this technique cannot distinguish EVs from lipoproteins and protein aggregates and thus has low utility in complex biological fluids[14]. Furthermore, NTA does not quantify vesicles smaller than 50 nm in diameter, which excludes a portion of the EV population, specifically exosomes.[14].

Tunable resistive pulse sensing (TRPS) is an electrical method for analysis of EV quantity and size distribution. TRPS detects EVs by measuring the change in electrical current as particles pass through a nanopore. The decrease in current is proportional to the volume of the particle passing though[15]. While this technique is highly accurate in pure samples, its utility in biological samples is minimal as the pore can easily be clogged by larger particles.

Flow Cytometry simultaneously analyzes light scattering and performs fluorescence measurements on individual particles by illumination with a laser beam[14]. Light scattering can determine the size and shape of EVs. However, size estimates of particles are thought to be less accurate and limited to EVs of diameter greater than 100nm for high resolution flow cytometers and 500nm for conventional flow cytometers[15]. Smaller EVs are detected collectively and can be counted as one large EV thus hampering the quantitation of EVs[15]. This technique can also simultaneously label surface markers and measure particle size, which may be important for cell-type specific EV analysis.

While DLS, NTA and TRPS can all determine particle counts, unlike surface protein-based measurements they do not distinguish between EVs and other abundant molecular entities such as lipoproteins and protein aggregates. Methods for identifying EV specific proteins include dot blot, Western blot and ELISA[15]. All three rely upon antibodies to identify both surface and cytosolic proteins, which means they require rigorous validation of non-specific binding to ensure proper quantification. Of these techniques, only Western blot verifies protein size, which provides additional confidence in the measurement. Nonetheless, the use of two antibodies in a sandwich Enzyme Linked Immunosorbent Assay (ELISA) format gives the highest target specificity and is therefore the most quantitative of the protein-based measurement methods. Because many of the surface proteins that characterize EVs, such as tetraspanins (CD9, CD63 and CD81), are also present on cells, samples must be carefully purified to remove cells for accurate quantification. An important caveat in this quantification method is that some

EVs have only some of the markers depending on the cell-type they came from, and some may have none at all[15].

The above methods were primarily optimized for use in EV analysis of cell culture. Consequently, each has shortcomings in quantifying EVs in complex biological fluids. Specifically, they are inadequate when EVs are present at low concentrations, as is the case in fluids such as CSF. Therefore, there is still a need therefore to develop accurate methods for quantification of EVs when they are present in low quantities in complex biological samples, which is a major focus of the experiments in Chapters 2 and 3 of this thesis.

1.3.2 EV Isolation

Several techniques have been developed to isolate EVs from biological samples. These techniques rely on properties of EVs such as their size, density and the protein content of their membrane. The choice of optimal isolation method largely depends upon the complexity of samples in use and the needed purity level for the intended downstream application. Below I describe the main techniques currently used for EV isolation.

Differential Ultracentrifugation separates EVs based on size and density[16]. With this method, a series of centrifugation steps are taken. First, low speed centrifugation in the range of several hundred to 2000 g removes particles with high buoyant densities like cells and cell debris. Next, a ~10,000 g step clears large apoptotic bodies. Finally, centrifugation at >100,000 g for more than two hours is used to pellet the EVs and discard the remaining supernatant [17]. This last step can be repeated for increased purity of EVs. Specific protocols for EV isolation vary widely in the number of steps and the speed

and duration of each step, generating differences in reported yield and purity of EVs. Of note, ultracentrifugation is particularly useful when collecting EVs from cell culture or urine, as it allows for the concentration of the sample from a large volume. On the other hand, EV sedimentation efficiency is lower in viscous samples like plasma and serum, necessitating higher centrifugation speeds and yielding low purity preparations[17]. However, in any sample, the co-sedimentation of protein aggregates, lipoproteins and other non-EV particles is the main disadvantage of ultracentrifugation.

Density Gradient Centrifugation increases the efficiency of EV separation. In this technique the sample is loaded either on the top or bottom of a sucrose or iodixanol gradient and centrifuged at speeds >100,000 g for ten or more hours. DGC works on the principle of buoyant density, and unlike differential ultracentrifugation has very little contamination of protein aggregates or lipoproteins in the EV fraction. DGC is both the highest purity and lowest yield technique in EV biology and is used primarily for research purposes when highly pure samples are necessary[17]. A major disadvantage of centrifugation-based methods (both ultracentrifugation and density gradient centrifugation) is that they require many hours in an ultracentrifuge where only a handful of samples can be processed at a time. These techniques are therefore not feasible for large-scale biomarker discovery or for use in clinics.

Ultrafiltration relies on low-speed centrifugation through a filter of a given pore size. This method has been used in the literature for EV isolation[17]. However, research has demonstrated that while this technique is excellent for concentrating EV samples, an important step in downstream analysis, the technique does not efficiently separate EVs

from contaminating proteins and therefore should only be used in conjunction with other purification techniques.

Size Exclusion Chromatography (SEC), also known as Gel Filtration, uses a resin (usually Sepharose) to efficiently separate EVs from smaller contaminating proteins. For this reason, it has become the preferred method in complex and viscous biological samples such as plasma. Due to the need to first concentrate EVs, it is less commonly used in cell culture and urine. Furthermore, unlike centrifugation-based techniques, EVs isolated by SEC maintain their integrity and biological activity[17]. Many important parameters can influence the purity and yield of SEC including column dimensions, gel utilized, elution buffer and the viscosity and volume of the loaded sample. Thus, the best protocol is determined by the yield and purity needed for downstream applications, and this must be carefully optimized. Unlike centrifugation-based methods, SEC can readily be scaled up and automated for large-scale biomarker discovery and clinical use. However, it is important to mention that this technique does not provide good separation from some lipoprotein species, which may interfere with downstream analysis.

Precipitation-based methods for EV isolation include the use of hydrophilic polymers such as PEG. This method, which relies on the decreased solubility of EVs in a solution of hydrophilic polymers, has increased in popularity due to ease of use and because a large number of samples can be processed simultaneously[17]. However, the main disadvantage is the coprecipitation of non-EV particles including proteins, lipoproteins and viruses.

Finally, immunoprecipitation relies on immunocapture of specific surface proteins on EVs in order to pull them out of a biological fluid. This method is especially useful for

isolating cell-type- or disease-specific EVs but can also be used to capture total EVs with common markers such as the tetraspanins[17]. Generally, this procedure involves attaching antibodies or aptamers to magnetic beads or other solid resins and introducing the sample of interest for an incubation period of several hours. Subsequently, many wash steps must be performed to remove nonspecifically bound particles. While this technique is useful, particularly for cell-type-specific isolation, several caveats are important to address. First, the resins in use may nonspecifically bind proteins-- for this reason control antibodies are used. Second, this technique uses only a single antibody for immune isolation, which may result in nonspecific binding of the antibody to other targets. Thus, careful validation of immunoprecipitation techniques is necessary for proper interpretation of downstream data.

Ultimately, the choice of isolation technique is dependent upon the purity and yield required for downstream analysis as well as the biofluid in use. High-throughput analysis of these methods is the focus of chapter 2 of this thesis.

1.4 Single Molecule Array Technology for EV quantification

EVs exist at extremely low quantities in accessible biological fluids, and the internal protein content of EVs is low. In order to quantify and analyze proteins that are either on the membrane or internal to EVs, it is necessary to utilize analytical technologies that can achieve femtomolar and even attomolar detection limits. This is particularly essential when evaluating BDEVs that are thought to be only a fraction of total EVs in biological fluids such as plasma. In this thesis work, I utilize a technology called single molecule arrays (Simoa) invented in our laboratory in order to achieve the

sensitivity needed to detect EV proteins. Simoa is the main technique used throughout the remainder of this thesis, and the theoretical underpinnings that enable its use are described below.

Simoa technology makes use of a sandwich enzyme-linked immunosorbent assay (ELISA) format in which an immobilized antibody is used to capture the target of interest and a biotinylated detection antibody is used for labeling[18]. The biotinylated detection antibody binds streptavidin-labeled beta-galactosidase which cleaves resorufin-beta-D-galactopyranoside (RGP) to produce a fluorescent product. Unlike traditional ELISA, Simoa uses a bead-based format in which the capture antibody is conjugated to a 2.7μm diameter paramagnetic bead and the beads are isolated in 216,000 wells, each of which can fit only a single bead[19]. Thus, only when the target of interest is present will there be a full immunocomplex and therefore a beta-galactosidase enzyme present in a given well. The beads are loaded into the wells along with the substrate RGP and sealed with oil. Due to the small size of the microwells (40 femtoliters), a single beta-galactosidase enzyme molecule is able to produce high local fluorescence, which can be easily imaged[18]. In contrast, the same single immunocomplex would not be detectable if the volume of the well were instead dozens of microliters as is the case in a traditional ELISA. This digitized technique therefore allows us to count the individual number of molecules in solution and reach 100-1000-fold higher sensitivity compared to traditional ELISA.

Simoa technology relies on the assumption that each bead has either zero or one target molecules per bead. This is achieved by using a large excess of beads (500,000) compared to the number of target molecules in solution. Thus, the percentage of beads

containing an immunolabeled complex will follow a Poisson distribution. When the concentration of analyte exceeds this low concentration, Poisson statistics cannot be assumed, and we therefore can no longer count molecules. At these high concentrations, we switch to looking at overall fluorescence as in a traditional ELISA. The ability to switch between a digital and non-digital reading within the same assay ensures that we can not only achieve the sensitivity to measure EVs and their contents, but also have a wide dynamic range for higher concentration analytes.

Imaging of resorufin takes place at 574nm excitation and 615nm emission at two timepoints separated by a 30 second interval. The difference between these images is used to quantify the fluorescence in a given well. This reduces background signal by negating the effect of spontaneous RGP conversion enabling us to identify active wells containing an enzyme molecule. The fraction of beads with at least one bound enzyme is known as the fraction on (f_{on}) while the intensity of each well is the I_{bead}. At low concentrations of analyte, f_{on} is used to calculate the average number of enzymes per bead (AEB), while at high concentrations of analyte, when Poisson statistics no longer govern the distribution of enzymes per bead, I_{bead} is used.

In addition to images taken at 574/615nm for resorufin fluorescence, four other wavelengths are captured to identify beads with conjugated fluorescent dyes. In a multiplexed Simoa assay, different capture antibodies for different analytes are each conjugated to beads with a specific fluorescent dye enabling decoding of which analyte is present in each microwell. This procedure, which was originally performed manually, has now been automated in the Quanterix HD-X system. All of the work described herein was performed in this automated fashion.

1.5 Do EVs cross the BBB?

The idea that brain-derived EVs can be isolated in the plasma relies on the assumption that EVs cross the blood brain barrier (BBB). The BBB is a complex structure of tight junctions formed by endothelial cells, pericytes and astrocytic end feet[20]. It is further interconnected with neuronal endings as well as microglia. The BBB is responsible for controlling access in and out of the central nervous system[20]. This collection of cells forms a homeostatic mechanism that mediates the influx of molecules necessary for brain function and outflux of CNS waste products[20]. However, this highly regulated functional unit is disrupted in several neurodegenerative diseases as well as cancer[20,21]. Under physiological conditions, there are five main mechanisms by which molecules are transported across the BBB. These include paracellular (transport between endothelial cells), transcellular diffusion (transport through the cytosol of BBB cells), protein mediated transport (selective carriage of essential nutrients), receptor mediated transcytosis (initiated by ligand binding) and adsorptive-mediated transcytosis (triggered by electrostatic interactions)[22]. The use of peripherally immunocaptured, brain-derived EVs relies on the assumption that EVs can use one of the above mechanisms to escape the CNS.

Evidence from both in vivo and invitro models suggests that EVs do cross into the CNS from the periphery[23]. In several studies, when EVs from cultured cell lines are injected peripherally, a small percentage, between 0.5-2%, accumulates in the brain[9]. Similarly, when siRNA, mRNA or microRNA are packaged into EVs and administered peripherally, they can be shown to exert an effect in brain tissue[24,25]. One caveat is that some of these studies use Rabies Virus ligands in order to guide these EVs to the brain,

which would not occur in physiological transfer. Nonetheless, even when there is no manipulation to the EVs, uptake into the CNS is seen. Thus, it is likely that under physiologic conditions EVs can cross into the CNS.

Evidence that EVs travel from the CNS into the periphery is less substantiated. Glioblastoma-specific mRNA has been sequenced in EVs collected peripherally in patients[26]. However, it is known that glioblastoma causes damage to the BBB[27]. Additional corroboration comes from injecting EVs into brain parenchyma in animal models, which can later be detected in plasma[9,27]. However, in this case the injection itself disrupts the BBB and therefore cannot be considered definitive proof. Thus, while current evidence hints at the likelihood of EV transport both into and out of the CNS, conclusive experiments still need to be performed. Models that use genetic manipulation to selectively express proteins in specific brain regions without surgical intervention will be key to answering these questions in the coming years, as they will be able to rule out an impaired blood brain barrier as a cause for EV transfer.

1.6 A historical review of Brain-Derived Extracellular Vesicles in peripheral blood

1.6.1 Neuron-Derived Extracellular Vesicles

Neurons are the main functional unit of the nervous system, storing information in their network of connections. Their dysfunction underlies myriad psychiatric and neurological conditions and accordingly has been the primary focus of BDEV isolation to date. In 2014, a pair of studies claimed to immuno-capture EVs derived from neurons in blood samples[28,29]. Both of these studies burst the EVs and found differences in disease-associated proteins between a patient cohort and a corresponding control group. One

study utilized the handle NCAM and compared Alzheimer's Disease patients to neurological controls while the other used L1CAM for Parkinson's Disease. These papers led to an explosion of research that mimicked these techniques utilizing either NCAM[29,30], L1CAM [9,28-71] or more recently GluR2[72-74] as a handle for neuron-derived EV (NDEV) immunocapture. Generally, the intent was to identify differences between neurological or psychiatric diseases or between these diseases and controls. These investigators utilized these putative NDEVs to learn about the underlying mechanisms behind Alzheimer's Disease[29,30,34], Mild Cognitive Impairment[29], Parkinson's Disease[28], Traumatic Brain Injury[39], HIV-associated neurocognitive disorder[32], Post-operative delirium patients[67], Bipolar Depression[65], Schizophrenia[58], Substance use Disorders[64], Amyotrophic Lateral Sclerosis[59], Frontotemporal Dementia[34], Restless Leg Syndrome[48] and Multiple Sclerosis[75]. Other studies sought to diagnose the aforementioned conditions by identifying differences in proteins or nucleic acids between groups[28,29,59]. A minority even looked at changes before and after treatments in order to monitor treatment engagement for clinical trials[61]. While the vast preponderance involved protein biomarkers, some researchers also interrogated differences in microRNAs[53,59,69,76].

These manuscripts acknowledge that NCAM and L1CAM are produced peripherally, but they assume that the captured EV content is, at a minimum, enriched for brain and specifically neuron-derived protein content. However, they often reference each other as evidence that NDEVs cross the BBB and can be immunocaptured. Chapter 3 of this thesis describes how I evaluated the claims made specifically about the use of L1CAM for NDEV immunocapture while chapter 4 describes how I evaluated the claims about NCAM and GLUR2.

1.6.2 Oligodendrocyte-Derived Extracellular Vesicles

Oligodendrocytes are the myelinating cells of the central nervous system. They wrap around individual neuron axons in order to increase the conduction velocity and enable action potentials to quickly propagate. In the peripheral nervous system, Schwann cells myelinate peripheral neurons; however, unlike oligodendrocytes, a single Schwann cell can myelinate many neurons. Several disorders of the central and peripheral nervous system, such as Multiple Systems Atrophy and Multiple Sclerosis, are due to disfunctions of these cell-types. In order to diagnose and better treat these disorders, some investigators have proposed capturing oligodendrocyte-derived EVs in plasma. These papers used either MOG[77] or CNPase[78] as handles for immunocapture. In chapter 4 of this thesis, I evaluate the claims made about MOG and CNPase as possible immunocapture targets for oligodendrocyte-derived extracellular vesicles.

1.6.3 Astrocyte-Derived Extracellular Vesicles

Astrocytes are support cells of the brain that play an important role in homeostatic functions and whose dysregulation has been implicated in several psychiatric and neurological disorders. To study this disfunction in Alzheimer's Disease, a pair of studies used the astrocyte cell surface marker GLAST to immunocapture astrocyte-derived EVs in plasma[33,79]. In chapter 4 of this thesis, I attempt to evaluate the claims made about GLAST; however, due to insufficiently avid antibodies, I was ultimately not able to conclude whether GLAST is an effective immunocapture target.

1.6.4 The need for rigorous evaluation of claims about BDEVs

Over 60 publications have made quantification claims regarding proteins and nucleic acids within BDEVs. During my thesis research, I attempted to replicate the work from these publications in order to build upon it. My goal was to develop blood-based, early diagnostics for Parkinson's Disease (PD) using BDEVs. However, an early set of experiments demonstrated clearly that there were fundamental flaws with the prevailing literature and the necessary analytic methods to rigorously evaluate such claims did not exist. The focus of my thesis subsequently became the development of tools for EV isolation, quantification and identification of *bona fide* BDEV immunocapture targets. In the next several chapters, each of which is a manuscript submitted for publication, I describe the development of methods, propose a framework for evaluating BDEVs, and chart a roadmap for their successful use in diagnostic applications for psychiatric and neurological disease.

Chapter 2: Comparison of Extracellular Vesicle Isolation Methods from Human Biofluids using Single Molecule Arrays[1]

[1] Ter-Ovanesyan D, Norman M, Lazarovits R, Trieu W, Lee JH, Church GM, Walt DR. 2021. Elife. 10:e70725.

Reprinted here with permission from publisher.

2.1 Introduction

EVs are released by all cell-types and are found in biofluids such as plasma and CSF. EVs contain contents from their donor cells, providing broad non-invasive access to molecular information about cell-types in the human body inaccessible to biopsy [80]. Despite the diagnostic potential of EVs, there are several challenges that have hampered their utility as biomarkers. First, EVs are heterogeneous and difficult to quantify [15,81]. Second, EVs and their contents are present at low amounts in clinically relevant samples [82]. Finally, there is a lack of consensus about the best way to isolate EVs from biofluids [83].

Several techniques have been used in attempts to quantify EVs. These methods, such as NTA, DLS, and TRPS, aim to measure both particle size and concentration [15]. A major limitation of these methods is that they cannot discriminate lipoproteins or particles of aggregated proteins from EVs [83]. Since biofluids, and plasma in particular, contain an abundance of lipoproteins and protein aggregates at levels higher than those of EVs [84,85], these methods are ill-suited for quantifying EVs [81]. Lipid dyes have also been used to label and measure EVs [86,87], but these dyes also bind to lipoproteins and lack sensitivity [81]. A feature of EVs that distinguishes them from both lipoproteins and free protein aggregates is the presence of transmembrane proteins that span the phospholipid bilayer [84]. The tetraspanins CD9, CD63, and CD81 are transmembrane proteins that are widely expressed and readily found on EVs, often referred to as "EV markers" [81]. Although there is not one transmembrane protein present on all EVs, simultaneously measuring several highly expressed proteins in a sample should minimize the possibility that a rare subset of

EVs is being analyzed. Therefore, measuring the three tetraspanin markers should be reliable proxy for EV abundance in many contexts.

Our lab has previously developed single molecule array (Simoa) technology, now commercially available, which converts the enzyme-linked immunosorbent assay (ELISA) into a digital readout by distributing single protein-antibody complexes into femtoliter wells [88]. Simoa assays can be 100 to 1000 times more sensitive than traditional ELISAs [89], which is essential for EV analysis. The levels of EV proteins are often low in clinical samples and undetectable using conventional techniques [90]. We developed Simoa assays EVs by immuno-isolating and detecting EV transmembrane proteins (CD9, CD63, and CD81) in microwell arrays. We previously used these assays, as well as a Simoa assay for the putative neuron-derived EV marker, L1CAM, to show that L1CAM is not associated with EV-containing fractions by SEC or DGC [88].

Simoa can count individual antigen-positive vesicles with a specific transmembrane protein, and concentration can be calculated by mapping the ratio of "on wells" to "off wells" against a calibration curve of recombinant protein. Thus, we reasoned that Simoa could be used to compare EV capture efficiency between different EV isolation methods. In this study, we demonstrate the application of Simoa for relative EV quantification by comparing different EV isolation methods from human biofluids. We compared three of the most commonly used isolation techniques: ultracentrifugation, precipitation, and SEC. By measuring levels of albumin using Simoa, we were also able to determine the relative purity for each technique in the same experiment. These comparisons were enabled by Simoa's high sensitivity, wide dynamic range, and high-throughput capabilities. We were then able to use Simoa assays to develop improved SEC

protocols for EV isolation in plasma and CSF, demonstrating the utility of Simoa for EV quantification and analysis in biological fluids.

2.2 Methods

2.2.1 Human Sample Handling

Pre-aliquotted pooled human plasma and CSF samples were ordered from BioIVT. The same pools were used for all main figures throughout the paper in order to ensure comparable analysis of methods. For all EV isolation technique comparisons, one 0.5 mL sample was used for each isolation method. Plasma or CSF was thawed at room temperature. After sample thawing, 100X Protease/Phosphatase Inhibitor Cocktail (Cell Signaling Technology) was added to 1X. The sample was then centrifuged at 2000 x *g* for 10 minutes. The supernatant was subsequently centrifuged through a 0.45 μm Corning Costar SPIN-X centrifuge tube filter (Sigma-Aldrich) at 2000 x *g* for 10 minutes to get rid of any remaining cells or cell debris.

2.2.2 Simoa Assays

Simoa assays were developed and performed as previously described [88]. Capture antibodies were coupled to Carboxylated Paramagnetic Beads from the Simoa Homebrew Assay Development Kit (Quanterix) using EDC chemistry (Thermo Fisher Scientific). Detection antibodies were conjugated to biotin using EZ-Link NHS-PEG4 Biotin (Thermo Fisher Scientific). The following antibodies were used as capture antibodies for tetraspanins: ab195422 (Abcam), MAB5048 (R&D Systems), and ab79559 (Abcam). The

following antibodies were used as detector antibodies for tetraspanins: ab58989 (R&D Systems), 556019 (BD) and 349502 (BioLegend).

For albumin, DY1455 (R&D Systems) was used as both capture and detector antibody. The following recombinant proteins were used for CD9, CD63, CD81, and albumin: ab152262 (Abcam), TP301733 (Origene), TP317508 (Origene), ab201876 (Abcam).

On-board dilution was performed with 4X dilution for each of the tetraspanins, while manual 20X dilution was used for albumin. All samples were raised to 160 μL per replicate in sample diluent. For tetraspanin assays, samples were incubated with immunocapture beads (25 μL) and biotinylated detection antibody (20 μL) for 35 minutes. Next, six washes were performed, and the beads were resuspended in 100 μL of Streptavidin labeled β-galactosidase (Quanterix) and incubated for 5 minutes. An additional six washes were performed, and the beads were resuspended in 25 μL Resorufin β-D-galactopyranoside (Quanterix) before being loaded into the microwell array on the Quanterix HD-X instrument.

For the albumin assay, samples were incubated first with immunocapture beads (25 μL) for 15 minutes and then washed six times. Subsequently, 100 μL detection antibody was incubated with the beads for 5 minutes. Next, six washes were performed, and the beads were resuspended in 100 μL of Streptavidin labeled β-galactosidase (Quanterix) for a final 5 minute incubation. After an additional six washes, the beads were resuspended in 25 μL Resorufin β-D-galactopyranoside (Quanterix) and then loaded into the microwell array on the Quanterix HD-X instrument.

2.2.3 Preparation of Custom SEC Columns

The resins Sepharose CL-2B, Sepharose CL-4B, and Sepharose CL-6B (all from GE Healthcare/Cytiva) were washed in PBS. The volume of resin was washed with an equal volume of PBS in a glass container and then placed at 4 °C in order to let the resin settle completely (several hours or overnight). The PBS was then poured off, and an equal volume of PBS was again added two more times for a total of three washes. Columns were prepared fresh on the day of use. Washed resin was poured into an Econo-Pac Chromotography column (Bio-Rad) to bring the bed volume (the resin without liquid) to 10 mL or 20 mL. When the desired amount of resin filled the column and the liquid dripped through, the top frit was immediately placed at the top of the resin without compressing the resin. PBS was then added again before sample addition.

2.2.4 Collection of Size Exclusion Chromatography Fractions

Once prepared, all columns were washed with at least 20 mL of PBS in the column. Immediately before sample addition, the column was allowed to fully drip out and, after last drop of PBS, sample (filtered plasma or CSF) was added to the column. As soon as sample was added, 0.5 mL fractions were collected in individual tubes. As soon as the plasma or CSF completely entered the column (below the frit), PBS was added to the top of column 1 mL at a time. Fraction numbers correspond to 0.5mL increments collected as soon as sample is added. For Izon and 10 mL columns, fractions 6-21 were collected (since first few fractions correspond to void volume). For 20 mL columns, fractions 12-27 were collected (since void volume is larger for 20 mL columns than 10 mL columns).

2.2.5 Ultracentrifugation

Samples of filtered 0.5 mL plasma or CSF were added to 3.5 mL Open-Top Thickwall Polycarbonate ultracentrifuge tubes (Beckman Coulter), and PBS was added to fill tubes to the top. Samples were ultracentrifuged at 120,000 x *g* for 90 minutes at 4 °C in an Optima XPN-80 ultracentrifuge (Beckman Coulter) using a SW55 Ti swinging-bucket rotor (Beckman Coulter). Afterwards, all supernatant was aspirated. Pellets were resuspended in PBS for the "Ultracentrifugation" condition. For the "Ultracentrifugation with wash" condition, the ultracentrifuge tubes were filled to the top with PBS, and samples were ultracentrifuged again at 120,000 x *g* for 90 minutes. Supernatant was then aspirated, and pellets were resuspended in 500 uL PBS. For all ultracentrifugation samples, isolation was performed on two separate days and then resulting Simoa values were averaged.

2.2.6 ExoQuick & ExoQuick ULTRA

Samples of plasma or CSF were mixed with ExoQuick Exosome Precipitation Solution (System Biosciences) or ExoQuick ULTRA EV Isolation Kit for Serum and Plasma (System Biosciences), and protocols were performed according to manufacturer's instructions. For ExoQuick, 0.5 mL of plasma or CSF was mixed with 126 uL of ExoQuick and incubated at 4 °C for 30 minutes, followed by centrifugation at 1500 x *g* for 30 minutes. Supernatant was removed, and samples were centrifuged at 1500 x *g* for an additional 5 minutes. Residual supernatant was removed, and pellets were resuspended in 500 uL PBS. For ExoQuick ULTRA, 250 uL of plasma or CSF was used in accordance with instructions, and Simoa values were corrected by multiplying by two to match 0.5

mL volume used for other samples. For each sample, 500 uL of EVs was eluted per column. For all precipitations, isolation was performed on two separate days and then resulting Simoa values were averaged.

2.3 Results

2.3.1 EV analysis using Simoa

We employed Simoa technology, an ultrasensitive digital ELISA, as a novel platform for EV quantification. Although Simoa is generally used to quantify free proteins, we applied Simoa to EVs by immuno-isolating single vesicles into microwell arrays labeled with antibodies to transmembrane proteins on the EV surface. As in conventional ELISA, Simoa uses two antibodies: a capture antibody conjugated to a magnetic bead, and a detector antibody that is labeled with an enzyme creating a fluorescent product. Because EVs have more than one copy of each protein molecule on their surface, the detector antibody can be either the same protein as the capture antibody, or another protein on the same vesicle. Unlike traditional ELISA, individual immuno-complexes are isolated into femtoliter wells that fit only one bead per well. In a given sample, there are many more antibody-bound beads than target proteins, and therefore Poisson statistics dictate that only a single immuno-complex is present per well in the vast majority of wells. This allows counting "on wells" as individual protein molecules, or, in the case of EVs, antigen-positive vesicles (Figure 2.1a) for markers such as CD9, CD63, or CD81. We previously developed Simoa assays for these proteins and showed that they are one to three orders of magnitude more sensitive than the corresponding standard ELISA assays with the same pairs of antibodies [88].

2.3.2 Application of Simoa for comparison of existing EV isolation methods

We used Simoa to directly compare EV isolation from 0.5 mL samples of human plasma and CSF using commonly used EV isolation methods. For each method, we used identical samples of plasma or CSF that were pooled and aliquotted, allowing us to directly compare the different methods. To separate EVs from cells, cell debris, or large vesicles, all samples were first centrifuged and then filtered through a 0.45 μm filter. We compared ultracentrifugation (with and without a wash step), two commercial precipitation kits (ExoQuick and ExoQuick ULTRA), and two commercially available SEC columns (Izon qEVoriginal 35nm and 70nm). SEC separates EVs from free proteins based on size; proteins enter porous beads and elute from the column later than the EVs, which are much larger and less likely to enter the beads (Figure 2.1b). Whereas the ultracentrifugation and precipitation conditions each yielded a single sample, for the SEC conditions, we collected several fractions and analyzed each fraction to assess the distribution of EVs relative to albumin.

We were able to quantify EVs by measuring the levels of CD9, CD63, and CD81 across the different EV isolation methods in both plasma and CSF (Figure 2.1c). Since we are interested in all EVs as opposed to subsets with a specific marker, we quantified EV yield by averaging the levels of the three tetraspanins. We first used the Simoa measurement (in picomoles, determined relative to a corresponding recombinant protein standard) to calculate EV recovery for each individual marker by normalizing the level of tetraspanin in each condition to the amount of that tetraspanin in fractions 7-10 of the Izon qEV 35nm SEC column (the condition with highest EV levels in plasma). Next, we

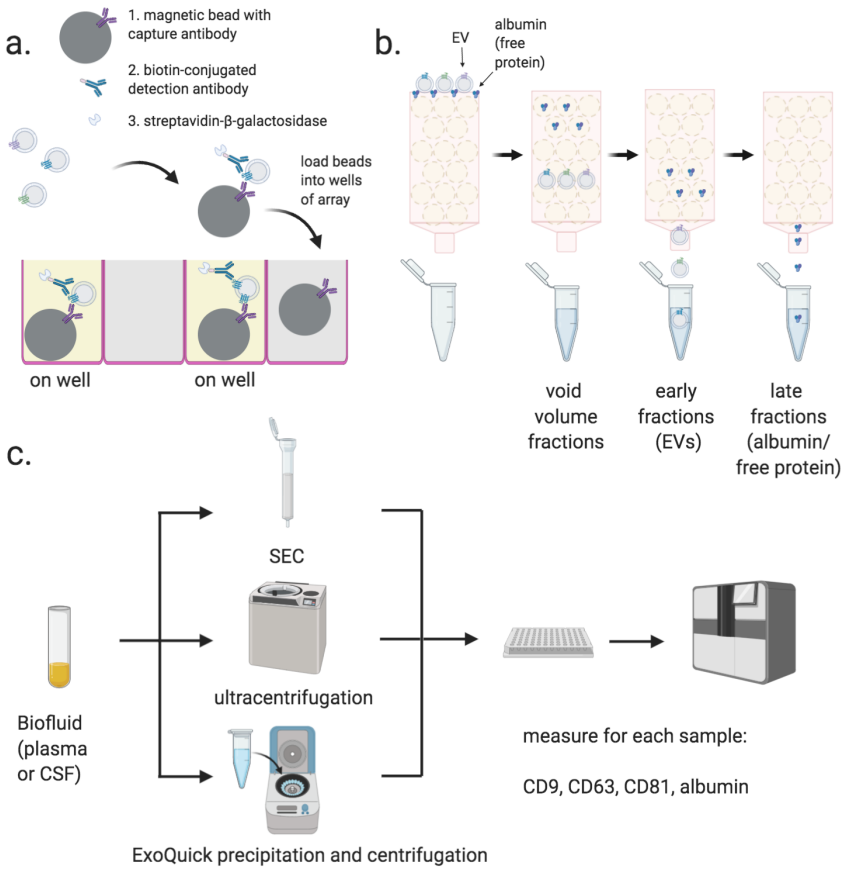

Figure 2. 1 Overview of EV detection using Single Molecule Arrays (Simoa) and experimental design

a. Single immuno-complexes are formed by binding the target tetraspanin protein on EVs to a magnetic bead conjugated to a capture antibody and a biotin-labeled detection antibody. Detection antibodies are then labeled with a streptavidin-conjugated enzyme. The beads are then loaded into individual wells of a microwell array where each well matches the size of the magnetic bead limiting a maximum of one bead per well. Wells with the full immuno-complex produce fluorescent signal upon conversion of substrate. Wells that are "on" are then counted by fluorescence imaging. In the case of detecting transmembrane proteins such as tetraspanins, an immuno-complex can be formed by capture and detection antibodies binding to either the same individual protein or to different tetraspanin proteins on the same EV.
b. EV and free proteins such as albumin in a biofluid sample are separated by SEC. Free proteins elute from the column in later fractions than EVs because free proteins are smaller than the pore size of the beads while EVs are larger and are excluded from entering the beads
c. Aliquots of 0.45 µm filtered plasma or CSF are isolated using SEC, ultracentrifugation, or ExoQuick precipitation. Samples from each isolation method are then loaded into a 96-well plate into a Quanterix HD-X instrument for Simoa analysis of CD9, CD63, CD81, and albumin.

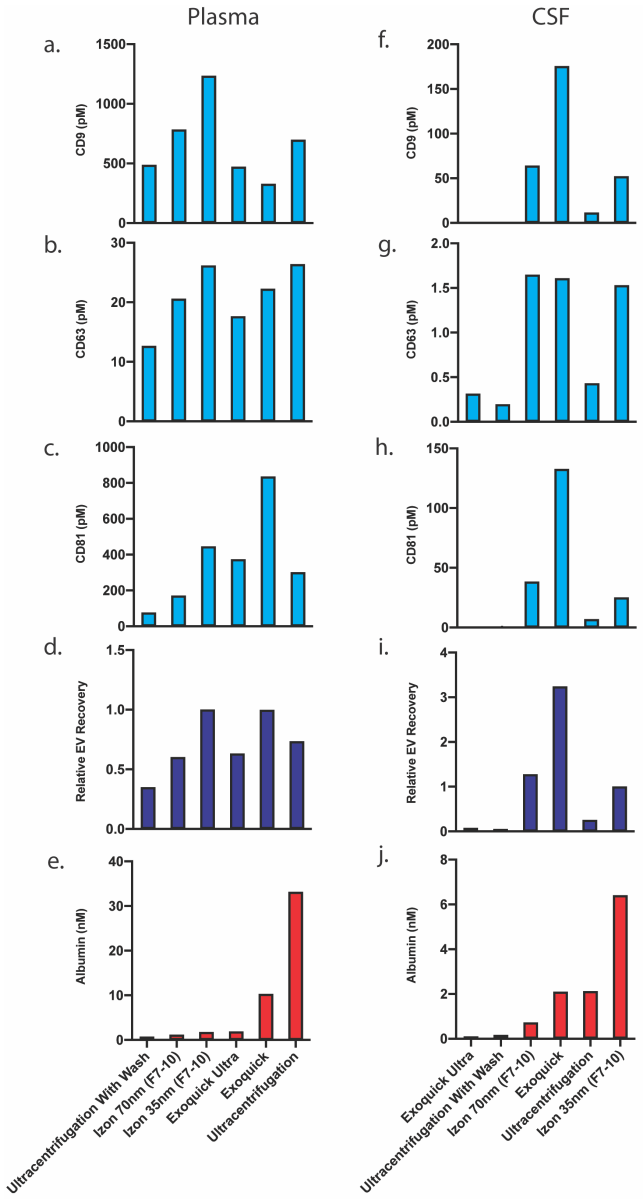

Figure 2. 2 Comparison of existing methods for EV isolation in plasma and CSF

All methods are listed in order of increasing albumin levels.
a-c. Individual tetraspanin yields using different isolation methods from plasma.
d. Relative EV recovery from plasma was calculated by first normalizing individual tetraspanin values (in pM) in each technique to that of Izon qEVoriginal 35nm EV fractions (7-10) and then averaging the three tetraspanin percentages.
e. Albumin levels using different EV isolation methods from plasma.
f-h. Individual tetraspanin yield using different isolation methods from CSF.
i. Relative EV recovery in CSF was calculated by first normalizing individual tetraspanin values (in pM) in each technique to that of Izon qEVoriginal 35nm fractions (7-10) and then averaging the three tetraspanin percentages.
j. Albumin levels using different EV isolation methods from CSF.

averaged the relative tetraspanin recovery values across the three tetraspanins to calculate relative EV recovery (Figure 2.2).

After determining combined relative EV recovery and albumin concentration for each EV isolation method, we could directly compare EV recovery and purity in both plasma and CSF. In plasma, we found that the Izon qEVoriginal 35nm SEC column (collecting fractions 7-10) yielded both the highest recovery of EVs and the highest purity of EVs (Figure 2.2a-e). Meanwhile, in CSF, ExoQuick yielded the highest recovery of EVs while Izon qEVoriginal 70nm yielded the highest purity (Figure 2.2f-j).

2.3.3 Application of Simoa for custom SEC column optimization

We next took advantage of Simoa's high throughput to optimize EV isolation from 0.5 mL samples of plasma and CSF using SEC. We prepared our own SEC columns and systematically tested several parameters of the SEC isolation procedure in an effort to improve EV yield and purity beyond that of the commercially available columns. To accomplish this goal, we tested three Sepharose resins (CL-2B, CL-4B and CL-6B) at two column heights (10 and 20 mL). This comprehensive comparison led us to several conclusions. First, we found that resins with smaller pore sizes led to higher yield. Sepharose CL-6B, which has the smallest pore size, gave the highest yield of EVs, although it was accompanied by higher albumin contamination, as expected. For all SEC columns, higher purity could also be achieved by taking a smaller number of fractions (e.g. 7-9 instead of 7-10), albeit at the expense of lower EV yield. We quantified this difference for all columns and found that doubling the height of any given column from 10 to 20 mL resulted in better separation between EVs and free proteins, leading to

higher purity but lower EV recovery (Figures 2.3 & 2.4). When we compared different volumes of plasma and CSF for a 10 mL Sepharose CL-6B column, we found that the sample volume loaded had an effect on purity, with larger loading volumes leading to lower purity (Figure 2.5).

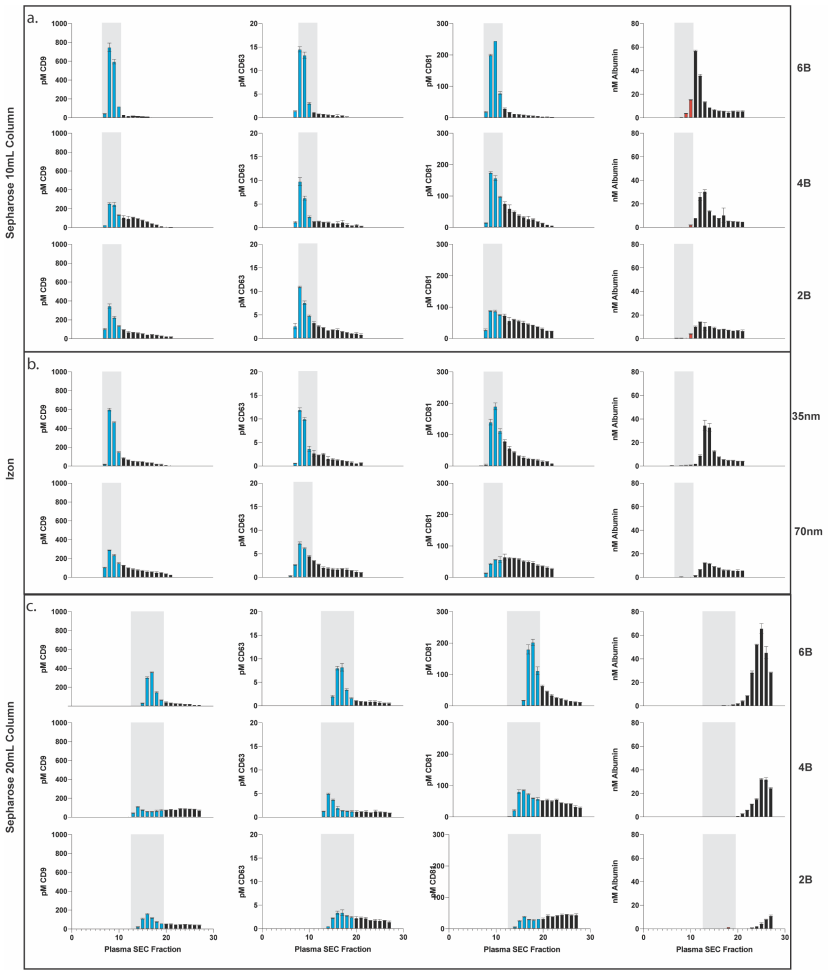

Figure 2. 3 Comparison of SEC methods for EV isolation in plasma

Error bars represent the standard deviations from two technical replicates.
a. Levels of tetraspanins and albumin in plasma after fractionation with 10 mL custom columns filled with: Sepharose CL-6B (top), Sepharose CL-4B (middle), and Sepharose CL-2B (bottom).
b. Levels of tetraspanins and albumin in plasma after fractionation with Izon qEVoriginal 35nm column (top) and Izon qEVoriginal 70nm column (bottom).
c. Levels of tetraspanins and albumin in plasma after fractionation with 20mL custom columns; Sepharose CL-6B (top), Sepharose CL-4B (middle), Sepharose CL-2B (bottom).

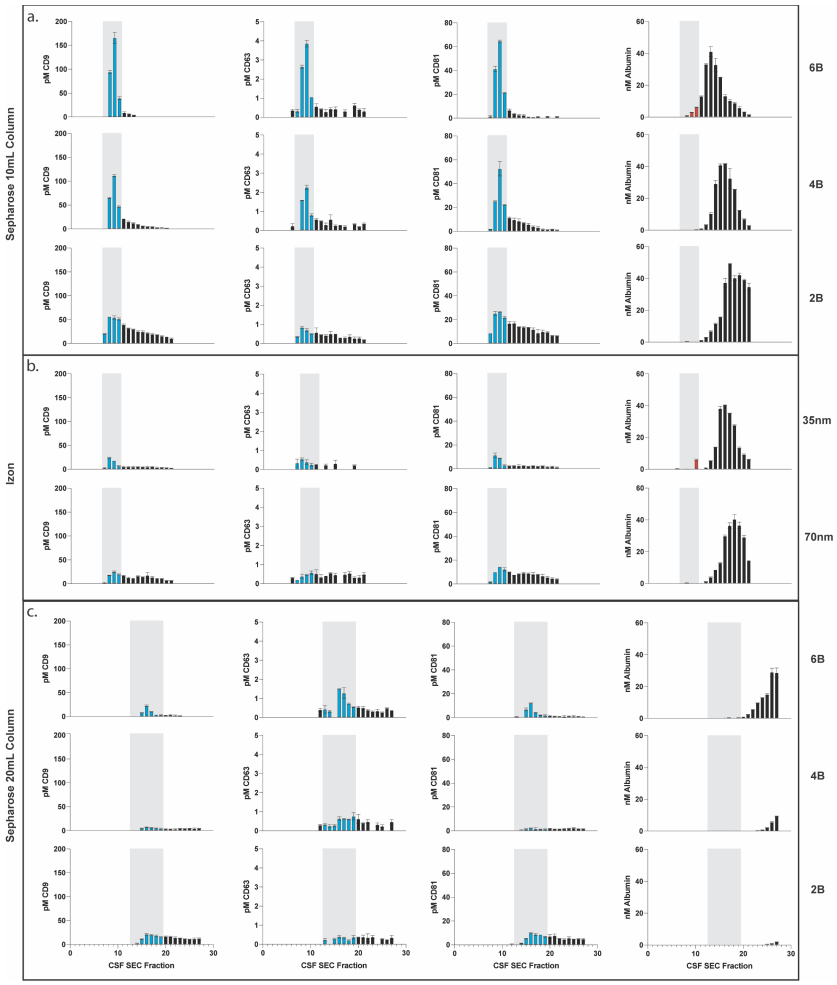

Figure 2. 4 Comparison of SEC methods for EV isolation in CSF

Error bars represent the standard deviations from two technical replicates.
a. Levels of tetraspanins and albumin in CSF after fractionation with 10 mL custom columns filled with: Sepharose CL-6B (top), Sepharose CL-4B (middle), and Sepharose CL-2B (bottom).
b. Levels of tetraspanins and albumin in CSF after fractionation with Izon qEVoriginal 35nm column (top) and Izon qEVoriginal 70nm column (bottom).
c. Levels of tetraspanins and albumin in CSF after fractionation with 20mL custom columns; Sepharose CL-6B (top), Sepharose CL-4B (middle), Sepharose CL-2B (bottom).

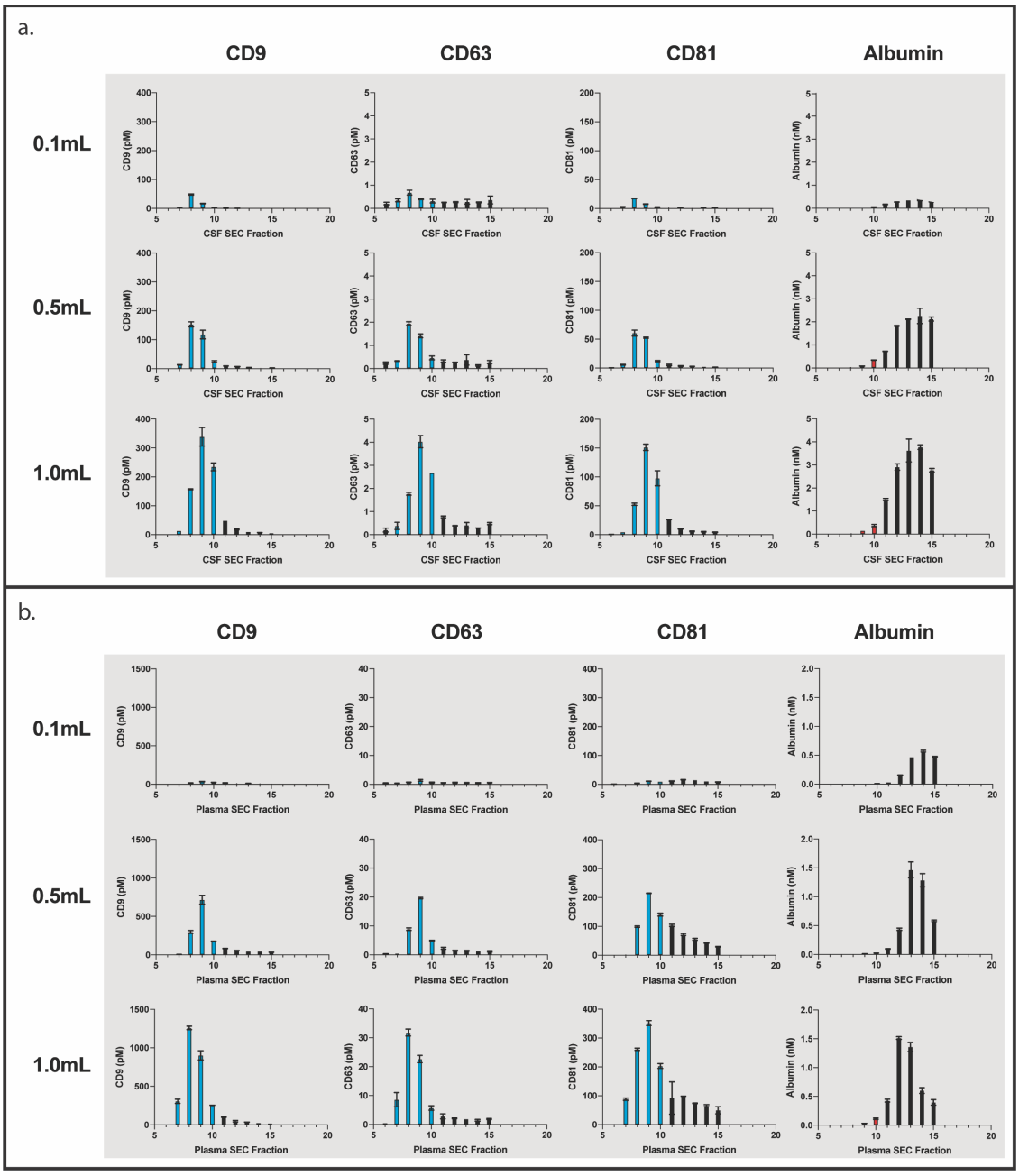

Figure 2. 5 Effect of CSF and plasma sample volume on SEC

a. Effect of sample volume on EV recovery and purity by SEC for 0.1 mL (top), 0.5 mL (middle) and 1.0 mL (bottom) samples of CSF. Simoa was performed to determine levels of CD9, CD63, CD81 and albumin after fractionating different volumes of CSF by SEC using a 10 mL Sepharose CL-6B column.
b. Effect of sample volume on EV recovery and purity by SEC for 0.1 mL (top), 0.5 mL (middle) and 1.0 mL (bottom) samples of plasma. Simoa was performed to determine levels of CD9, CD63, CD81 and albumin after fractionating different volumes of plasma by SEC using a 10 mL Sepharose CL-6B column.

2.3.4 Direct comparison of all EV isolation methods

Combining all of the Simoa data we generated, we were able to perform a direct, quantitative comparison of the relative yield and purity of EVs across all methods tested. We normalized the level of each tetraspanin recovered using a given method by the level measured across all fractions (6-21) in a 10 mL Sepharose CL-6B column. We then averaged the values of the three tetraspanins to obtain relative EV recovery for each method. Similarly, albumin contamination was calculated by normalizing the amount of albumin in each isolation method to the total albumin detected in all fractions of a 10 mL Sepharose CL-6B column (Figure 2.6).

For plasma, the techniques that demonstrated the highest recovery were Sepharose CL-6B 10 mL, Izon qEVoriginal 35nm column, and ExoQuick (Figure 2.6a). Of these three methods, Sepharose CL-6B 10 mL demonstrated the highest yield whereas the Izon qEVoriginal 35nm column demonstrated the highest purity. For CSF, we observed the highest recovery with 10 mL Sepharose CL-6B, Sepharose CL-4B, and ExoQuick (Figure2.6b). Sepharose CL-6B 10 mL demonstrated the highest yield, while Sepharose CL-4B demonstrated the highest purity of these three methods. These findings suggest that the best isolation method depends both on the biofluid of interest and downstream application since there is a tradeoff between EV yield and purity.

2.4 Discussion

We developed Simoa assays that can be used for ultrasensitive quantification of EVs in biological fluids and applied these assays to the analysis of EV isolation methods.

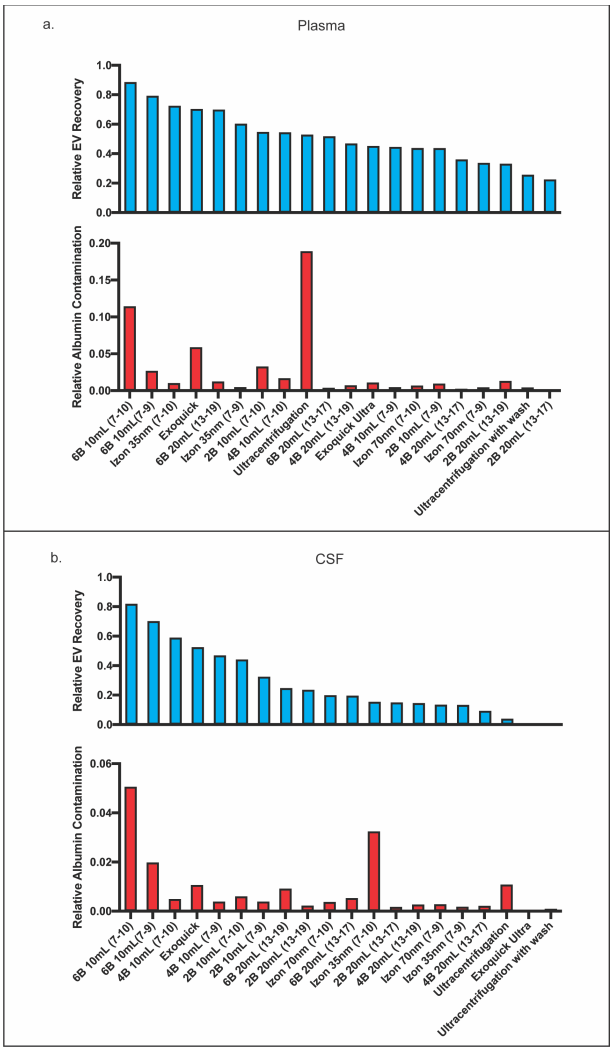

Figure 2. 6 Comparison of EV recovery and albumin contamination across all tested methods in plasma and CSF

a. Comparison of plasma EV recovery (top) and albumin contamination (bottom) across all tested methods ranked by EV recovery. Relative EV recovery was calculated by individually normalizing each tetraspanin to the sum of that tetraspanin in all fractions (6-21) in the 10mL Sepharose CL-6B condition. The three tetraspanin percentages were then averaged to calculate the relative EV recovery. Similarly, albumin for each condition was calculated as a fraction of the albumin found in all fractions (6-21) in the 10mL Sepharose CL-6B condition.
b. Comparison of CSF EV recovery (top) and albumin contamination (bottom) across all tested methods ranked by EV recovery. Relative EV recovery was calculated by individually normalizing each tetraspanin to the sum of that tetraspanin in all fractions (6-21) in the 10mL Sepharose CL-6B condition. The three tetraspanin percentages were then averaged to calculate the relative EV recovery. Similarly, albumin for each condition was calculated as a fraction of the albumin found in all fractions (6-21) in the 10mL Sepharose CL-6B condition.

Although several techniques have previously been applied to EV detection [15], Simoa technology has a unique set of features that makes it particularly well-suited for measuring EVs, overcoming several limitations of other methods. Simoa effectively differentiates EVs from other particles such as lipoproteins or aggregated proteins, since transmembrane proteins are present on EVs but should not be present in other particles. Simoa also offers high dynamic range, throughput, and sensitivity. This sensitivity is achieved by converting ELISA to a digital readout via immuno-capture and counting of individual protein molecules in a microwell array. The high-throughput nature of Simoa is enabled by the automated liquid handling of the commercially-available Quanterix HD-X instrument, although our lab has developed other digital ELISA methods that do not rely on commercial instrumentation [91-93] which could be similarly applied to EVs.

We used Simoa to directly compare yield and purity of EV isolation methods. To obtain the purest EVs possible (and separate EVs from lipoproteins), it has been shown that it is necessary to combine several techniques sequentially, such as density gradient centrifugation (DGC) and SEC [94,95]. However, techniques such as DGC are not scalable to many samples and therefore not amenable to biomarker studies. Thus, we focused on several commonly-used EV isolation methods that are amenable to biomarker studies and used Simoa to assess their recovery and purity in both plasma and CSF.

Although several previous reports have previously compared EV isolation methods [96-106] and yielded important insights, the lack of available quantitative methods for EV measurement has made these studies difficult to interpret [81,83,107]. We introduce Simoa as a new analytical tool to rapidly provide a quantitative comparison of EV isolation methods. Although not every EV will necessarily contain a tetraspanin protein,

by detecting three different tetraspanins per sample with Simoa, we minimize the probability that we are measuring a rare subset of EVs. In the experiments reported here, we observed a strong correlation of the relative levels of the three tetraspanins in different SEC fractions. Since we compared isolation methods from the same starting sample, we were able to provide a direct quantitative comparison of tetraspanin levels between the different isolation methods. By also developing a Simoa assay to measure free albumin (the main contaminant of EV preparations), we were able to assess the purity of EV preparations with respect to unwanted co-purification of free proteins.

We compared ultracentrifugation (with and without a wash), the commonly used commercial EV precipitation reagent ExoQuick (as well as the newer version, ExoQuick Ultra), and SEC using two different commercial Izon qEV columns. Our results show that there are significant differences between the performance of various methods between plasma and CSF. These differences could be due to a much higher protein concentration in plasma than CSF, which may affect the yield and purity of the different isolation methods. Of the existing methods, commercial SEC columns gave the best combination of yield and purity in plasma. In CSF, EV precipitation by ExoQuick gave higher yield but lower purity than SEC.

Given the high-throughput capabilities of Simoa, we compared several resins and column volumes to improve EV isolation by SEC. Analyzing the tetraspanin and albumin levels in each fraction, we directly compared homemade columns using two different bed volumes and three different resins to the most commonly-used commercial SEC columns. Our results demonstrate that the custom columns significantly improve EV yield over that of the commercial columns. In particular, we find that Sepharose CL-6B, which has not

been previously used for EV isolation, yields considerably higher levels of EVs than Sepharose CL-2B or Sepharose CL-4B. This is likely due to Sepharose CL-6B beads having a smaller average pore size, leading to a lower probability that EVs will enter the beads.

In SEC, we find that there is a tradeoff between EV yield and albumin contamination. Collecting more EVs generally means more albumin contamination, as the later EV fractions become contaminated with free protein. Thus, we envision different SEC columns will be suited for different applications. Using a 10 mL Sepharose CL-6B column for EV isolation from plasma or CSF is the best choice for downstream applications where maximum EV yield is needed and where some free protein contamination is not detrimental. Use of this column would also be preferable for analyzing rare EV cargo or when further purification of EVs will be performed (such as immuno-isolation). On the other hand, if isolating EVs from plasma where minimal free protein contamination is desired (for example, in EV protein analysis by western blot), a larger 20 mL column with Sepharose CL-6B or Sepharose CL-4B would yield better results. For CSF, we found that larger 20 mL columns demonstrated poor yield; therefore, using 10 mL columns is preferable - Sepharose CL-6B for maximum yield or Sepharose CL-4B for maximum purity.

We used Simoa to quantify EVs after using the different isolation methods, but we think Simoa should be useful for a much broader set of EV-related applications. We analyzed EV subpopulations with capture and detection antibodies against one transmembrane protein at a time, but individual EVs can also be probed with antibodies against more than one protein [108]. Our assays used detergents, since once isolated we did

not need to keep EVs intact. Although it has been previously reported that EVs remain intact in the presence of low concentrations of Tween [109], we did not confirm the integrity of EVs in our studies. Future studies should ensure that assay conditions preserve intact EVs, which would allow Simoa to be applied to study EV heterogeneity at the level of individual vesicles.

The general experimental framework presented here could be easily applied to evaluate new EV isolation methods in plasma, CSF, or other biological fluids, such as urine or saliva. One could also add Simoa assays for lipoproteins and other common contaminants to evaluate how well various methods separate EVs from other particles present in biological fluids. These methods could also be applied to the study of EVs produced by cultured cells. The sensitivity and high-throughput nature of Simoa should allow for relative EV quantification in cell culture media from small numbers of cells, thus allowing analysis of the effects of genetic or cellular perturbations. As sensitivity of EV detection and specificity in differentiating EVs from contaminants are obstacles in all EV studies, we envision that ultrasensitive protein detection of EV surface proteins will be applicable to both the study of basic EV biology and the development of diagnostic methods.

2.5 Author Contributions

DT and MN conceived of study and designed experiments. DT, MN, WT, JHL, and RL performed experiments. DT, MN, and DRW analyzed data and wrote the manuscript with input from all authors. GMC and DRW supervised the study and provided funding support.

2.6 Acknowledgements

Funding for this study was provided by the Chan Zuckerberg Initiative (CZI) Neurodegeneration Challenge Network (NDCN) and Good Ventures Foundation. Schematics were created with BioRender.com

2.7 Competing Interests

DRW is the scientific founder and a board member of Quanterix Inc. GMC commercial interests: http://arep.med.harvard.edu/gmc/tech.html The authors have filed a provisional patent on some of the work described in this manuscript.

Chapter 3: L1CAM is not Associated with Extracellular Vesicles in Human Cerebrospinal Fluid or Plasma[2]

[2] Norman M, Ter-Ovanesyan D, Trieu W, Lazarovits R, Kowal EJK, Lee JH, Chen-Plotkin AS, Regev A, Church GM, Walt DR. 2021. *Nat Methods*.18(6):631-634. Reprinted here with permission of publisher.

3.1 Introduction

Developing therapeutics for neurological and psychiatric conditions has lagged far behind other medical disciplines partly due to the inability to perform brain biopsies on living individuals. Our current understanding of brain diseases relies mainly upon postmortem tissue analysis after neurodegeneration and cell death have already occurred. Therefore, fundamental questions about the underlying biochemical processes of neurological and psychiatric disease still remain. Having access to the proteomic and transcriptomic profiles of neurons and other brain cells in living patients would be a great asset to our understanding of neuroscience. Furthermore, the ability to measure biochemical changes in response to medication would be a novel and useful tool for drug development.

One potential approach to learning about the living brain is to analyze extracellular vesicles (EVs). EVs, which are released from many cell-types and found in all biofluids, contain proteins and RNAs from their cell of origin [110]. There has been a great deal of excitement about capturing EVs released from neurons and characterizing their contents as a window into neurological processes. Over the past several years, a large number of studies have reported the immunocapture of putatively neuron-derived EVs (NDEVs) and subsequent measurement of proteins and RNA implicated in neurodegenerative and psychiatric diseases. Almost all of these studies [9,28-71] used as a handle for EV capture the transmembrane protein L1CAM, a cell adhesion molecule implicated in neural development [111]. The choice of L1CAM relied on its known expression in neurons, presence in plasma, and the availability of high-affinity antibodies.

However, there are reasons that L1CAM may not be a good marker for NDEVs. First, L1CAM is expressed widely outside of the brain, including on non-neuronal cells [112]. Furthermore, L1CAM has been shown to exist in soluble forms. It is therefore not safe to assume that L1CAM present in extracellular fluids is necessarily vesicle-associated, but this must be directly validated. Currently, publications that report measuring proteins inside L1CAM EVs use antibodies to the L1CAM ectodomain [9,28-71]. However, if L1CAM is cleaved or alternatively spliced in the CSF and plasma, then it is possible that soluble L1CAM is being captured, rather than EVs. Here we develop both a framework and the necessary tools for evaluating whether a given protein is a good candidate for NDEV pulldown.

3.2 Methods

3.2.1 Electron Microscopy

Plasma fractions 9 and 12 from SEC using a 10mL Sepharose CL-6B column were fixed in 2% paraformaldehyde and then stained with 2% uranyl formate. Samples were added to 400 mesh formvar/carbon film copper grids (Electron Microscopy Sciences) and liquid was wicked away using Whatman filter paper. Samples were imaged using a JEM-1400 120 kV transmission electron microscope (JEOL USA). Images were taken using AMT image capture engine V602 (Advanced Microscopy Techniques).

3.2.2 Human Sample Handling

Pre-aliquoted human plasma and CSF samples were ordered from BioIVT. For spike and recovery and dilution linearity experiments, individual CSF and plasma from

BioIVT were utilized. For all other experiments, pooled CSF and plasma were used. Plasma or CSF was thawed at room temperature. Immediately after the sample had thawed, 100X Protease/Phosphatase Inhibitor Cocktail (Cell Signaling Technology) was added at 1X final concentration to the sample. The sample was then centrifuged at 2000 x *g* for 10 minutes. Next, the supernatant was centrifuged through a 0.45µm Corning Costar SPIN-X centrifuge tube filter (Sigma-Aldrich) at 2000 x *g* for 10 minutes to get rid of any remaining cells or cell debris.

3.2.3 Simoa Assays

Candidate capture antibodies were coupled to carboxylated paramagnetic beads from the Simoa Homebrew Assay Development Kit (Quanterix) using EDC chemistry (Thermo Fisher Scientific). Candidate detection antibodies were conjugated to biotin using EZ-Link NHS-PEG4 Biotin (Thermo Fisher Scientific). Reagents were cross-tested for signal against the following recombinant proteins for CD9, CD63, CD81, L1CAM and albumin: ab152262 (Abcam), TP301733 (Origene), CD81 Origene TP317508 (Origene), TP311601 (Origene), ab201876 (Abcam) on a Simoa HD-X Analyzer (Quanterix). The antibody pairs that gave the highest signal to background ratio were further validated in two ways: First, plasma and CSF were serially diluted in sample buffer in order to demonstrate endogenous dilution linearity (Figure 3.4). Next, the recombinant protein used in the calibration curve was added to plasma and CSF at two different concentrations in order to determine that spike and recovery was within 70-130% (Table 3.1).

For CD9, CD63, CD81 and L1CAM assays, samples were incubated with immunocapture beads (25 μL) and biotinylated detection antibody (20 μL) for 35 minutes. Next, six washes were performed, and the beads were resuspended in 100 μL of Streptavidin labeled β-Galactosidase (Quanterix) and incubated for 5 minutes. An additional six washes were performed, and the beads were resuspended in 25 μL Resorufin β-D-Galactopyranoside (Quanterix) before being loaded into the microwell array.

For the albumin assay, samples were incubated first with immunocapture beads (25 μL) for 15 minutes and then washed six times. Subsequently, 100 μL detection antibody was incubated with the beads for 5 minutes. Next, six washes were performed, and the beads were resuspended in 100 μL of Streptavidin labeled β-Galactosidase (Quanterix) for a final 5-minute incubation. An additional six washes were performed, and the beads were resuspended in 25 μL Resorufin β-D-Galactopyranoside (Quanterix) before being loaded into the microwell array.

3.2.4 Plate-Based ELISA

Simoa assays were transferred to a plate-based ELISA for comparison. Capture antibody was diluted in ELISA Coating Buffer (BioLegend) at a concentration of 4 μg/mL and 100 μL was coated per well on a Nunc MaxiSorp ELISA plate (BioLegend). Plates were incubated with capture antibody overnight at 4 °C. Subsequently, the plate was washed 3 times with 200 μL PBST. Sample was added to each well and incubated at room temperature for 3 hours. The plate was again washed 3 times with 200 μL PBST. 100 μL of corresponding detection antibody was added to the plate and left to incubate

for 1 hour. Detection antibody was then removed, and the plate was washed 3 times with 200 μL PBST. 100 μL Streptavidin labeled β-Galactosidase from the Simoa Homebrew Assay Development Kit (Quanterix) was then added and incubated for 30 minutes. The plate was then washed 5 times with 200 μL PBST and incubated with 100 μL of Resorufin β-D-Galactopyranoside, also from the Simoa Homebrew Assay Development Kit (Quanterix), for 20 minutes in the dark. Plates were then imaged with a Tecan Plate Reader using Magellan v 7.2 software at 555 nm excitation and 605 nm emission.

3.2.5 Western Blotting

Western blotting was performed as previously described in detail [113].

3.2.6 Western blot for Figure 3.5:

Equal volumes of each SEC fraction were loaded on a Bolt 4-12% Bis-Tris Plus gel (Thermo Fisher Scientific) after addition of Bolt LDS sample buffer (Thermo Fisher Scientific) and denaturation at 70°C for 10 minutes. The gel was run at 150 V for 60 minutes and then transferred onto a nitrocellulose membrane using the iBlot2 Dry Blotting System (Thermo Fisher Scientific). The following primary antibodies were used for western blot at the corresponding dilutions in milk overnight at 4°C: MM2/57 for CD9 (Millipore Sigma) at 1:1000, h5c6 for CD63 (BD Biosciences) at 1:1000, M38 for CD81 (Thermo Fisher Scientific) at 1:666. After three washes with PBST, anti-mouse IgG Secondary antibody (Bethyl Laboratories) was added for 2 hours in milk buffer at 1:2000. After three more washes in PBST, SpectraQuant HRP-CL Spray Chemiluminescent Detection Reagent (BridgePath Scientific) was used to develop the

western blots. Imaging was performed on the Sapphire Biomolecular Imager (Azure Biosystems).

3.2.7 Immunocapture & Western blot for Figure 3.6:

Immunocapture of L1CAM from plasma and CSF was performed using the Dynabeads antibody coupling kit (Invitrogen 14311D). Following the manufacturer's instructions either anti-L1CAM antibody (Abcam ab272321) or anti-MCherry control antibody (Abcam ab232341). Four aliquots of 1mL of CSF or .375mL of plasma were incubated at 4°C overnight with gentle rotation. Plasma or CSF were washed 4 times with PBS and resuspended in LDS with reducing buffer. Immunocaptured plasma and CSF L1CAM as well as human brain lysate and iNGN cell lysate were loaded on a Bolt 4-12% Bis-Tris Plus gel (Thermo Fisher Scientific) after addition of Bolt LDS sample buffer with reducing buffer (Thermo Fisher Scientific) and denaturation at 70°C for 10 minutes. The gel was run at 150V for 120 minutes and then transferred onto a nitrocellulose membrane using the iBlot2 Dry Blotting System (Thermo Fisher Scientific). The following primary antibodies were used for western blot at the corresponding dilutions in milk overnight at 4°C: UJ127 (Abcam) at 1:2000 and 2c2 (Abcam) at 1:500. After three washes with PBST, anti-mouse cross IgG secondary antibody (Bethyl Laboratories) was added for 2 hours in milk buffer at 1:2000. After three more washes in PBST, SpectraQuant HRP-CL Spray Chemiluminescent Detection Reagent (BridgePath Scientific) was used to develop the western blots. Imaging was performed on the Sapphire Biomolecular Imager (Azure Biosystems).

3.2.8 Preparation of Custom SEC Columns

Sepharose CL-6B (GE Healthcare) was washed in PBS. Briefly, the volume of resin was washed with an equal volume of PBS in a glass jar and then placed at 4 °C in order to let the resin settle completely (several hours or overnight). The PBS was then poured off, and new PBS was again added for a total of 3 washes. Columns were prepared fresh on the day of use. Washed resin was poured into an Econo-Pac Chromatography column (Bio-Rad) for a 10 mL bed volume. The column was allowed to drip out until the column was solid at which time the top frit was placed securely at the top of the resin but without compression. PBS was then added at 1 mL above the frit until sample was ready to be added.

3.2.9 Collection of Size Exclusion Chromatography Fractions

Once prepared, all columns were washed with at least 20 mL of PBS in the column. When sample was ready to be loaded, the column was allowed to fully drip out and, after last drop, plasma or CSF was added to the column. Immediately thereafter, 0.5 mL fractions were collected. As soon as the plasma or CSF completely went through the frit, PBS was added to top of column 1 mL at a time. For plasma and CSF, fractions 6-19 were collected while for iNGN fractions 6-15 were collected. For the comparison of Simoa, ELISA, and western blot, one 0.5 mL sample was fractionated by SEC using an Izon qEVoriginal 35nm column into 0.5 mL fractions (fractions 6-15). Each of the fractions was then divided evenly for use in the three techniques.

3.2.10 Proteinase Protection Assay

SEC was performed on 1mL plasma and fractions 7-10 were pooled. 200uL of this solution was used for each of four conditions:

a) No treatment, two-hour incubation, lyse with 1% Triton X, one-hour incubation
b) 100ug Proteinase K application (Thermo Fisher), two-hour incubation, lyse with 1% Triton X, one-hour incubation
c) No treatment, one-hour delay, add PMSF to a final concentration of 2.5mM for one hour, lyse with 1% Triton X, one-hour incubation
d) 100ug Proteinase K application (Thermo Fisher), one-hour incubation, add PMSF to a final concentration of 2.5mM for one hour, lyse with 1% Triton X, one-hour incubation

After the final incubation, each sample was diluted in Homebrew Sample Diluent (Quanterix) to a final volume of 800uL and measured using Simoa assays to Alix and Albumin on the Quanterix HD-X instrument.

3.2.11 Density Gradient

For the density gradient centrifugation, an Optiprep (Iodixanol) gradient was prepared using the following layers (from top to bottom): 2 mL 5%, 3mL 10%, 3mL 20%, 3 mL 40% layers. Each layer of Optiprep (Millipore Sigma) was diluted in solution of 0.25M Sucrose (Millipore Sigma) and Tris-EDTA pH 7.4 (Millipore Sigma) . Sample (1mL) was loaded on top of the 5% fraction. Samples were centrifuged at 100,000 RCF for 18 hours at 4C in 13.2 Polypropylene tubes (Beckman Coulter). Fractions were

removed from the top in 1 mL increments. To calculate the density of each fraction, 1 mL of PBS was loaded on a gradient instead of sample. The refractive index of each fraction was measured with a refractometer after ultracentrifugation and then density was calculated based on this measurement.

3.2.12 Mass Spectrometry

Excised gel bands around the size of 180-240kDa were cut from a polyacrylamide gel and submitted for mass spectrometry analysis. Gel pieces were washed and dehydrated with acetonitrile, and then acetonitrile was removed. Gel pieces were dried in Speed-Vac and a modified in-gel Trypsin procedure was performed [114]. Samples were then reconstituted in 5 - 10 µl of HPLC solvent A (2.5% acetonitrile, 0.1% formic acid). A nano-scale reverse-phase HPLC capillary column was created by packing 2.6 µm C18 spherical silica beads into a fused silica capillary with a flame-drawn tip [115]. Each sample was loaded via a Famos auto sampler (LC Packings) onto the column. Peptides were eluted with increasing concentrations of solvent B (97.5% acetonitrile, 0.1% formic acid), subjected to electrospray ionization, and entered into an LTQ Orbitrap Velos Pro ion-trap mass spectrometer (Thermo Fisher Scientific). Peptide sequences were determined by matching protein databases with the acquired fragmentation pattern by the software program, Sequest (Thermo Fisher Scientific) [116].

3.2.13 iNGN EV isolation

Previously described iNGN cells were grown in mTeSR1 media (STEMCELL Technologies) on Matrigel (Corning) coated plates. Doxycycline (Sigma Aldrich) was

diluted in PBS and added to MTeSR1 at a final concentration of 0.5 μg/mL to initiate differentiation. On Day 4 after Dox addition, media was switched to Gibco DMEM with GlutaMAX (Thermo Fisher Scientific) supplemented with B27 Serum-Free Supplement (Thermo Fisher Scientific) and Gibco Penicillin Streptomycin (Thermo Fisher Scientific). On Day 6, EVs were isolated by differential ultracentrifugation, as previously described [117], and resuspended in PBS.

3.2.14 Splicing RNA-Seq Analysis

For analysis of Genotype-Tissue Expression database (GTEx) data, pre-processed exon-exon junction read- counts were obtained from the publicly available version 8 database (https://GTExportal.org). The read table was filtered to include only junctions falling within the body of L1CAM and these counts were analyzed using custom python scripts available upon request. Reads aligning to L1CAM (chrX:153,859,517-153,888,173) were visually examined using the Integrative Genomics Viewer (IGV) [118] to assess evidence of inclusion or exclusion of exon 25.

3.3 Results

In light of research demonstrating that both cleaved and alternatively spliced forms of L1CAM exist, we first sought to evaluate whether L1CAM in plasma and CSF is EV-associated, or free. To do so, we fractionated biofluids using size exclusion chromatography (SEC) and density gradient centrifugation (DGC) to separate EVs from free proteins. We hypothesized that if L1CAM were predominantly associated with EVs, it would elute along with EV markers like the tetraspanins CD9, CD63 and CD81 [110].

Alternatively, if L1CAM was predominantly a free protein, it would elute along with free proteins like albumin (schematically represented in Figure 3.1a). We first demonstrated that EVs isolated from the conditioned media of human iPS-derived neurons show L1CAM in earlier fractions of SEC but recombinant L1CAM protein elutes in later fractions (Figure 3.1b). Although there is some overlap at the tails, these distributions are clearly distinct, and thus we refer to these samples as molecular standards for which fractions constitute vesicle-associated vs. free protein throughout the rest of this study.

Next, we investigated EVs in human CSF and plasma. To demonstrate that the early SEC fractions (7-10) of these biofluids contain intact EVs, we performed proteinase protection assays (for Alix, reported to be internal to EVs) on these fractions, and identified EVs by Electron Microscopy (Figures 3.2 & 3.3). Since EVs are present at low concentrations, we next developed and optimized high sensitivity assays for EV markers (CD9, CD63 and CD81) as well as for L1CAM and albumin (Figures 3.4,3.5 & Table 3.1). We utilized Simoa technology [18] to measure these proteins in fractionated CSF and plasma.

To ascertain whether this improved sensitivity was necessary for quantifying EVs in biological samples, human plasma and CSF samples were fractionated using a commercially available SEC column (Izon qEVoriginal 35nm), and fractions were evenly split for downstream analysis using Simoa, ELISA, and western blotting. Simoa quantified tetraspanins in EV fractions 7-10 (early fractions where EVs are expected) for all markers in both plasma and CSF (b,d,f). ELISA was able to quantify CD9 in expected EV fractions (7-10) for plasma, while only a subset of the expected EV fractions were quantifiable in plasma for CD63 and CD81. In contrast, none of the CSF fractions

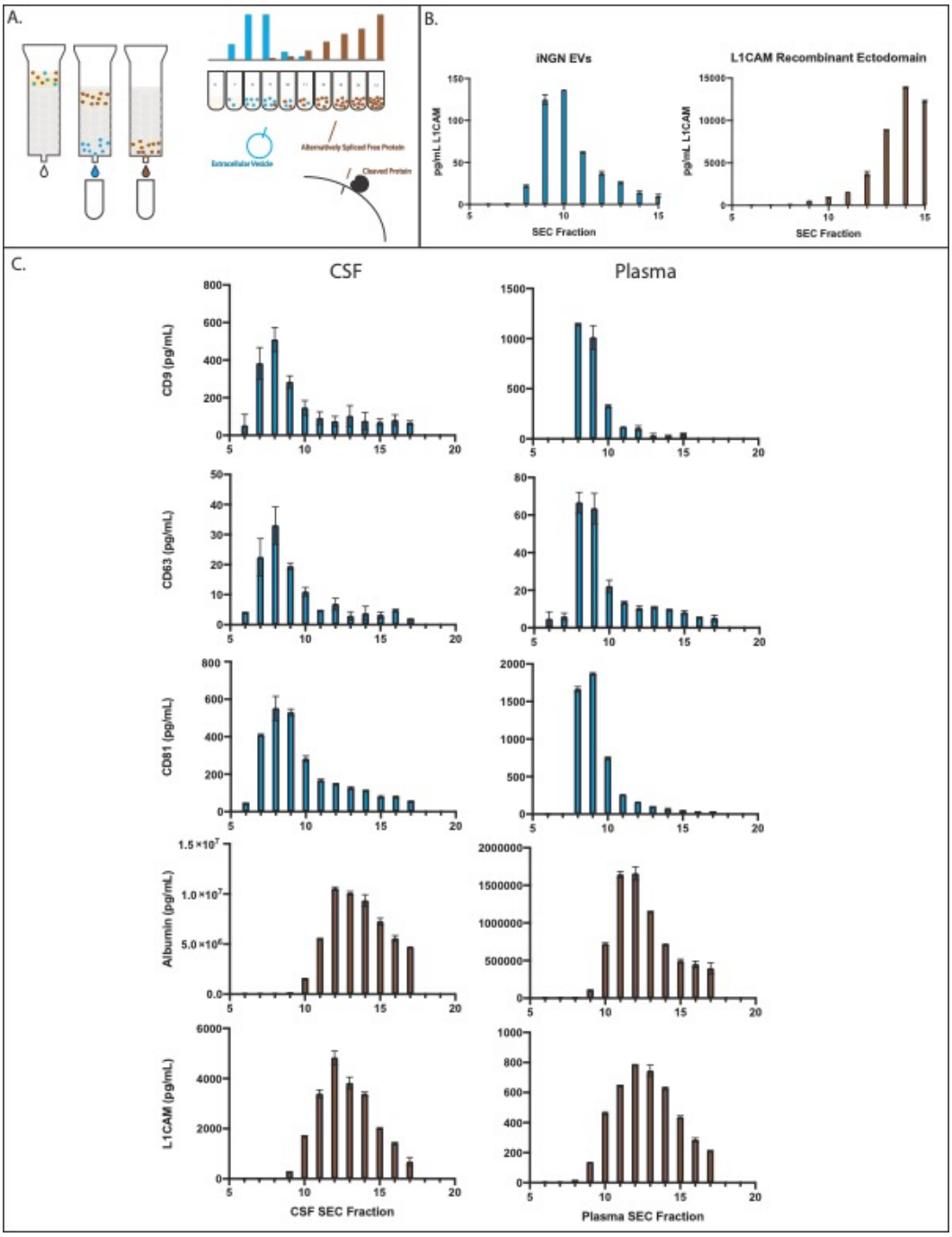

Figure 3. 1 Method for evaluating whether L1CAM is EV-associated or free in biofluids

a. Schematic representation of our method for evaluating whether L1CAM is EV-associated using Size Exclusion Chromatography
b. Size Exclusion Chromatography of cell culture EVs expressing L1CAM (left) and a free recombinant L1CAM protein (right)
c. Simoa quantification of CD9, CD63, CD81, albumin and L1CAM in Sepharose 6B 10mL SEC fractions of CSF (left) and Plasma (right)

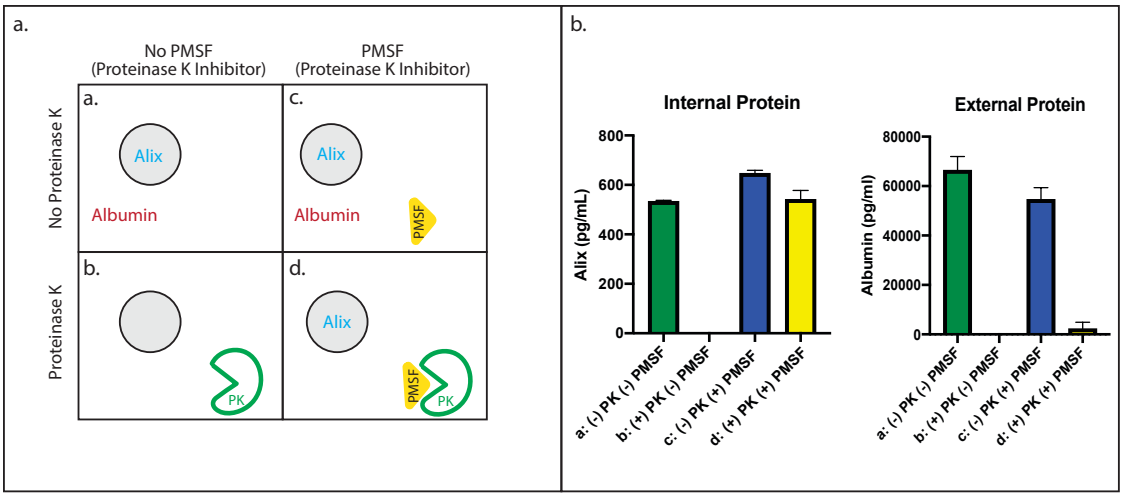

Figure 3. 2 Proteinase Protection Assays

EVs have a lipid bilayer that protects the contents within. If an EV is intact and proteinases are introduced to the sample, the internal proteins will be preserved. In order to demonstrate that plasma SEC fractions 7-10 contain intact EVs, we treated these fractions with Proteinase K. By subsequently inactivating the Proteinase K with PMSF before lysing the EVs, we confirm that internal EV proteins are protected, while external proteins are fully degraded. To demonstrate EVs were intact, we split the preparations into four conditions:

a. No treatment, two-hour incubation, lyse with Triton X, one-hour incubation
b. Proteinase K application, two-hour incubation, lyse with Triton X, one-hour incubation
c. No treatment, one-hour delay, add PMSF for one hour, lyse with Triton X, one-hour incubation
d. Proteinase K application, one-hour incubation, add PMSF to inhibit Proteinase K for one hour, lyse with Triton X, one-hour incubation

After these steps, we used homebrew Simoa assays to measure Alix (a protein known to be internal to EVs) and Albumin (a protein known to be secreted and therefore external to EVs). We observe that the level of Alix is identical using conditions a, c and d but disappears completely in b in which lysis occurs without Proteinase K inactivation. Alternatively, we see that Albumin is high using conditions a and c but close to zero using conditions b and d in which Proteinase K is present. These results suggest that SEC fractions 7-10 contain intact EVs; otherwise, Alix would not be protected from the Proteinase K treatment and would behave like Albumin. Error bars represent technical replicates of the Simoa assay measurements.

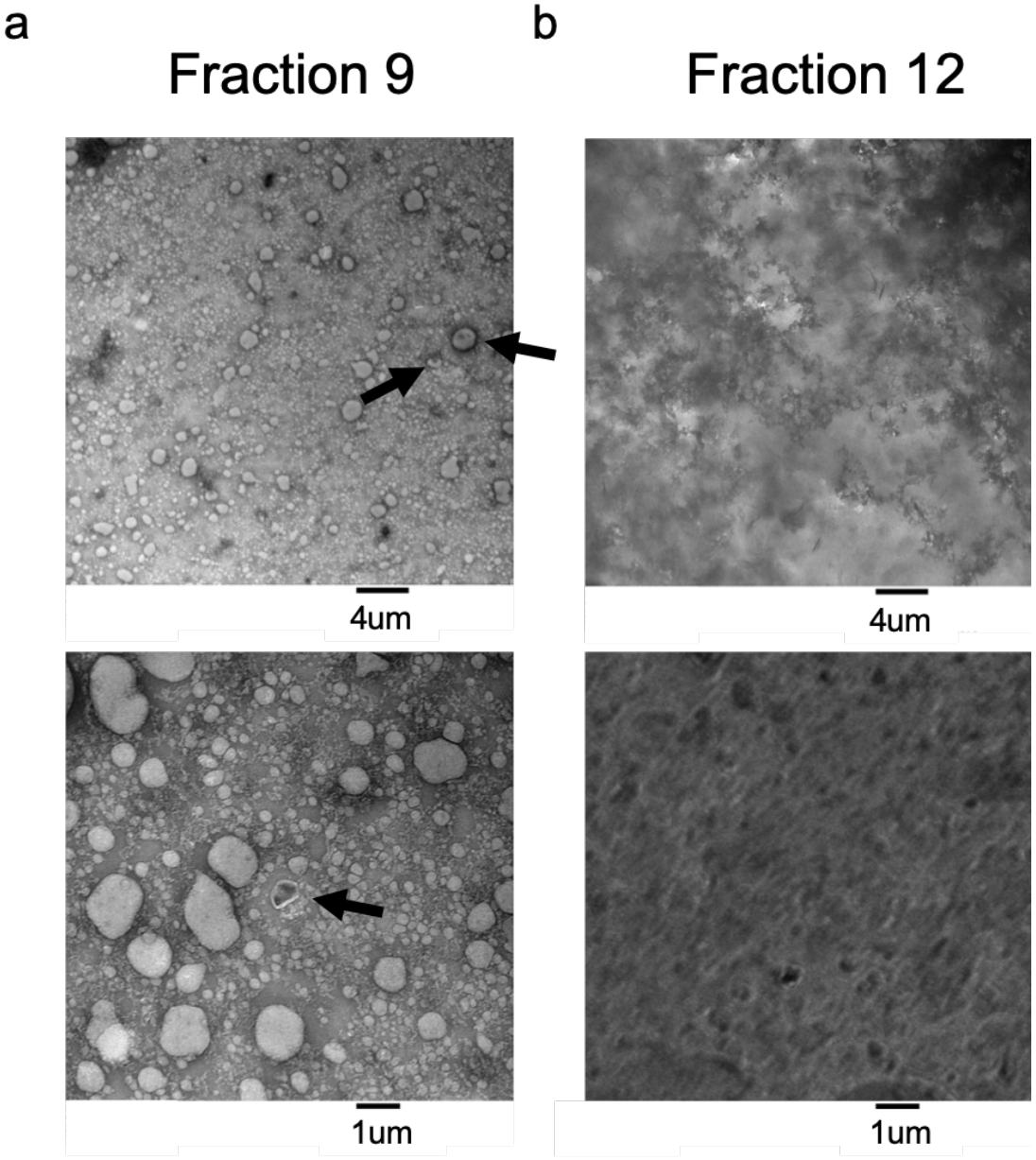

Figure 3. 3 Electron Microscopy of SEC fractions

Transmission Electron Microscopy of a. Fraction 9 and b. Fraction 12 from 1mL plasma fractionated using SEC with a Sepharose CL-6B column and negatively stained with uranyl formate. Representative images are shown at 6000x magnification (top) and 20,000x magnification (bottom). Arrows indicate “cup-shaped” EVs.

a.

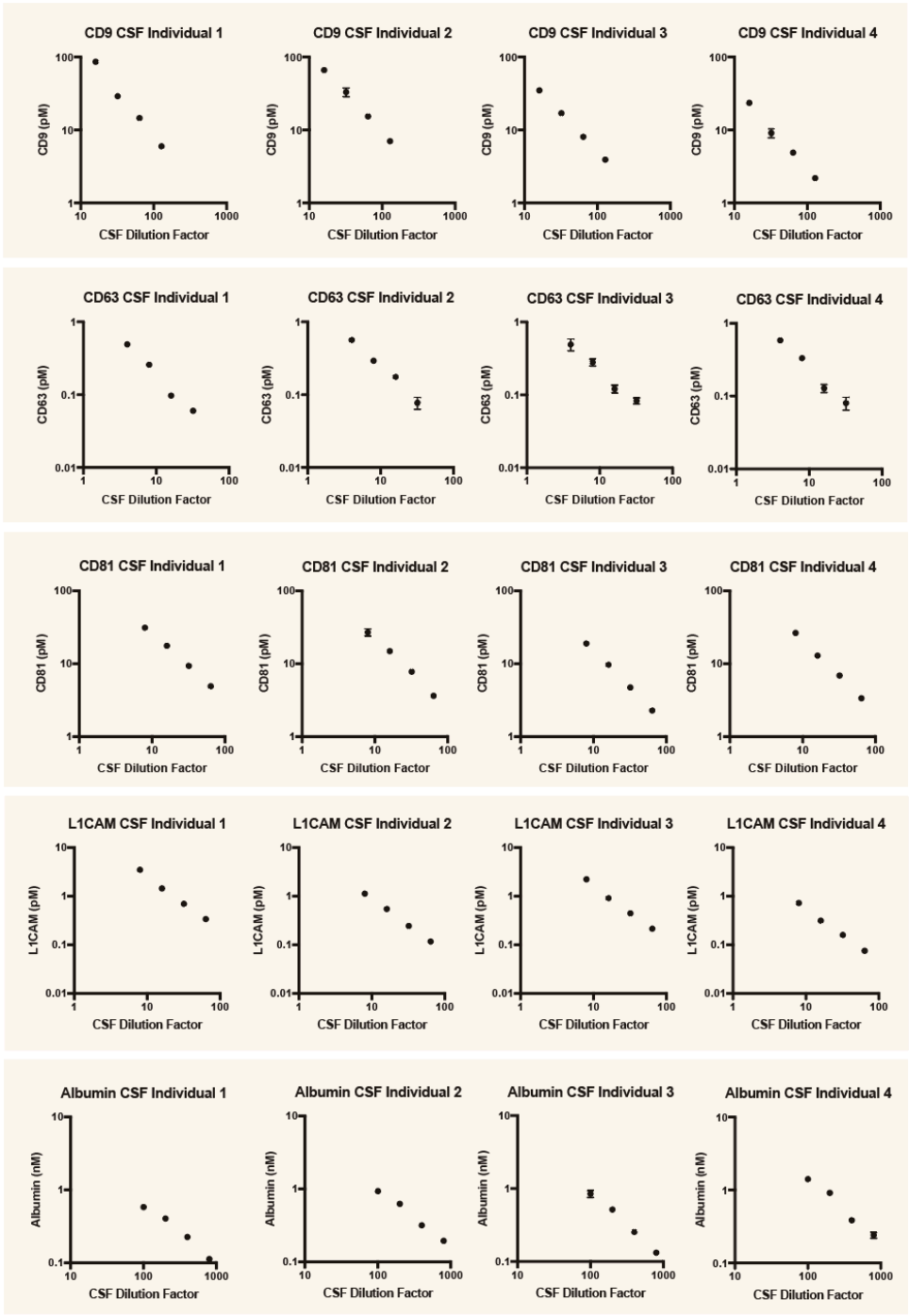
CD9 CSF Individual 1
CD9 CSF Individual 2
CD9 CSF Individual 3
CD9 CSF Individual 4
CD9 (pM)
CD63 CSF Individual 1
CD63 CSF Individual 2
CD63 CSF Individual 3
CD63 CSF Individual 4
CD63 (pM)
CD81 CSF Individual 1
CD81 CSF Individual 2
CD81 CSF Individual 3
CD81 CSF Individual 4
CD81 (pM)
L1CAM CSF Individual 1
L1CAM CSF Individual 2
L1CAM CSF Individual 3
L1CAM CSF Individual 4
L1CAM (pM)
Albumin CSF Individual 1
Albumin CSF Individual 2
Albumin CSF Individual 3
Albumin CSF Individual 4
Albumin (nM)
CSF Dilution Factor

b.

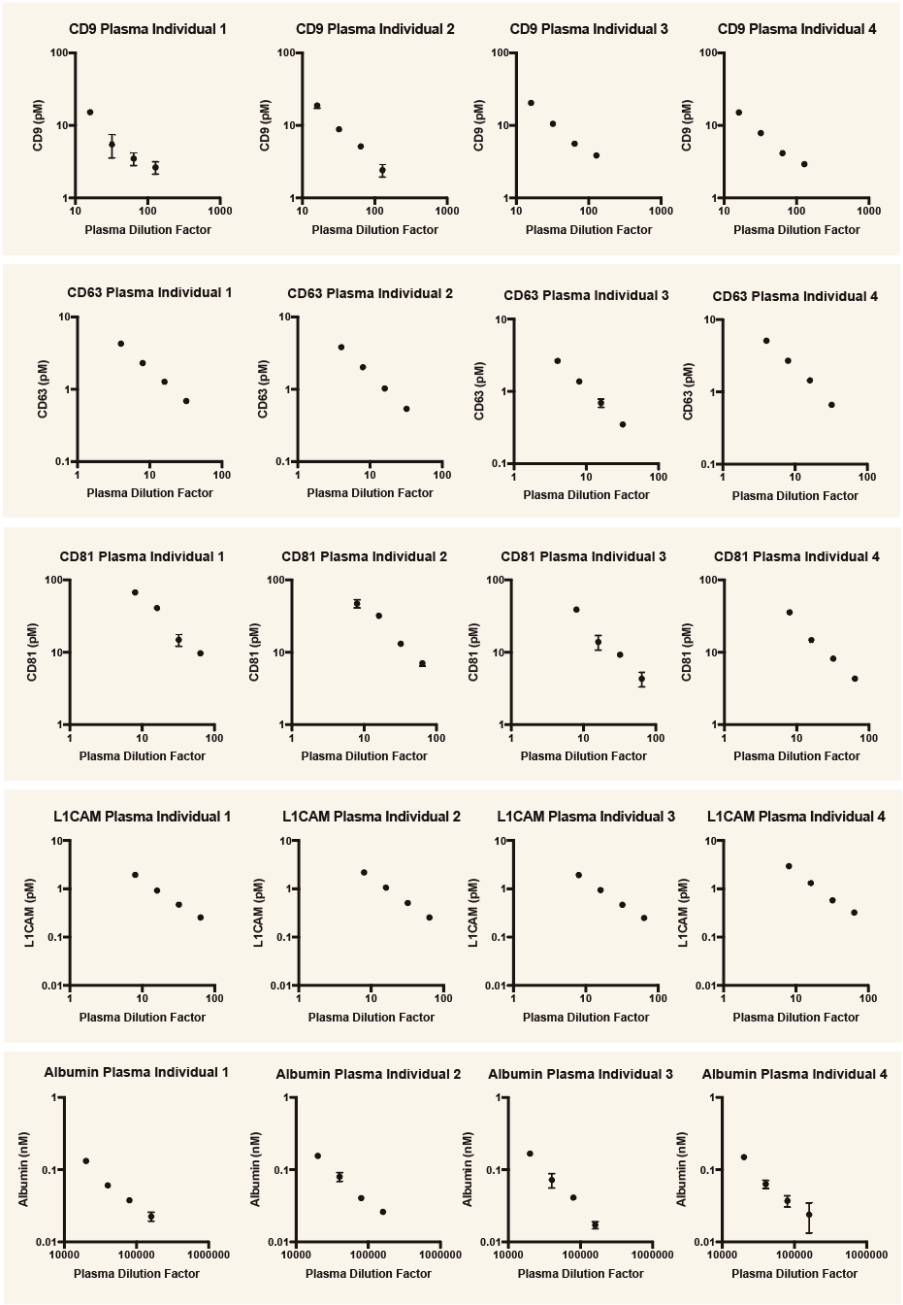

Figure 3. 4 Linearity of dilution for Simoa assays

We developed Simoa assays for the EV markers CD9, CD63, CD81 as well as for L1CAM and albumin. To ensure that our assays are accurate and precise, we performed validation experiments. Each assay demonstrated endogenous dilution linearity (parallelism) in human CSF (a) and plasma (b). Error bars represent the standard deviation from two technical replicates. Each linearity experiment was performed on the CSF and plasma from four individuals.

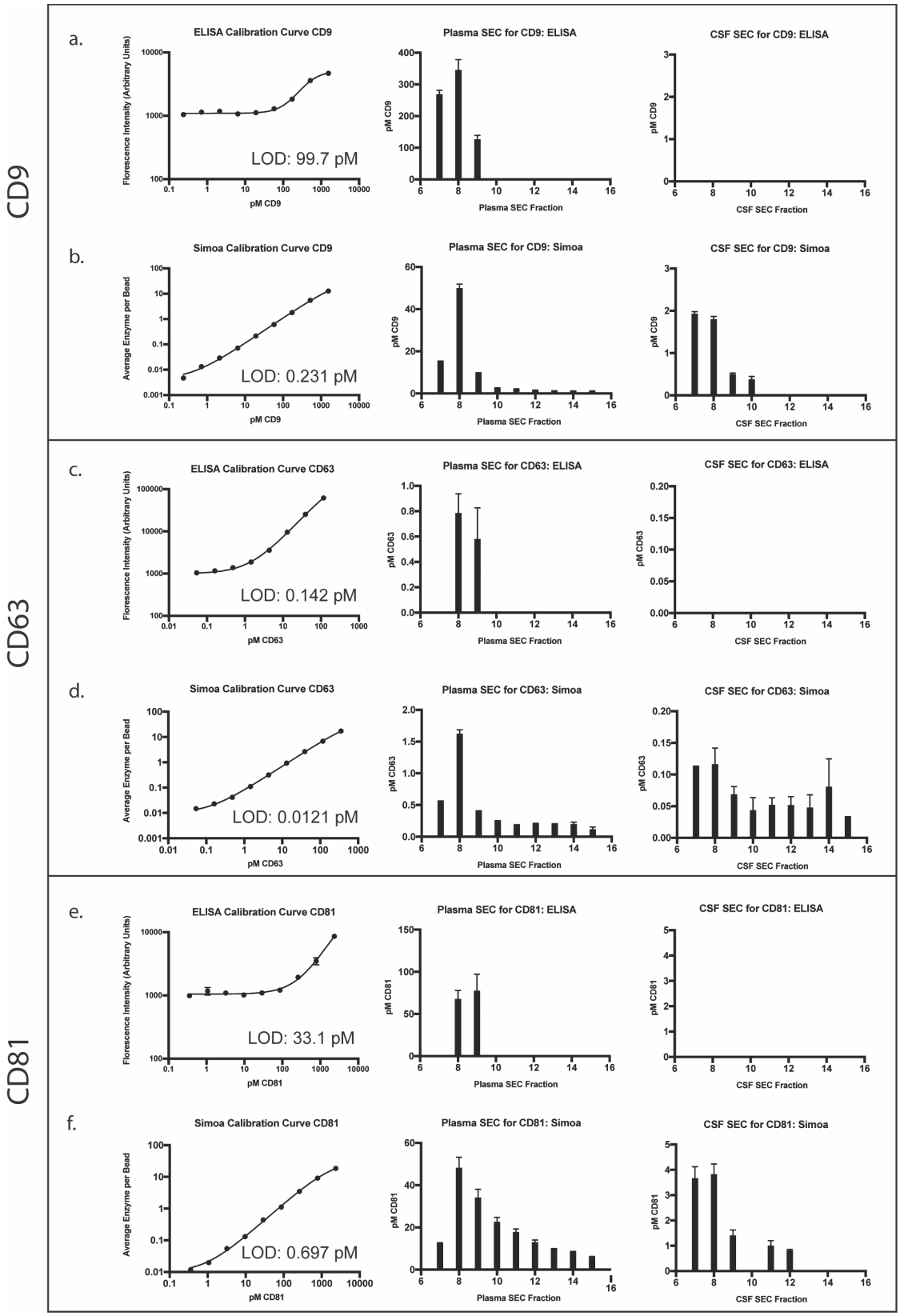
CD9
CD63
CD81
a.
ELISA Calibration Curve CD9
Florescence Intensity (Arbitrary Units)
pM CD9
LOD: 99.7 pM
Plasma SEC for CD9: ELISA
pM CD9
Plasma SEC Fraction
CSF SEC for CD9: ELISA
pM CD9
CSF SEC Fraction
b.
Simoa Calibration Curve CD9
Average Enzyme per Bead
pM CD9
LOD: 0.231 pM
Plasma SEC for CD9: Simoa
pM CD9
Plasma SEC Fraction
CSF SEC for CD9: Simoa
pM CD9
CSF SEC Fraction
c.
ELISA Calibration Curve CD63
Florescence Intensity (Arbitrary Units)
pM CD63
LOD: 0.142 pM
Plasma SEC for CD63: ELISA
pM CD63
Plasma SEC Fraction
CSF SEC for CD63: ELISA
pM CD63
CSF SEC Fraction
d.
Simoa Calibration Curve CD63
Average Enzyme per Bead
pM CD63
LOD: 0.0121 pM
Plasma SEC for CD63: Simoa
pM CD63
Plasma SEC Fraction
CSF SEC for CD63: Simoa
pM CD63
CSF SEC Fraction
e.
ELISA Calibration Curve CD81
Florescence Intensity (Arbitrary Units)
pM CD81
LOD: 33.1 pM
Plasma SEC for CD81: ELISA
pM CD81
Plasma SEC Fraction
CSF SEC for CD81: ELISA
pM CD81
CSF SEC Fraction
f.
Simoa Calibration Curve CD81
Average Enzyme per Bead
pM CD81
LOD: 0.697 pM
Plasma SEC for CD81: Simoa
pM CD81
Plasma SEC Fraction
CSF SEC for CD81: Simoa
pM CD81
CSF SEC Fraction

g.

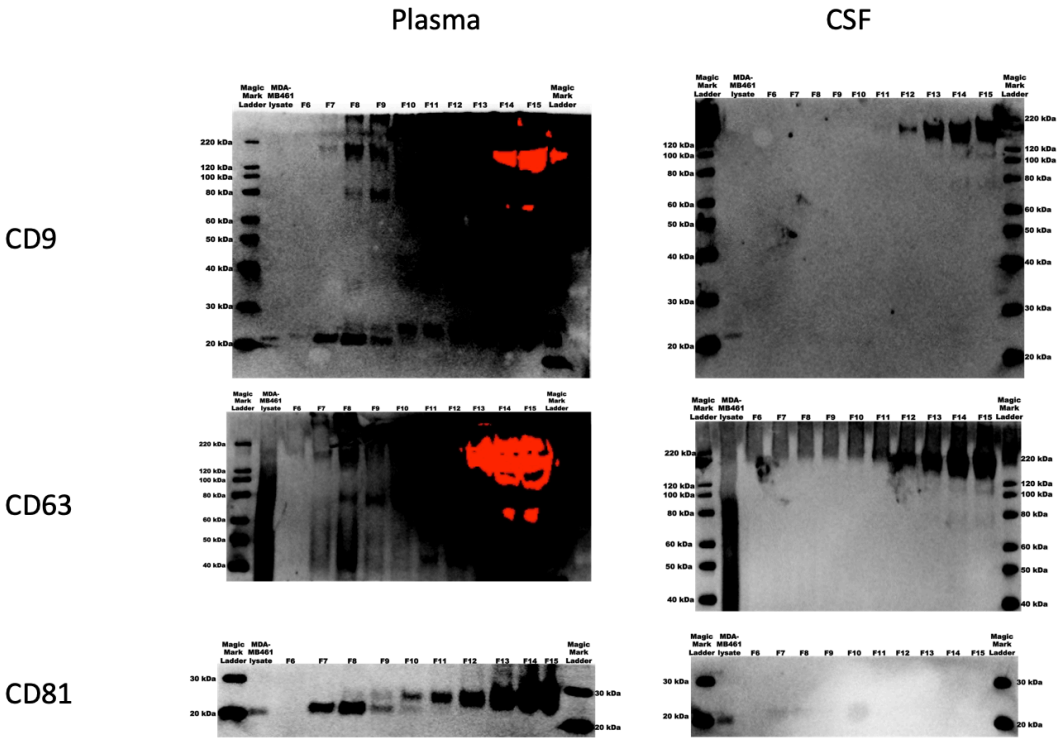

Figure 3. 5 Comparison of ELISA and Simoa for EV quantification

ELISA and Simoa were used to measure tetraspanin levels. For each assay, the same sample is directly compared by ELISA and Simoa for the calibration curve using protein standard (left), EV quantification of pooled plasma SEC fractions (middle) and EV quantification of pooled CSF SEC fractions (right) (a-f). The limits of detection (LOD) of the five Simoa assays were one to two orders of magnitude more sensitive than their respective standard ELISAs using the same set of antibodies for each target. Error bars represent the standard deviation from two technical replicates.

7-10 were quantifiable by ELISA for any of the tetraspanins (a,c,e). When the SEC fractions were analyzed by western blot using the same volume of each fraction, we observed very high background in the plasma fractions (due to the high abundance of free proteins), but the tetraspanins were detectable and matched the general pattern of the Simoa results. We did not detect any tetraspanins in the CSF fractions (g). Simoa was the

Protein	CSF Dilution Factor/Spike	Average Recovery (4 Individuals)	Plasma Dilution Factor/Spike	Average Recovery (4 Individuals)
CD9	32x+500	86%	32x+500	79%
	32x+1000	101%	32x+1000	74%
CD63	16x+10	106%	16x+10	83%
	16x+50	105%	16x+50	74%
CD81	32x+500	104%	32x+500	106%
	32x+1000	101%	32x+1000	94%
Albumin	400x+50000	90%	80000x+50000	85%
	400x+100000	85%	80000x+100000	90%
L1CAM	32x+500	106%	64x+500	102%
	32x+1000	107%	64x+1000	98%

Table 3. 1 Spike and recovery for Simoa assays

We spiked the recombinant protein used for the calibration curve into human plasma and CSF and quantified the percent recovery. Each assay recovered between 70-130% of the spiked concentration, indicating good assay precision. Data averaged across four individuals and two technical replicates.

only assay method that allowed quantification of EVs in SEC fractions for both plasma and CSF.

To evaluate whether L1CAM elutes in fractions with EVs or with free protein, we utilized two complementary techniques, SEC and DGC [96]. When CSF and plasma were fractionated by SEC, the tetraspanins were detected primarily in fractions 7-9, while L1CAM was detected with a similar distribution to albumin in fractions 11-14 (Figure 3.1c). When CSF and plasma were fractionated by DGC, we observed the same pattern, with the tetraspanins eluting in different fractions than the L1CAM and albumin signals: in CSF, the tetraspanins eluted in fractions 5-10, while albumin and L1CAM eluted in Fractions 1-5 (Figure 3.6a). In plasma, the tetraspanins eluted in fractions 7-11 while L1CAM, like albumin, eluted in fractions 1-6 (Figure 3.6a). Thus, with either of these two fractionation methods, L1CAM in human biofluids behaves as a free protein, not an EV-associated protein.

Next, we set out to investigate the isoforms of L1CAM detected in CSF and plasma. We hypothesized two ways in which the L1CAM ectodomain may be present as a free protein: L1CAM present on cells may be cleaved by proteases such as ADAM10 or Plasmin [119,120], or an isoform of L1CAM lacking a transmembrane domain may be produced by alternative splicing [112]. We expect that proteolytic cleavage of L1CAM would produce a molecule containing the extracellular domain, but not its intracellular domain (schematically represented in Figure 3.6b), while alternative splicing excluding specifically the transmembrane domain would produce a molecule containing both the extracellular and intracellular domains as part of a soluble protein.

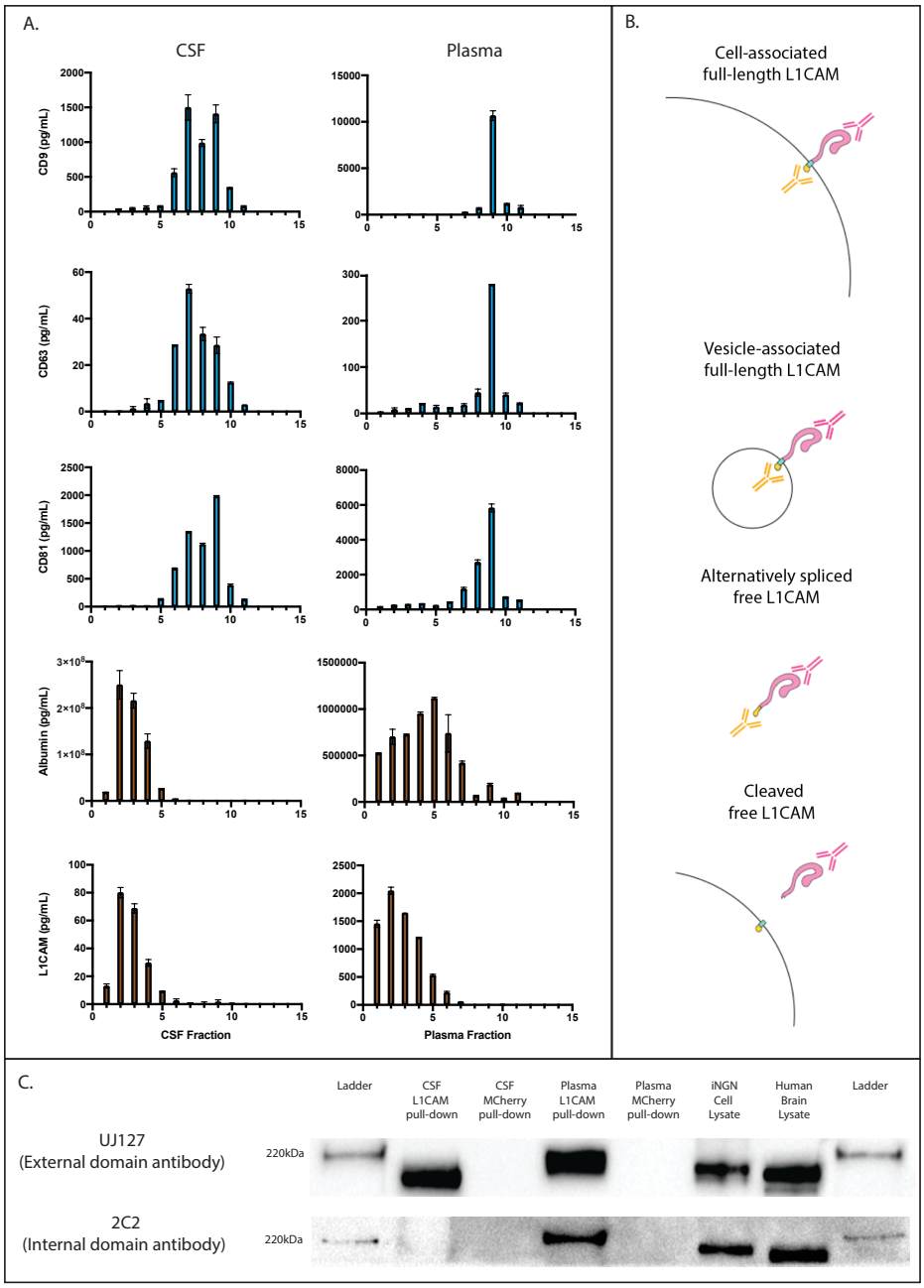

Figure 3. 6 Density Gradient Centrifugation of CSF and Plasma & Analysis of L1CAM Isoforms

a. Simoa quantification of CD9, CD63, CD81, albumin and L1CAM in Density Gradient Centrifugation fractions of CSF (left) and plasma (right). The density of fractions 1-11 were as follows in g/mL: 1.012, 1.028, 1.045, 1.056, 1.065, 1.076, 1.097, 1.113, 1.138, 1.193, 1.219.
b. Schematic representation of putative L1CAM isoforms present in the human body
c. Western blotting of L1CAM immunocaptured in CSF and plasma using an antibody to the external domain of L1CAM (Clone EPR23241-224). Staining was done with one antibody to an external domain (Clone UJ127) or internal domain (Clone 2C2).

We immunocaptured L1CAM and performed Western blotting utilizing one antibody to the external domain and another to the internal domain. L1CAM immunocaptured from CSF produced a band at approximately 200 kDa, which blotted only with the external domain antibody, but not with the internal domain antibody. Conversely, L1CAM immunocaptured from plasma demonstrated a band at approximately 220 kDa and blotted with both the internal and external domain antibodies, (Figure 3.6c). Additionally, using mass spectrometry, we were able to detect a peptide matching the cytoplasmic portion of L1CAM in plasma (Figure 3.7). Although we are not able to conclude whether soluble L1CAM is cleaved, alternatively spliced or both, our mass spectrometry and Western blot results suggest that some proportion of soluble L1CAM in plasma is alternatively spliced to exclude the exon encoding for the transmembrane domain [112,119,120]

The transmembrane domain of L1CAM is contained entirely in exon 25 (Figure 3.8). Skipping of this exon leads to production of an L1CAM protein containing an ER signal sequence but no domain for insertion into the plasma membrane; thus the protein is likely secreted into the extracellular medium. Expressed sequence tags (ESTs) have previously been observed showing skipping of exon 25 in human endothelial cell lines [112]. We analyzed Genotype-Tissue Expression (GTEx) RNA-Seq data across diverse human organs to investigate L1CAM splicing status in other tissues. Although the junction reads supporting inclusion of exon 25 generally outnumbered those supporting skipping, we did observe reads traversing the junction from exon 24 directly to exon 26 in a number of tissues, including Tibial artery (Figure 3.8). These reads in Tibial artery

and other organs support the existence of an L1CAM isoform lacking its transmembrane domain (Figure 3.9).

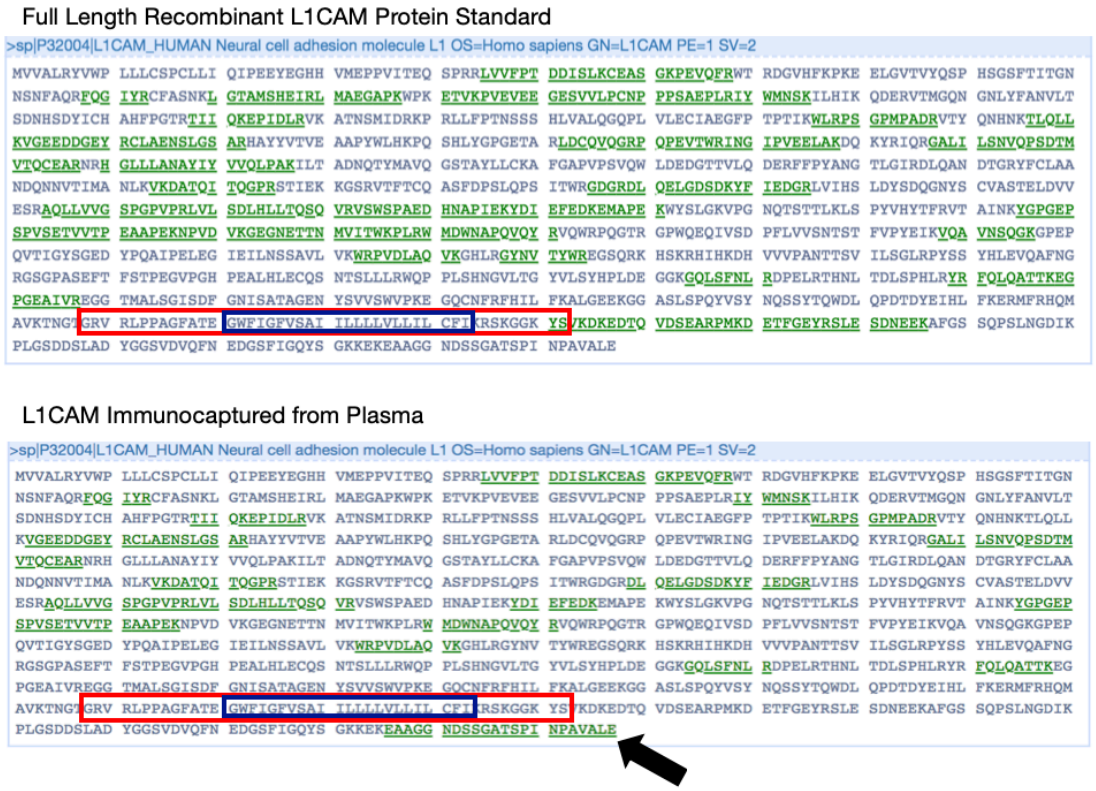

Figure 3. 7 Mass spectrometry of L1CAM immunocaptured from plasma

Mass spectrometry of full length recombinant L1CAM protein standard shows, as expected, peptides matching an isoform which includes Exon 25 (a). Mass Spectrometry of L1CAM immunocaptured from human plasma shows peptides matching the cytosolic domain at the C terminus (emphasized with black arrow) (b). Full length sequence of L1CAM displayed with peptides from mass spectrometry shown in green. Blue box indicates L1CAM transmembrane domain and red box indicates amino acid sequence encoded by Exon 25.

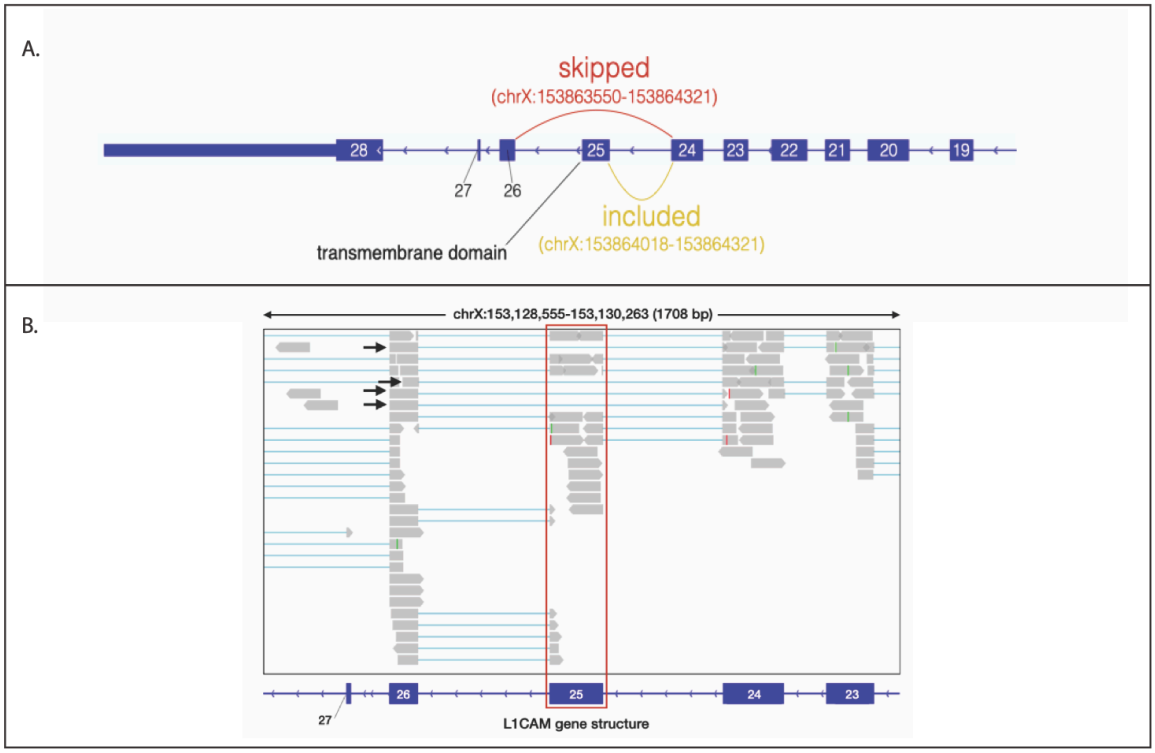

Figure 3. 8 Analysis of RNA-seq data for L1CAM

a. In GTEx samples, RNA-seq supports some skipping of exon 25, as junction reads between exons 24 and 26 are detected.
b. Reads from GTEx RNA-Seq data of human Tibial Artery loaded in Integrative Genome Browser (IGV) aligning to Exon 25 of L1CAM, which contains the transmembrane domain (highlighted in red). Junction reads supporting the skipping of Exon 25 are indicated with black arrows.

Finally, we sought to understand why prior publications had found increased "cargo" proteins such as alpha-synuclein in their L1CAM EV samples. We hypothesized that this may be caused by nonspecific binding of free alpha-synuclein in plasma to the L1CAM antibody. To test this hypothesis, we followed the L1CAM immunocapture protocol of one such study utilizing the same L1CAM antibody and nonspecific mIgG control antibodies, but we performed the isolation on recombinant alpha-synuclein instead of plasma [28]. Utilizing a Simoa assay we found that three times more recombinant

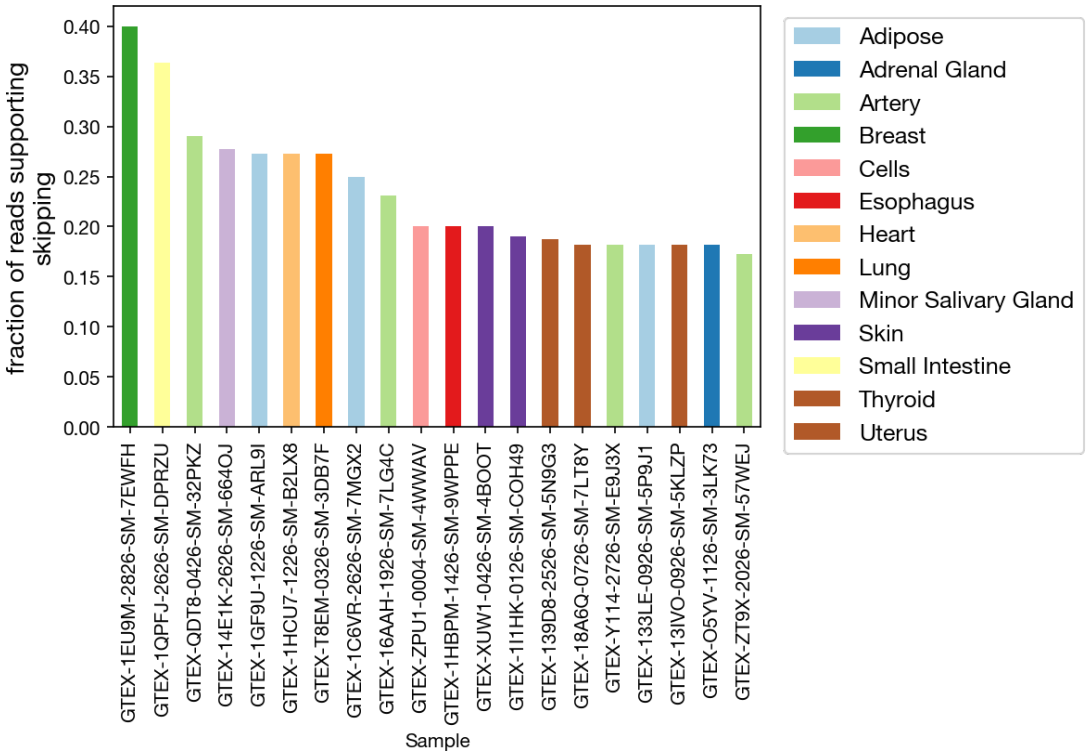

Figure 3. 9 Analysis of reads from GTEx RNA-Seq Data indicating Exon 25 skipping in alternative splicing of L1CAM

Fraction of reads mapping to L1CAM isoform supporting skipping of L1CAM Exon 25 (junction reads spanning Exon 24 and Exon 26) vs. inclusion of Exon 25 from RNA-Seq GTEx data of various human organs.

alpha-synuclein binds to the L1CAM antibody than the mIgG control (Figure 3.10), matching the enrichment of alpha-synuclein found in the prior work. This suggests that the measured changes in levels of proteins after EV immunocapture may be due to differences in nonspecific binding of free proteins to the capture antibodies highlighting the importance of performing rigorous controls to exclude this possibility.

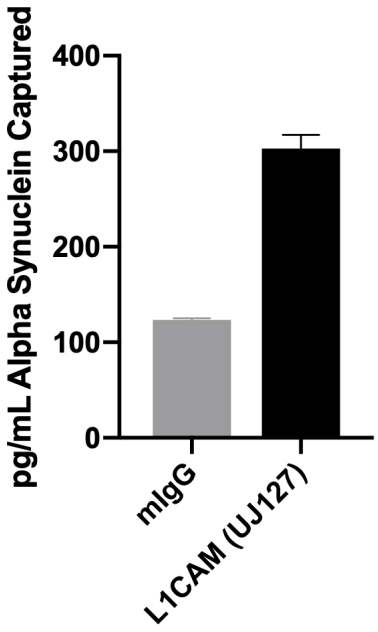

Figure 3. 10 Affinity of L1CAM for recombinant alpha-synuclein

In order to assess nonspecific binding of UJ127 to alpha-synuclein, we followed the protocol from Min Shi et al. 2014. We utilized the same L1CAM antibody (Clone UJ127, Abcam) and nonspecific mIgG control antibodies (Santa Cruz Biotechnology) but used recombinant alpha-synuclein instead of plasma [28]. We found that that three times more recombinant alpha-synuclein binds to the UJ127 antibody than the mIgG control, exactly mirroring the effect in the paper.

3.4 Discussion

Utilizing a variety of biochemical methods, we have demonstrated that L1CAM is not associated with EVs in human CSF or plasma. Although L1CAM is canonically a surface protein in neurons, we conclude that the main forms of L1CAM in plasma and CSF are soluble, possibly generated by proteolytic cleavage or alternative splicing. These finding indicate that new NDEV markers are needed. We believe that the methodology and tools present herein to investigate L1CAM can be used to validate other putative cell-type specific EV markers, not only for NDEV immunocapture, but for immunocapture of EVs from any cell. Despite this surprising result with L1CAM, we remain optimistic

regarding the potential for EVs to provide a window into the brain in accessible biofluids such as plasma [121,122], and are currently searching for other markers to isolate bona fide NDEVs from the brain.

3.5 Author Contributions

MN and DT conceived of study and designed experiments. DT, MN, WT, JHL, EJKK and RL performed experiments. DT, MN, and DRW analyzed data and wrote the manuscript with input from all authors. GMC, APC and DRW supervised the study and provided funding support.

3.6 Acknowledgements

The authors thank Alex Ng for help with stem cell differentiation and Jan Van Deun for help with density gradient centrifugation. The authors also thank Taplin Biological Mass Spectrometry Facility at Harvard Medical School and the Harvard Center for Mass Spectrometry for help with proteomics experiments. This work was supported by funding from the Chan Zuckerberg Initiative (CZI) Neurodegeneration Challenge Network, Good Ventures, NIH Center for Excellence in Genomic Science, Howard Hughes Medical Institute (HHMI), and the Klarman Cell Observatory (KCO).

3.7 Disclosures

DRW is a founder and equity holder of Quanterix. AR is a SAB member of ThermoFisher Scientific, Neogene Therapeutics, Asimov and Syros Pharmaceuticals. AR

is a cofounder of and equity holder in Celsius Therapeutics and an equity holder in Immunitas. From August 1, 2020, AR is an employee of Genentech. GMC is a founder, consultant, or advisory board member to companies listed here: http://arep.med.harvard.edu/gmc/tech.html

Chapter 4: Brain-Derived Extracellular Vesicles: *Separating* Fact from Fiction[3]

[3] Norman, M., Walt D.R. To be Submitted to *Jama Neurology.*

4.1 Introduction

BDEVs hold tremendous promise as a method for understanding the underlying biology of psychiatric and neurological disease. Because of their promise for monitoring biochemical changes in response to treatment, several clinical trials have incorporated BDEVs into their analysis of target engagement[45,61,123], and numerous upcoming trials list BDEVs in their biomarker plans[124]. However, current methods for isolating and characterizing BDEVs are still in question, and they must be rigorously scrutinized before being relied upon as a means to determine what is occurring in a patient's brain.

Recently, our lab validated novel methods for the evaluation of BDEVs, and we established that L1CAM, a marker commonly used for isolation, is a free protein in plasma and CSF and is not associated with EVs[88]. We made this discovery using size and density-based separation techniques, which demonstrate that L1CAM elutes as a free protein and not with membrane-associated EV markers such as the tetraspanins (CD9, CD63, and CD81). Following this work, we sought to apply our method to other candidate BDEV markers reported in the literature, in order to make recommendations about their utility for clinical trials and biological research. Here, we develop single molecule array (Simoa) assays to evaluate candidates from the literature, which have been used in efforts to isolate neuronal (NCAM[29,30], GLUR2[72-74]), oligodendrocyte (CNPase[78], MOG[77]), and astrocyte (GLAST[33,79]) EVs.

4.2 Methods

Bead coupling, biotinylation, cross-testing of antibodies, dilution linearity, spike-and-recovery as well as size exclusion chromatography (SEC) were performed as previously described[88]. Experiments were conducted using commercially sourced CSF and plasma. Four individual samples were used for assay validation while pooled samples were used for SEC experiments.

4.3 Results

In order to detect potential BDEVs, which are thought to be a small fraction of total EVs in the plasma, we developed high-sensitivity Simoa assays. First, we screened potential antibodies to find high-affinity pairs that work in a sandwich ELISA (calibration curves shown in Figure 4.1). Then, we validated each assay using dilution linearity (Figure 4.2) and spike-and-recovery (Table 4.1) experiments. While we were able to produce high sensitivity assays for NCAM, GLUR2, MOG, and CNPase, the reagents for GLAST did not have sufficient affinity to detect endogenous samples. NCAM and MOG could be detected in both the CSF and plasma, but GLUR2 could be detected only in the CSF and CNPase only in the plasma.

Finally, we assessed whether each target elutes in the same fractions as the tetraspanins, indicating that the protein is associated with EV membranes, or in the albumin and L1CAM fractions, indicating that it is a free protein. NCAM, GLUR2 and

MOG eluted predominantly in the free protein fraction, while CNPase eluted predominantly in the EV fractions (Figures 4.3 & 4.4).

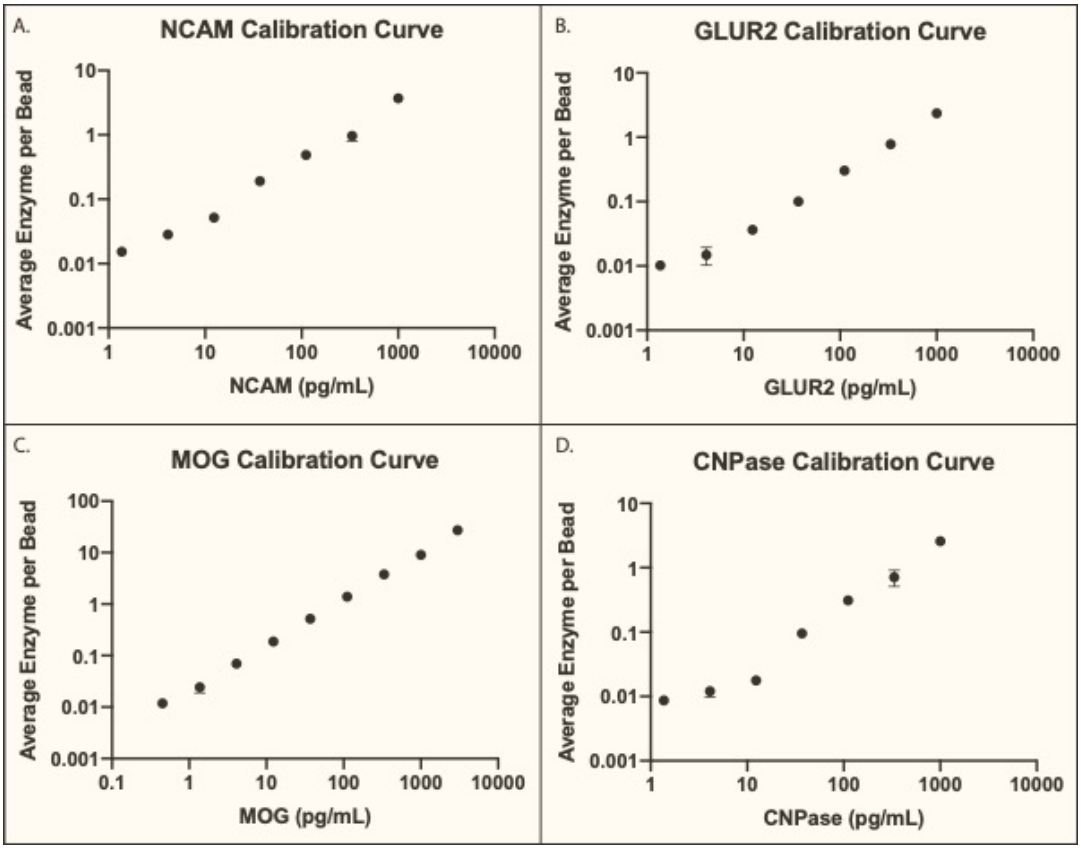

Figure 4. 1 Simoa Calibration Curves

Recombinant protein standard was serially diluted. Error bars represent the standard deviation of duplicate measurements.

a. NCAM assay
b. GLUR2 assay
c. MOG assay
d. CNPase assay

4.4 Discussion

Using SEC, we demonstrate that NCAM, GLUR2 and MOG predominantly exist as free proteins in the plasma and CSF, and therefore, like L1CAM, they should not be utilized as immunocapture targets for EVs. CNPase, on the other hand, eluted with the

a.

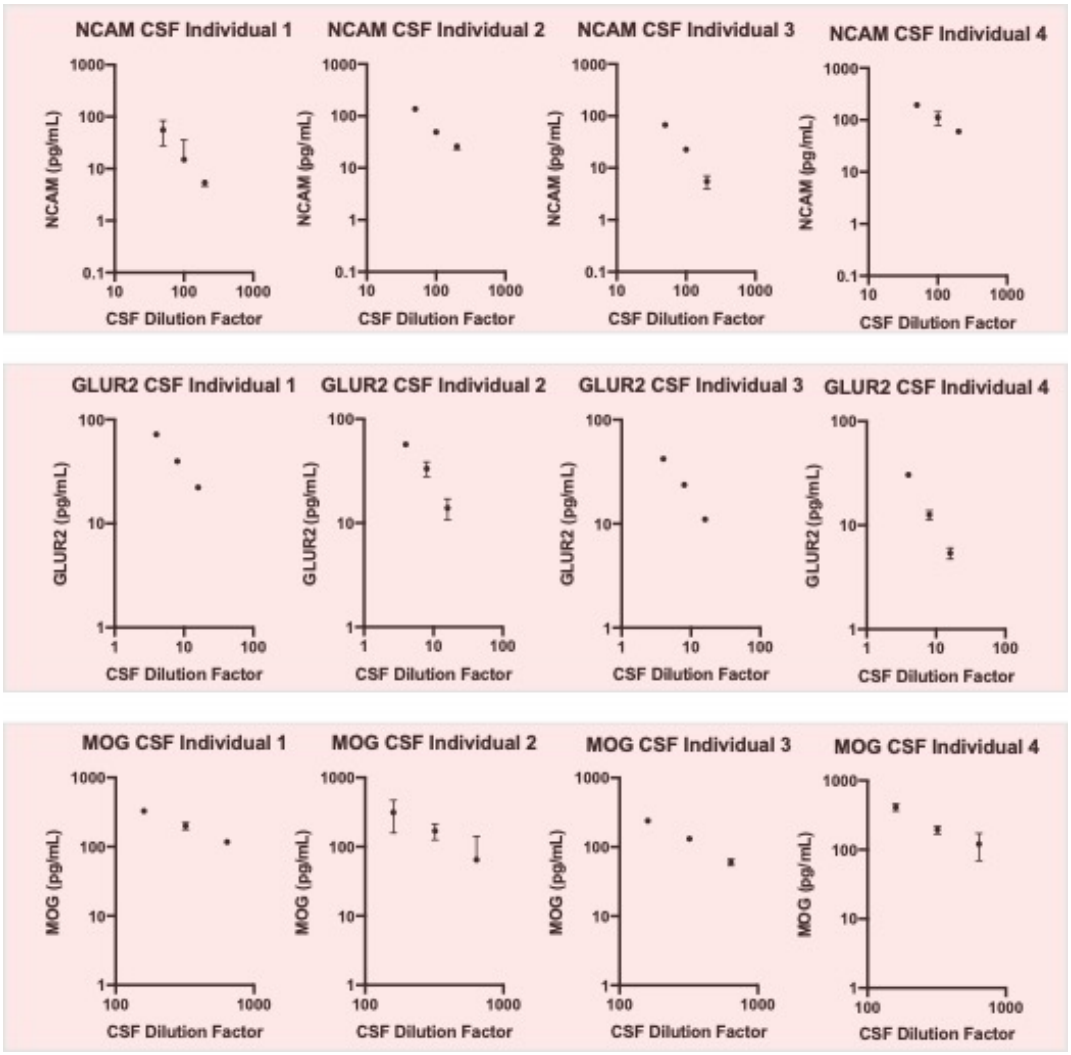
NCAM CSF Individual 1
NCAM CSF Individual 2
NCAM CSF Individual 3
NCAM CSF Individual 4
NCAM (pg/mL)
CSF Dilution Factor
GLUR2 CSF Individual 1
GLUR2 CSF Individual 2
GLUR2 CSF Individual 3
GLUR2 CSF Individual 4
GLUR2 (pg/mL)
CSF Dilution Factor
MOG CSF Individual 1
MOG CSF Individual 2
MOG CSF Individual 3
MOG CSF Individual 4
MOG (pg/mL)
CSF Dilution Factor

b.

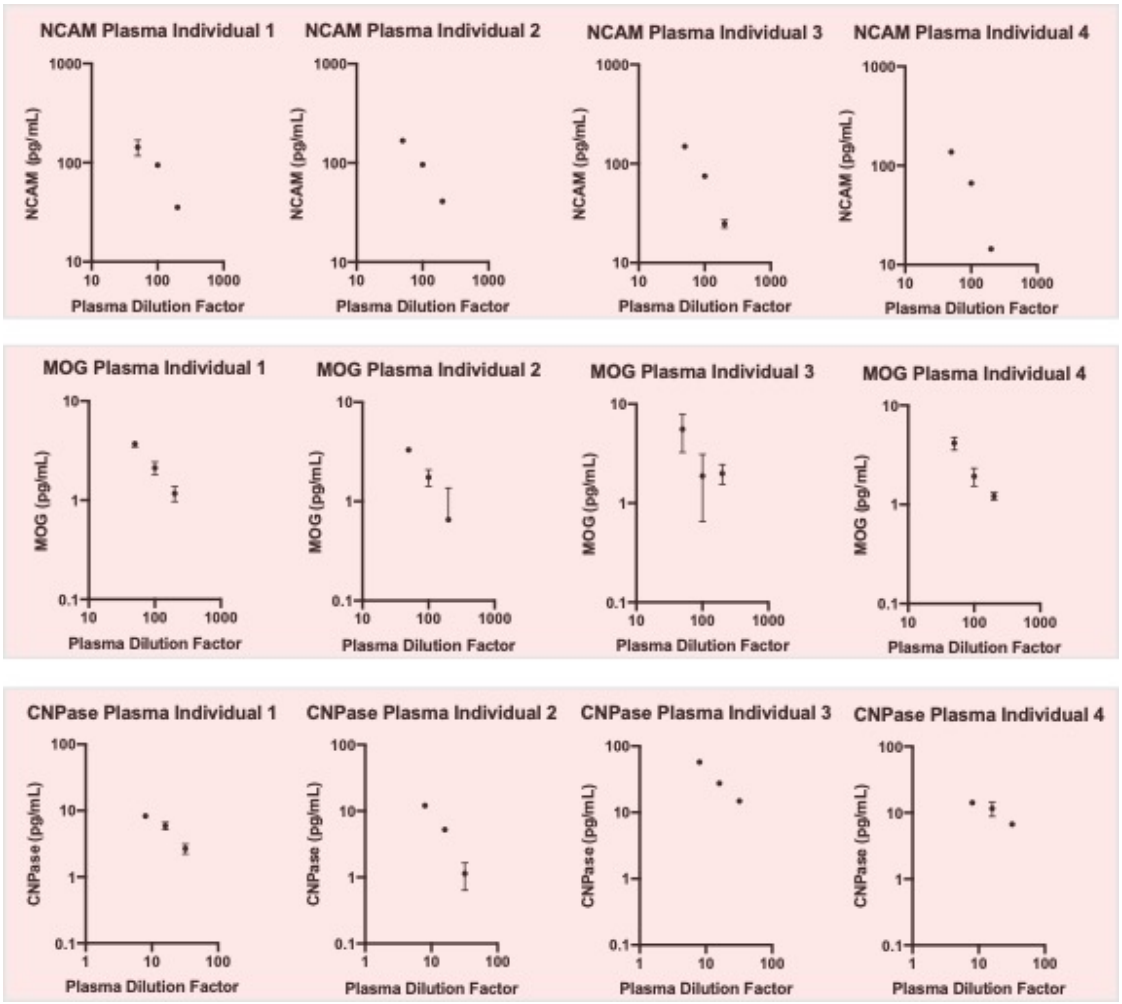

Figure 4. 2 Linearity of Dilution for Simoa Assays

We developed Simoa assays for NCAM, GLUR2, MOG and CNPase. To ensure that our assays are accurate and precise, we performed validation experiments. Each assay demonstrated endogenous dilution linearity (parallelism) in human CSF (a) and plasma (b). Error bars represent the standard deviation from two technical replicates. Each linearity experiment was performed with CSF and plasma from four individuals. CNPase was not detectable in CSF while GLUR2 was not detectable in plasma.

tetraspanins indicating it is likely membrane associated; however, it was only detectable in the plasma and not in the CSF. Interestingly, this result suggests that the EVs isolated using CNPase immunoprecipitation may originate from Schwann cells and not Oligodendrocytes as previously hypothesized[78]. Nonetheless, further validation is

warranted. Thus, we recommend against the use of L1CAM, NCAM, GLUR2 and MOG for EV isolation in clinical trials and biological research. We are actively pursuing novel targets for BDEV isolation to be used for these important research aims.

Protein	CSF Dilution Factor/Spike	Average Recovery (4 Individuals)	Plasma Dilution Factor/Spike	Average Recovery (4 Individuals)
NCAM	100x+100	108%	100x+100	70%
	100x+500	110%	100x+500	108%
GLUR2	8x+10	83%	----------	----------
	8x+100	78%	----------	----------
MOG	320x+500	116%	100x+50	88%
	320x+1000	109%	100x+100	107%
CNPase	----------	----------	16x+10	103%
	----------	----------	16x+50	90%

Table 4. 1 Spike-and-recovery for Simoa assays

We spiked the recombinant protein used for the calibration curve into human plasma and CSF and quantified the percent recovery. Each assay recovered between 70-130% of the spiked concentration, indicating good assay precision. Data averaged across four individuals and two technical replicates.

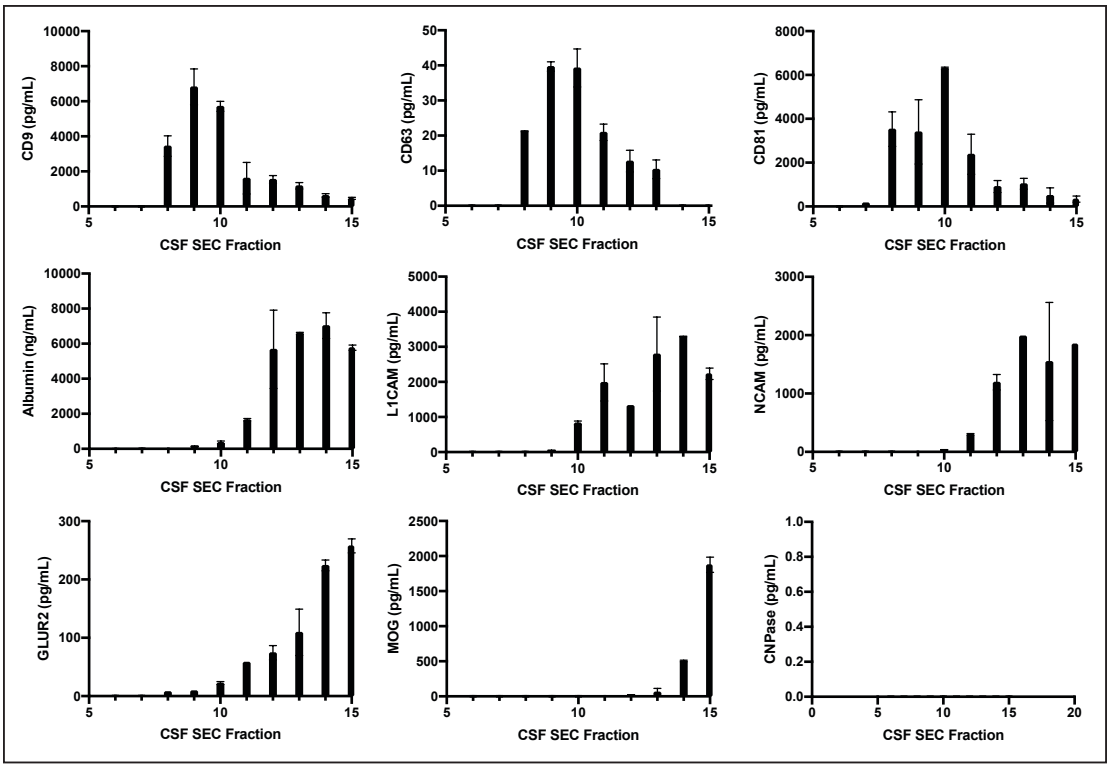

Figure 4. 3 Simoa Analysis of CSF using SEC

Simoa quantification of CD9, CD63, CD81, albumin, L1CAM, NCAM, GLUR2, MOG and CNPase in Sepharose 6B 10mL SEC fractions of pooled CSF. Error bars represent two technical replicates.

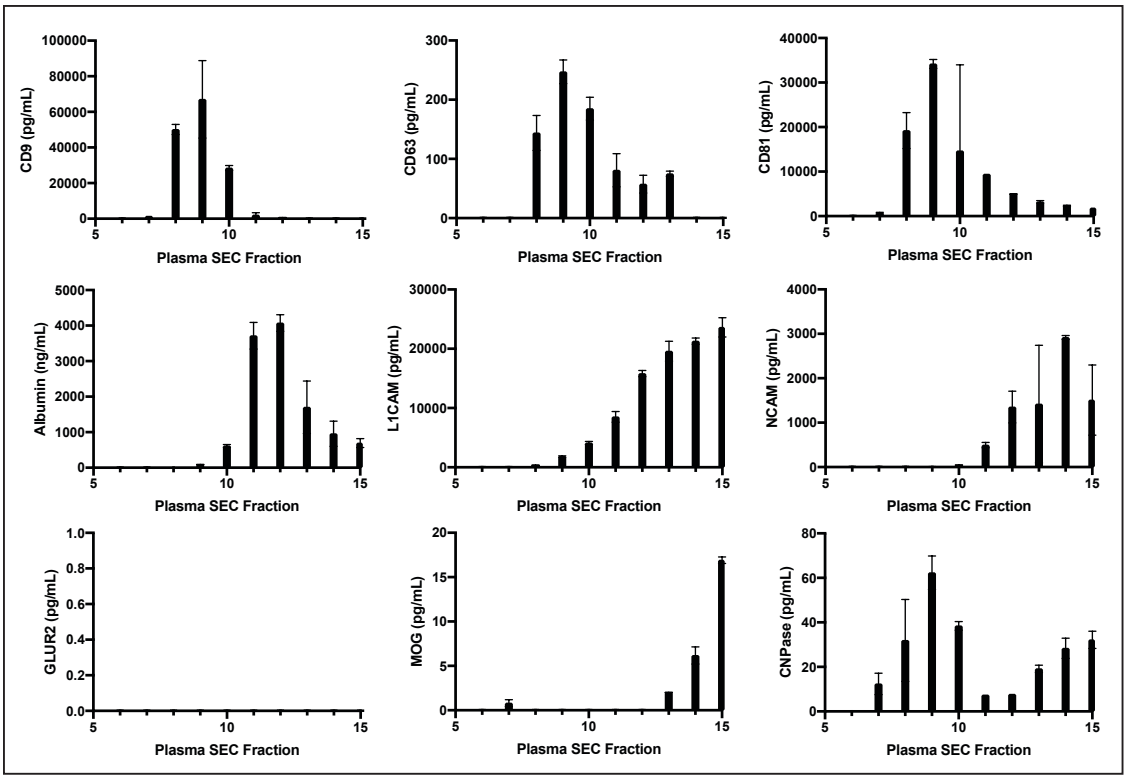

Figure 4. 4 Simoa Analysis of plasma using SEC

Simoa quantification of CD9, CD63, CD81, albumin, L1CAM, NCAM, GLUR2, MOG and CNPase in Sepharose 6B 10mL SEC fractions of pooled plasma. Error bars represent two technical replicates.

4.5 Author Contributions

DRW and MN conceived of the approach. MN performed all experiments and analysis. DRW and MN co-wrote the paper.

Chapter 5: Discussion

5.1 Do we still believe brain-derived EVs can be identified in plasma?

The evidence that brain-derived EVs cross the BBB and are present in plasma relies to some extent on the fundamental studies described in section 1.5 of this thesis. However, further confidence that brain-derived EVs are in fact quantifiable in blood was largely based upon the circular logic that over 60 publications made such claims. Given the findings herein, it is necessary to reevaluate this hypothesis. If future studies confirm that EVs do, in fact, cross the BBB, we still need to reorient our thinking about the quantity of such vesicles in peripheral biofluids like blood. It may be the case that techniques even more sensitive than Simoa will be necessary for identification and quantification. Therefore, new studies evaluating the presence or absence of BDEVs in blood must be designed and executed.

An initial step towards answering the question of whether BDEVs circulate in plasma is choosing a panel of mRNA exclusively expressed in the brain. The human protein atlas identifies 33 such genes whose transcripts cannot be detected in peripheral organs[125]. If isolation of total EVs and subsequent RT-qPCR were to locate these mRNAs, this would lend credence to the hypothesis that EVs from the brain can be present in peripheral blood. For additional confirmation, one could compare the transcripts in healthy individuals with individuals who have a BBB-disrupting disease to determine whether increased BDEVs are found due to this disruption. Finally, the same analysis can be done with high sensitivity assays for the proteins transcribed from these mRNAs in order to confirm brain specificity. Detecting these brain-specific mRNA and

protein species would be highly suggestive that EVs cross the BBB from the brain into the plasma.

Furthermore, animal experiments could play a confirmatory role, but critically these studies must be designed in a manner that will take advantage of novel technologies and allow the BBB to remain intact. For instance, one could use CRISPR to label an oligodendrocyte transmembrane protein with GFP. Oligodendrocytes are exclusively present in the CNS and not in the PNS. Finding GFP tagged EVs in plasma would confirm that EVs crossed the BBB without any injection or other disruption of the barrier. Such animal experiments coupled with the above experiments in humans would provide convincing evidence that BDEVs are present in plasma.

5.2 Identifying and validating novel markers for immunocapture of brain-derived EVs

Given our findings, it is unlikely that previously identified targets for BDEV isolation such as L1CAM, NCAM, GluR2 or MOG are in fact yielding BDEVs. If experiments such as those outlined in section 5.1 indicate that BDEVs cross the BBB and are intact in blood, then new markers must be identified, and two criteria need to be applied. First, the protein must be exclusively or predominantly transmembrane and cell-associated. In the case of L1CAM[112], NCAM[126] and MOG[127], there are known alternatively spliced or secreted isoforms. Proteins with such secreted isoforms must be ruled out during the selection process or must be demonstrated to be primarily EV-associated in biofluids using EV separation techniques such as SEC and DGC. In some

instances, as in the case of MOG, it may be possible to conduct immunocapture with a segment of the protein that is not present on the secreted form. In the example of MOG, an antibody to the carboxy terminus may yield only the membrane bound form[127]. However, we were unable to detect this isoform due to reagent limitations (data not shown). Second, proteins must be largely brain-specific at the gene expression level. While the cut off is to some degree arbitrary, L1CAM and NCAM are good examples of proteins that are heavily expressed in the periphery on non-neuronal cell-types[128]. A more stringent threshold for brain-specificity would be helpful in finding the right candidates. This can be evaluated with public databases such as GTEX which provide gene expression data for each organ[128]. Furthermore, if brain cell-type-specificity is to be claimed, then tools such as the brain RNA-Seq atlas must be utilized[129,130]. This database demonstrates for example, that neither NCAM nor GLUR2 are specific to neurons within the brain, but rather are also prevalent in oligodendrocytes and astrocytes.

After these criteria are met, it is next necessary to detect the target in the CSF and plasma. To this end, high sensitivity assays such as Simoa should be utilized. Due to the vast literature on L1CAM, the field has long perceived that the concentration of BDEVs in the blood was sufficiently high that conventional methods such as Western blotting and ELISA could be used. However, given the findings in this thesis, this may not be the case.

The subsequent step would be to demonstrate that the protein of interest predominantly elutes in the EV-associated fractions with both SEC and DGC. Immunocapture of purified EVs, following a high-yield EV extraction method such as Sepharose 6B should then be performed using a high-affinity antibody to the target, and a

high-affinity nonspecific control. As seen in our work on L1CAM it is important to use high-affinity control antibodies to account for off-target binding properties. For example, low Kd antibodies to proteins not found in the human body such as GFP or MCherry should be utilized. Once an immunocapture procedure has been established and confirmed by Western blotting, the internal contents of these EVs should be rigorously examined at both protein and RNA levels.

To properly assess the protein content of candidate BDEVs, one must apply a proteinase treatment to digest proteins outside of the BDEVs, and subsequently inactivate the proteinase before lysing the EVs as demonstrated in chapter 3. This step is critical in making reliable claims about the protein content being brain derived. Then, high-sensitivity detection assays for brain-specific proteins should be developed, and brain-specific proteins should be demonstrated to be enriched in the BDEVs compared to the nonspecific control immunocapture. qPCR for mRNAs specific to the brain should also be quantified in the immunocaptured EVs. Because mRNA cannot survive outside of EVs, no nuclease treatment is necessary.

Once it is shown that the target elutes predominantly in the EV fractions, and that the mRNA and protein within are cell-type specific, the immunocapture protocol can be justifiably used in clinical samples for analysis of brain content.

5.3 CNPase, how to further validate this target and what to use it for?

As demonstrated in chapters 3 and 4 of this thesis, the majority of targets used in the literature for BDEV isolation did not elute in the same fraction as tetraspanins in either plasma or CSF. The single exception was CNPase. This protein was initially

proposed to be an oligodendrocyte EV marker by Zhang et al. in 2018[78]. In chapter 4, I showed that CNPase elutes in the appropriate fractions; however, a great deal of validation is necessary before it can be used to learn about the cells that secrete it.

CNPase is not a transmembrane protein; rather it is a free protein, which is inserted into the membranes of oligodendrocytes and Schwann cells via palmytoylation[131]. Thus, one important milestone is demonstrating that it is present only on the cells of interest. Alternatively, one could imagine that it is released into the extracellular environment, and then associated nonspecifically with EVs due to its palmitoylation. To ensure that this is not the case, after immunocapture one must show that there is enrichment for transcripts and proteins from the myelinating cells.

An interesting, and related, issue is that Zhang et al claimed that these EVs were from brain oligodendrocytes. However, CNPase is also expressed on Schwann cells in the peripheral nervous system[132]. Moreover, in chapter 4, I demonstrate that CNPase was not detectable in the CSF but was detectable in plasma. While not definitive, this suggests that CNPase in plasma is actually derived from Schwann cells and not oligodendrocytes. To confirm whether plasma CNPase EVs are from oligodendrocytes, Schwann cells, or both, one would have to immunocapture CNPase EVs and look for mRNA and protein of molecules exclusively present in one or the other cell-type. If it is the case that CNPase is coming from peripheral Schwann cells, then it may not be useful for evaluation of Multiple System Atrophy, as reported previously, but rather it may be an excellent tool with which to study diseases of Schwann cells such as Guillian Barre Syndrome, Chronic Inflammatory Demyelinating Polyradiculoneuropathy and Charcot-Marie-Tooth

Disease[133]. However, before utilizing CNPase as an immunocapture target the above experiments must be performed.

5.4 What to measure in BDEVs and caveats about nonspecific binding

5.4.1 Understanding the fundamental mechanism of brain diseases

BDEVs have the potential to transform our understanding of the fundamental mechanisms of psychiatric and neurological diseases. By utilizing low-input methods for unbiased RNA sequencing such as single-cell RNA seq[134] and Silver seq technologies[135], researchers can sample brain transcripts from each class of brain cell and learn about the changes that occur during disease states. For example, one could look at healthy individuals, siblings of patients with bipolar disease, and patients with bipolar disease both during and between episodes. Differences in mRNA expression could lead to a better fundamental understanding of why the disease develops, and importantly what biochemical changes occur during a bipolar episode. This type of analysis is currently not possible because we are only able to assess brain cell biochemistry post-mortem, but is particularly important for diseases in which we do not understand the underlying biology and for which we do not yet have disease-modifying agents. Using BDEVs we could discover proteins not formerly known to play a role in these diseases. This new understanding would lead to novel drug discovery pathways and potentially better treatments. While bipolar disease is just one example of a poorly understood disease, the same paradigm can be applied to other psychiatric conditions for which we do not have a solid mechanistic understanding.

Such RNA sequencing techniques would also be useful in uncovering early changes in neurodegenerative diseases. The vast majority of our mechanistic understanding of neurodegenerative disease comes from the static picture of post-mortem brain tissue analysis. However, the interpretation of this brain tissue is complicated by the fact that changes in protein and RNA may be the end stage processes of cell death and may have less to do with instigating factors of disease biogenesis. Since neurodegenerative diseases can have a prodromal phase spanning several decades, it may be possible to longitudinally sample adults in their 50s with blood tests each year. Some percentage of these adults will convert to neurodegenerative diseases, and an analysis of their BDEVs will allow us to find new and improved therapeutic targets and potentially enable early diagnosis. This, of course, would not be possible with CSF as healthy individuals are unlikely to volunteer for serial lumbar punctures.

5.4.2 Methods for early detection of neurodegenerative diseases

In addition to unbiased analysis of RNA, specific methods for detection of changes in BDEVs in the prodromal phase of neurodegenerative disease may become viable strategies for early diagnosis. An important biochemical process that occurs during neurodegeneration, is post-translational modification of key proteins, and such changes can be dramatic. For example, in Lewy Bodies, the main pathological feature of PD, alpha-synuclein was shown to be 90% phosphorylated at Serine 129, while in healthy brains the phosphorylation at this residue was only 4%[136]. Similar discrepancies can be seen in other diseases with increased phosphorylation of Tau at certain sites[137]. However, attempts to leverage these modifications diagnostically in the CSF or plasma have largely

failed[138]. This is likely because these biofluids contain free floating and cell-associated kinases and phosphatases, which means captured proteins may no longer reflect their original cellular state. Furthermore, a protein like alpha-synuclein is present in many cell-types outside of the brain so the observed phosphorylation state is likely to primarily reflect these other cell-types. By measuring PTMs in BDEVs, both problems are ameliorated; the protein maintains its original phosphorylation state as it is not exposed to extracellular phosphatases and kinases, and by definition it will have originated in the brain. Therefore, measuring PTMs in BDEVs may be an important avenue for early diagnosis of neurodegenerative disease.

Another potential strategy for early detection of neurodegenerative disease is to convert RT-QuiC for use with BDEVs. RT-QuiC is a method for detecting seeds that cause neurodegeneration[2]. This technique was originally developed to detect Creutzfeldt Jacob Disease in CSF samples[2], but has since been reengineered for PD using alpha-synuclein oligomers in CSF[3]. In this protocol, a CSF sample is incubated with free alpha-synuclein monomers and ThT, and it is then shaken. If alpha-synuclein oligomers are present, monomeric alpha-synuclein will bind and aggregate onto the oligomers forming larger and larger oligomers. These oligomers will break and reform continuing to increase in number and size until the monomeric alpha-synuclein has been consumed. The ThT in solution will bind and change conformation when it encounters an aggregate due to the rotational immobilization of the central C-C bond connecting the benzothiazole and aniline rings, and it will fluoresce[139]. Alternatively, if no aggregated alpha-synuclein seeds are present, then the alpha-synuclein cannot aggregate onto and no new oligomers will be formed. Thus, in a sample with alpha-synuclein oligomer seeds, such as an

individual with Parkinson's Disease or Lewy Body Dementia, fluorescence will increase over time, whereas in a healthy individual fluorescence will stay constant and low.

While RT-QuiC already shows great promise in CSF, it is not practical or even possible to conduct early diagnosis using this biofluid. Population screening with CSF will not occur because the number needed to test for PD diagnosis will not justify a population level screen with lumbar puncture. However, by switching from using RT-QuiC in CSF to blood via BDEVs, population-level screening for neurodegenerative diseases would be enabled. This early detection may enable intervention prior to massive cell loss.

5.4.3 Use of BDEVs for testing target engagement in clinical trials

Currently, it is challenging to assess target engagement in neurological and psychiatric clinical trials. This is typically attempted by measuring downstream pathway targets in CSF; however, this is often not indicative of the intracellular target engagement. BDEVs in plasma offer a potential solution to this problem. For example, in Parkinson's Disease, many trials of LRRK2 inhibitors have failed to show efficacy. Yet, it is not clear whether LRRK2 inhibitors even enter the brain cells. To test target engagement, surrogate markers like total urinary EV LRRK2, have been used, but these are likely to reflect the LRRK2 contents of kidney cells, not brain cells. Transitioning away from total EVs or CSF to BDEVs may help us pinpoint whether the issue is a lack of penetrance into brain cells, a lack of target engagement within the brain cells, or that target engagement was achieved but downstream effects did not stop or slow the neurodegenerative process. By incorporating BDEV analysis into clinical trials of

neurodegenerative and psychiatric disease, we may be able to obtain higher success rates, and when trials fail, improve future trial design in a more informed manner.

5.5 Conclusion

Despite setbacks to the field of BDEVs outlined in this thesis, I remain optimistic that when properly isolated and analyzed, these vesicles will contribute tremendously to our understanding of the human brain and its pathologies. The ability to noninvasively sample brain cells in living human patients as they experience disease, progress through its stages, and respond to medication will unlock new possibilities for early diagnosis and better management of neurological and psychiatric diseases. However, as described in this thesis, many challenges remain. It is clear that a substantially more rigorous scientific standard needs to be applied to the identification of targets for BDEV isolation and for assaying their internal contents. I am hopeful that the tools, methods and framework developed in this thesis will be part of a course-correction in BDEV research, allowing the field to fulfill its promise of being a true window into the brain.

Chapter 6: Appendix 1. High Sensitivity Single Molecule Array Assays for Pathological Isoforms in Parkinson's Disease[4]

[4] Norman, M., Gilboa, T., Walt, D. 2022. *Clin Chem.* 68 (3): 431-440.
Reprinted here with permission from publisher.

6.1 Introduction

PD is a devastating neurodegenerative disease characterized by the death of dopamine producing neurons in the Substantia Nigra[140]. Currently, there are no approved treatments that slow this degeneration, and dopamine replenishment remains the mainstay of symptomatic treatment[140]. Encouragingly, however, there are dozens of registered clinical trials examining disease modifying agents. The majority of these trials target specific pathological isoforms and post-translational modifications (PTMs) known to play a role in PD pathophysiology[141]. By pairing clinical metrics with measurements of these target isoforms, clinical trials seek to evaluate the efficacy of potential therapeutic compounds and associated target engagement[141]. These assays can also be used as a selection criterion to enroll patients with the desired levels and to balance participants across treatment arms. Thus, carefully validated, high-resolution, isoform-specific assays are crucial. However, these isoforms and PTMs can be challenging to measure in complex biological fluids such as CSF. Because PTMs generally comprise a small subset of the total protein, their concentration levels are difficult to detect with conventional methods such as ELISA. Additionally, interactions in biological matrices resulting in non-specific binding are a greater concern when attempting to discriminate between different isoforms of the same protein. Consequently, the assays must be rigorously validated to ensure the values obtained reflect only the specific isoform in question[142].

Here, we developed a panel of high sensitivity Simoa assays and validated their specificity in CSF. We selected analytes that are associated with a diverse set of pathological processes inherent to PD pathophysiology. These include markers of alpha

synuclein and tau aggregation, as well as more general indicators of neural degeneration and inflammation. We demonstrate the analytical specificity and sensitivity of our Simoa assays, and their ability to detect these low-abundance isoforms in a large cohort of PD patients and Neurological Controls (NC).

6.2 Methods

Bead coupling, biotinylation, cross-testing of antibodies, dilution linearity and spike and recovery were performed as previously described[88]. Dephosphorylation assays were carried out using Lambda Phosphatase (New England Biolabs). All validation experiments were conducted using commercially sourced CSF. For clinical validation of assay utility, samples were obtained from the NINDS PDBP biobank. Use of these samples for biomarker validation was approved by the Partners IRB. All sample measurements were taken in duplicate using the Quanterix HD-X instrument (Billerica MA).

6.3 Results

6.3.1 Simoa Assay Development and Validation

We developed a panel of Simoa assays to detect proteins, post-translational modifications and pathological isoforms implicated in PD pathophysiology (Figure 6.1). Simoa is a digital form of ELISA in which single immunocomplexes are trapped on magnetic beads and loaded into microwell arrays. The arrays are comprised of 216,000 microwells, each with space to confine only a single bead[18]. At low concentrations of

analyte, this technique facilitates the detection of signal from single protein molecules instead of having to rely upon total fluorescence from large numbers of molecules, as in traditional ELISA. While Simoa was originally designed to detect unmodified proteins, the sandwich immunoassay format is also amenable to the detection of specific protein isoforms and post-translational modifications.

For assays in which pathological isoforms or post-translational modifications were measured, we conducted further validation to ensure that these assays did not cross react with the unmodified or wild-type proteins (Figure 6.3). In the case of pSer129 alpha synuclein and pSer396 tau, we conducted two types of specificity experiments. First, we dephosphorylated the recombinant protein standard using Lambda Phosphatase. We demonstrated that this dephosphorylation did not affect the total levels of alpha synuclein or tau, but it completely eliminated the signal in the phospho-specific assay. Second, to ensure that the signal in CSF was caused by an interaction with the phosphorylated form, we dephosphorylated CSF samples and observed no decrease in the total levels of alpha synuclein or tau but a reduction of the phospho-assay signal to background level. We then sought to determine whether the filament alpha synuclein assay was specific to the filament pathological isoform. To do so, we measured varying concentrations of a monomeric recombinant alpha synuclein using the filament assay and saw no increase in signal at physiological alpha synuclein concentrations. Furthermore, our dilution linearity experiments for the filament assay demonstrated linearity in PD patients, but absence of the isoform in healthy controls (Figure 6.2).

We began by screening numerous antibody pairs for each target biomarker in order to find high affinity reagents with demonstrated specificity for the target of interest.

Calibration curves for each assay are shown in Figure 6.1, with limits of detection (LOD) and lower limits of quantification (LLOQ) in the attomolar and femtomolar range, a substantial improvement upon currently available assays (Table 6.2). We validated these assays using dilution linearity (parallelism) and spike and recovery experiments (Figure 6.2 & Table 6.1).

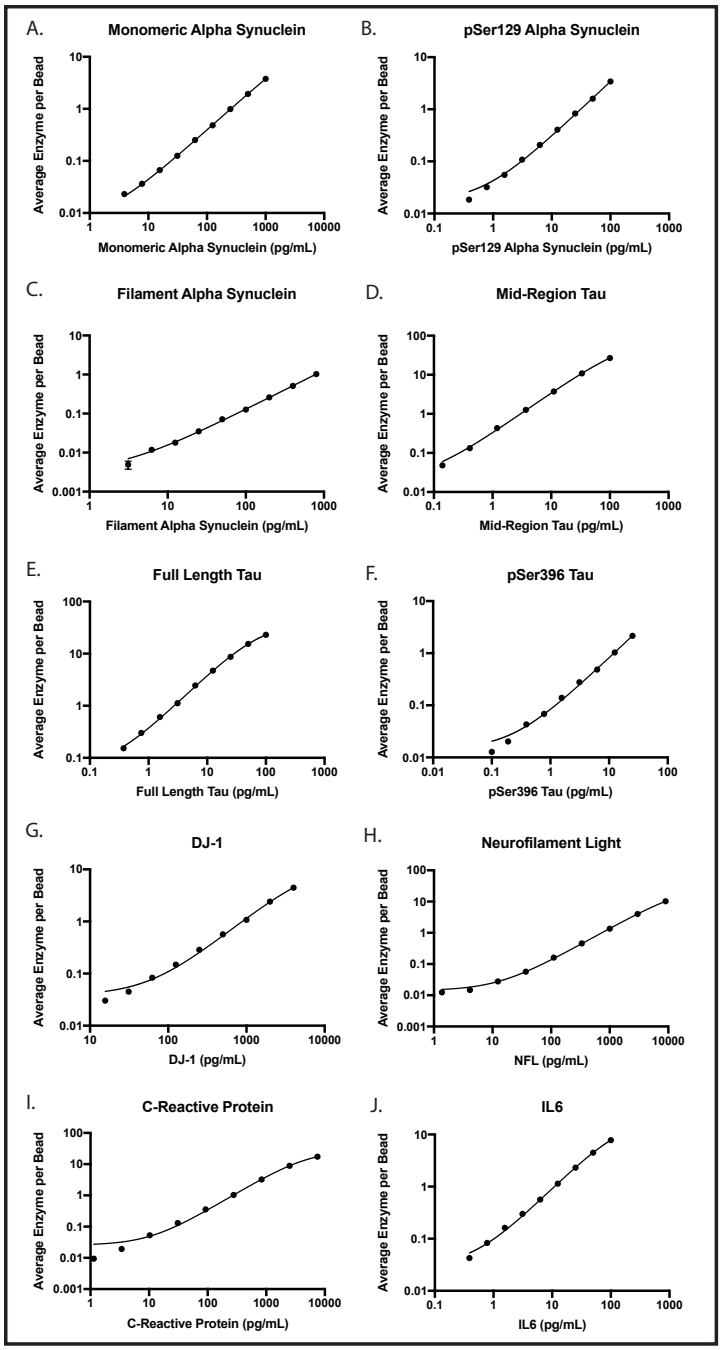

Figure 6. 1 Calibration curves for each Simoa assay

Recombinant protein standard was serially diluted. Error bars represent the standard deviation of duplicate measurements. A 4PL curve with $1/y^2$ weighting was fit to each curve.

a. Total Alpha Synuclein Assay
b. pSer129 Alpha Synuclein Assay
c. Filament Alpha Synuclein Assay
d. Mid-range Tau Assay
e. Full-length Tau Assay
f. pSer396 Tau Assay
g. DJ-1 Assay
h. Neurofilament Light Assay
i. C-reactive protein Assay
j. IL-6 Assay

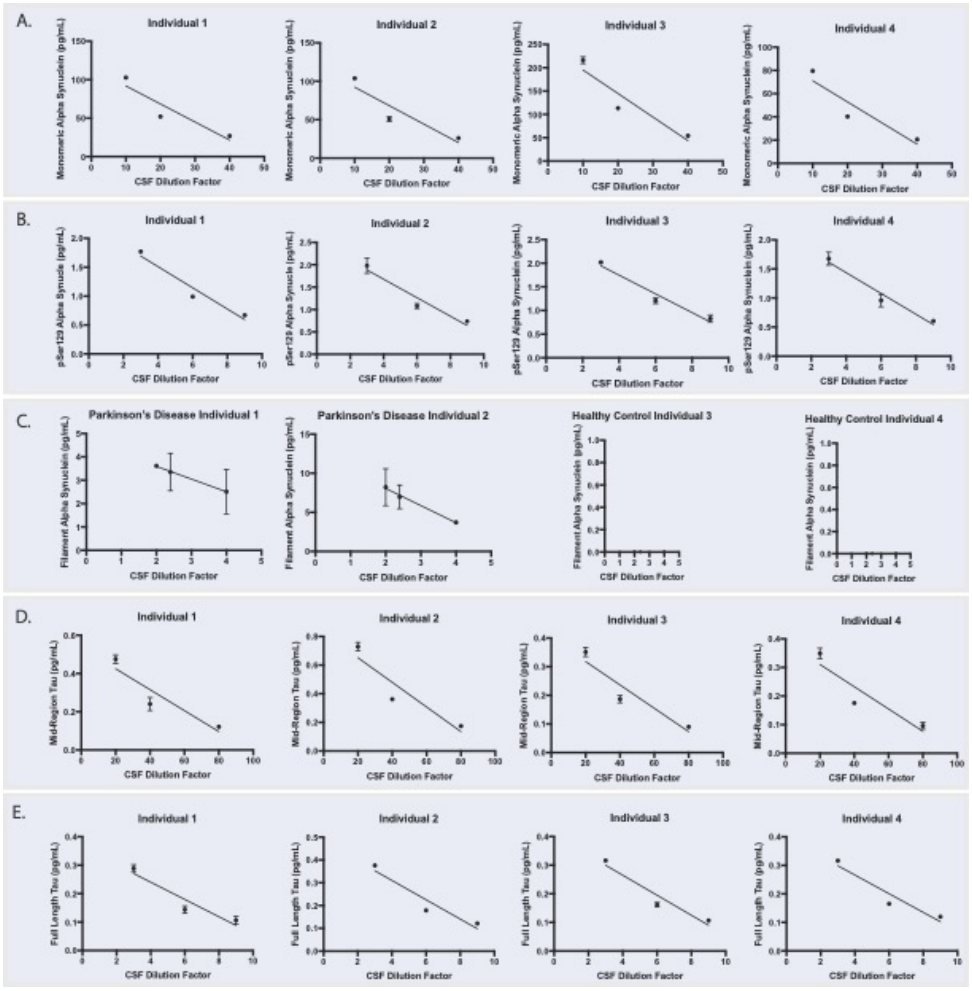

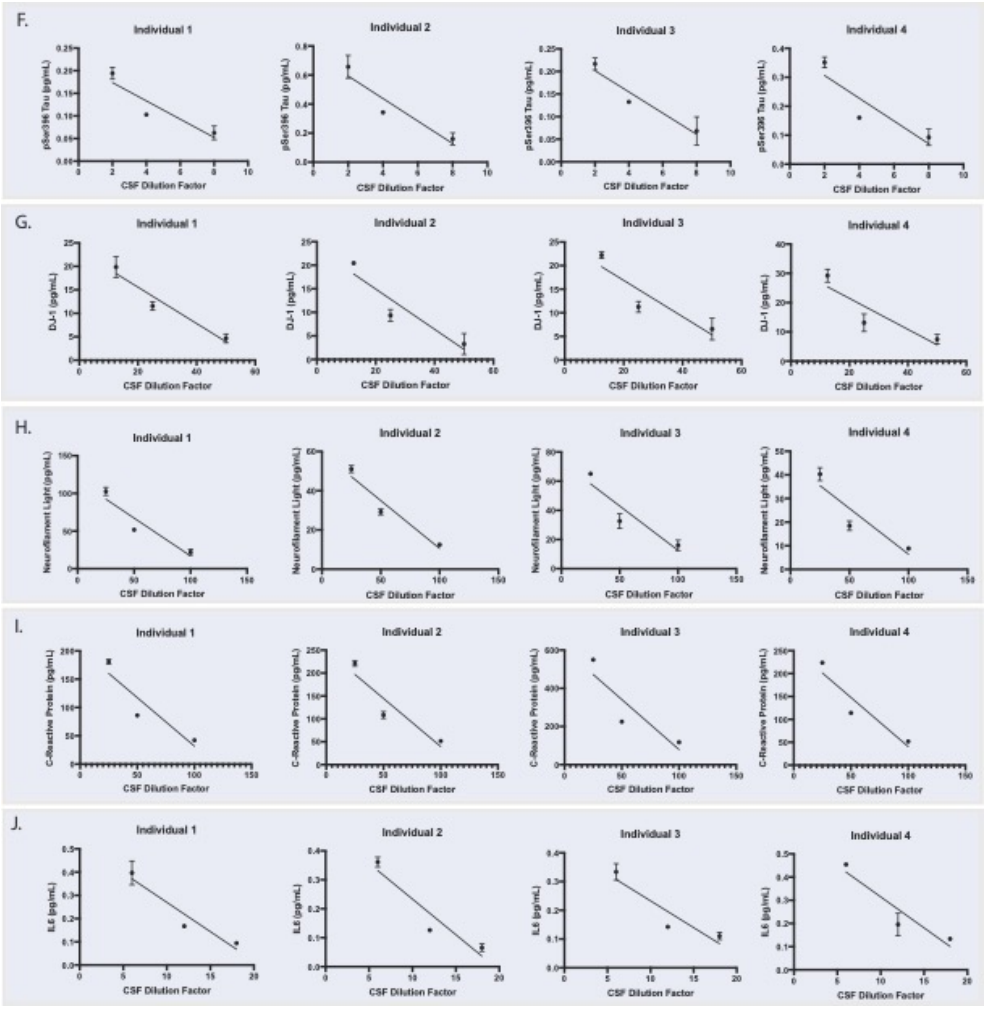

Figure 6. 2 Dilution Linearity (Parallelism) Simoa assays

Each assay was tested on four samples. Error bars represent the standard deviation of duplicate measurements. Concentration values were interpolated based on the curve in Figure 6.1.

a. Total Alpha Synuclein Assay (four commercial CSF samples, diagnosis unknown)
b. pSer129 Alpha Synuclein Assay (four commercial CSF samples, diagnosis unknown)
c. Filament Alpha Synuclein Assay (two commercial Parkinson's Disease and two commercial Neurological Control CSF samples)
d. Mid-range Tau Assay (four commercial CSF samples, diagnosis unknown)
e. Full-length Tau Assay (four commercial CSF samples, diagnosis unknown)
f. pSer396 Tau Assay (four commercial CSF samples, diagnosis unknown)
g. DJ-1 (four commercial CSF samples, diagnosis unknown)
h. Neurofilament Light (four commercial CSF samples, diagnosis unknown)
i. C-reactive protein (four commercial CSF samples, diagnosis unknown)
j. IL-6 (four commercial CSF samples, diagnosis unknown)

	Spike 1 Concentration (pg/mL)	Average % Recovery in CSF for Spike 1 (Averaged Across 4 Individuals)	Spike 2 Concentration (pg/mL)	Average % Recovery in CSF for Spike 2 (Averaged Across 4 Individuals)
Alpha Synuclein	10	85	100	87
pSer129 Alpha Synuclein	1	98	10	92
Filament Alpha Synuclein	50	67	100	63
Mid-Region Tau	1	106	10	100
Full Length Tau	1	105	10	102
pSer396 Tau	1	90	10	84
DJ-1	200	108	1000	100
Neurofilament Light	50	106	200	98
C-Reactive Protein	500	95	1000	100
IL-6	10	116	50	119

Table 6. 1 Spike and recovery for Simoa assays

Each value is the average of four samples each run in duplicate. The samples used are the same as those in Figure 6.2 for each sample. Spike concentrations were chosen to be proportional to the concentration of the analyte in the CSF.

6.3.2 Assessment of the clinical utility of our Simoa panel for diagnosis of Parkinson's Disease

In order to assess the diagnostic utility of our panel, we measured these targets in 100 Parkinson's Disease (PD) patients and 100 Neurological Controls (NC) from the NINDS Parkinson's Disease Biomarker Program (PDBP) Biobank. The groups were

	Calculated LOD (pg/mL)	Calculated LLOQ (pg/mL)	% of samples detectable	Average CV above LOD (%)
Alpha Synuclein	1.3922	4.3429	100	3.8
pSer129 Alpha Synuclein	0.2534	0.6618	100	5.9
Filament	1.096	3.3128	81	21.5
Full Length Tau	0.0026	0.0085	100	7.8
Mid Range Tau	0.0021	0.0078	99	21.9
p396 Tau	0.003	0.0102	100	12.8
DJ-1	0.9427	3.1844	100	16.5
Neurofilament Light	0.1767	0.4637	100	6
C-reactive protein	0.6751	2.1077	100	3.3
IL-6	0.0375	0.1139	53.5	24.6

Table 6. 2 Assay performance of Simoa Assays in Clinical cohort

The limit of detection (LOD) was calculated by first taking the mean of the background and adding three times the standard deviation. The concentration was then determined by fitting to a calibration curve, which was fit to a 4PL with 1/y2 weighting. The limit of quantification (LOQ) was calculated by adding ten times the standard deviation to the background and then using the calibration curve to obtain the concentration.

matched for key parameters such as site of collection, age, sex and hemoglobin contamination (Table 6.3). Parkinson's patients in this cohort were on average 5.7 years since diagnosis. Of all the PD patients, 90% were medicated, with 75% on Levodopa therapy. With the exception of IL-6, all analytes were detectable in the vast majority of

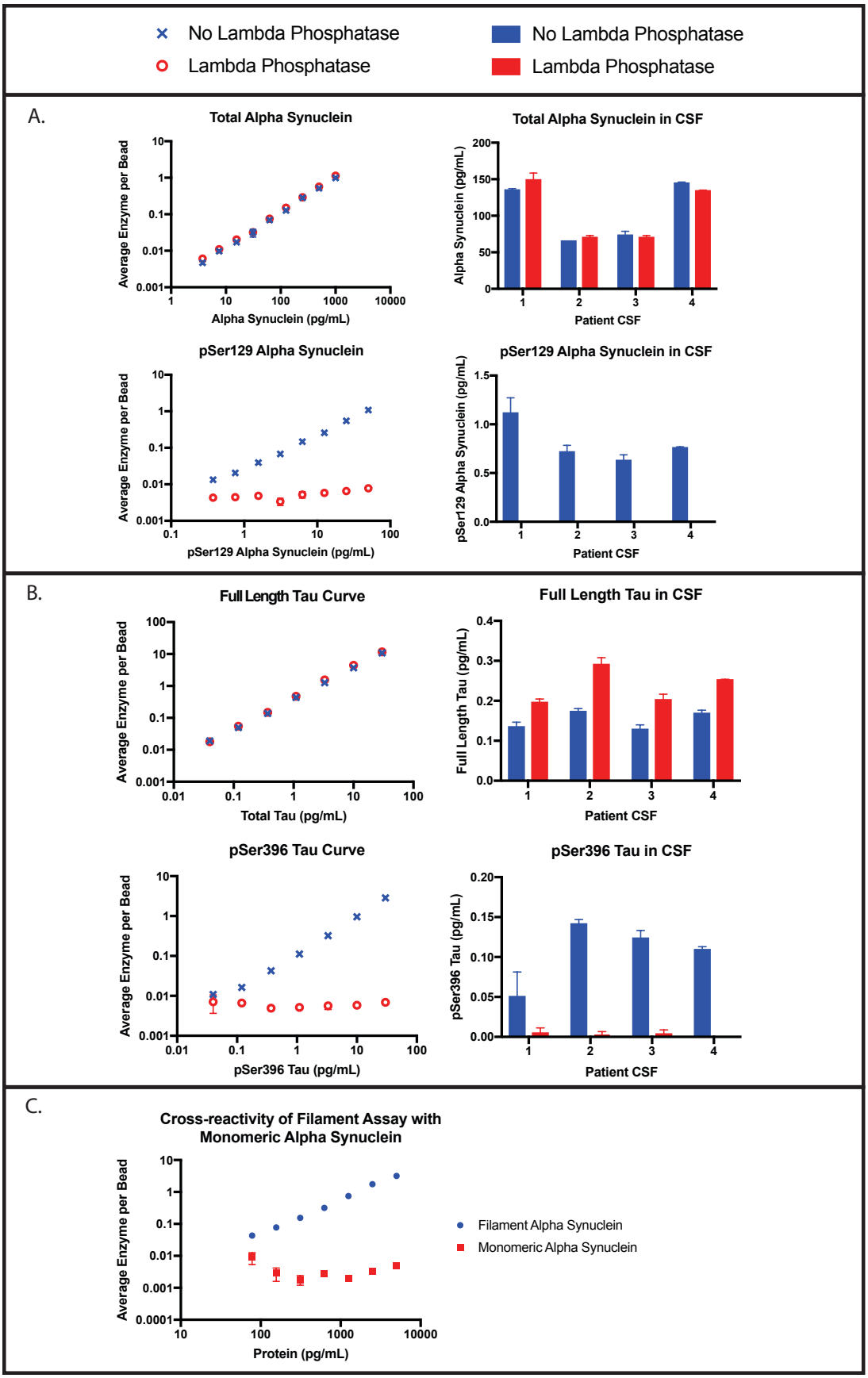
No Lambda Phosphatase
Lambda Phosphatase
No Lambda Phosphatase
Lambda Phosphatase
A.
Total Alpha Synuclein
Average Enzyme per Bead
Alpha Synuclein (pg/mL)
Total Alpha Synuclein in CSF
Alpha Synuclein (pg/mL)
Patient CSF
pSer129 Alpha Synuclein
Average Enzyme per Bead
pSer129 Alpha Synuclein (pg/mL)
pSer129 Alpha Synuclein in CSF
pSer129 Alpha Synuclein (pg/mL)
Patient CSF
B.
Full Length Tau Curve
Average Enzyme per Bead
Total Tau (pg/mL)
Full Length Tau in CSF
Full Length Tau (pg/mL)
Patient CSF
pSer396 Tau Curve
Average Enzyme per Bead
pSer396 Tau (pg/mL)
pSer396 Tau in CSF
pSer396 Tau (pg/mL)
Patient CSF
C.
Cross-reactivity of Filament Assay with Monomeric Alpha Synuclein
Average Enzyme per Bead
Protein (pg/mL)
Filament Alpha Synuclein
Monomeric Alpha Synuclein

Figure 6. 3 Specificity verification of assays for post-translational modifications and pathological isoforms

a. Top left: Quantification of total alpha synuclein using recombinant pSer129 alpha Synuclein standard with (red) or without (blue) lambda phosphatase treatment.
Bottom left: Quantification of pSer129 alpha synuclein using recombinant pSer129 alpha synuclein standard with (red) or without (blue) lambda phosphatase treatment.
Top left: Quantification of total alpha synuclein in CSF with (red) or without (blue) lambda phosphatase treatment.
Bottom left: Quantification of pSer129 alpha synuclein in CSF with (red) or without (blue) lambda phosphatase treatment.
b. Top left: Quantification of full length tau using recombinant GSK Beta phosphorylated tau standard with (red) or without (blue) lambda phosphatase treatment.
Bottom left: Quantification of pSer396 tau using recombinant GSK Beta phosphorylated tau standard with (red) or without (blue) lambda phosphatase treatment.
Top left: Quantification of full length tau in CSF with (red) or without (blue) lambda phosphatase treatment.
Bottom left: Quantification of pSer396 tau in CSF with (red) or without (blue) lambda phosphatase treatment.
c. Measurement of recombinant filament (blue) or monomeric (red) alpha synuclein using the filament alpha synuclein assay.

	Healthy Control	Parkinson's Disease
Age (years)	63.3	63.4
Gender	50F:50M	51F:49M
Time Since Diagnosis (years)	NA	5.7
Baseline MDS-UPDRS Score	6.9	48.2
Baseline MOCA Score	26.8	26.4
Hemoglobin in CSF (ng/mL)	32.4	32.6
% On medication for PD	NA	90%
% On Levodopa	NA	75%

Table 6. 3 Demographic characteristics of PD and NC CSF samples used to assess Simoa panel

Mean values shown for the PD and NC groups.

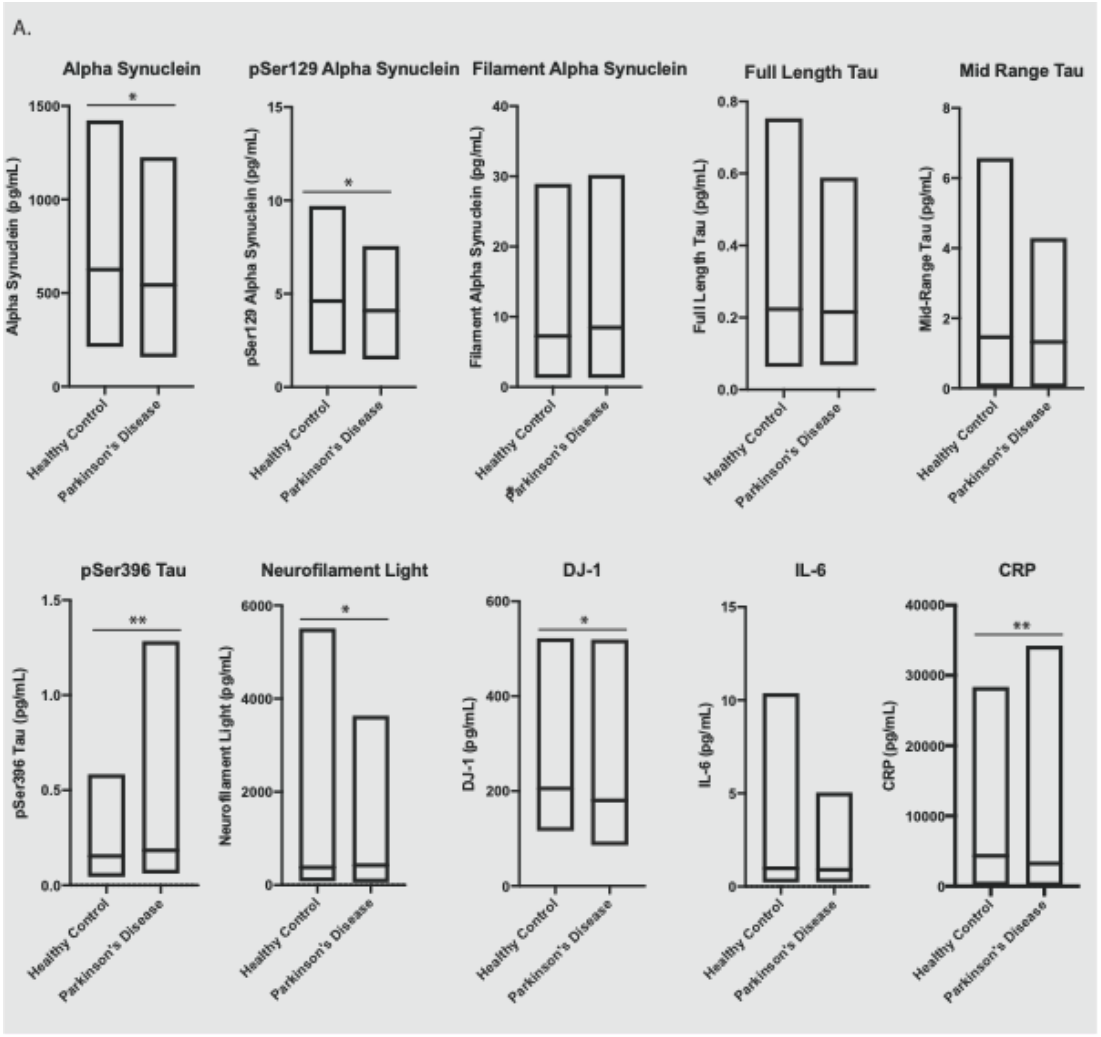
A.
Alpha Synuclein
Alpha Synuclein (pg/mL)
1500
1000
500
0
*
Healthy Control
Parkinson's Disease
pSer129 Alpha Synuclein
pSer129 Alpha Synuclein (pg/mL)
15
10
5
0
*
Healthy Control
Parkinson's Disease
Filament Alpha Synuclein
Filament Alpha Synuclein (pg/mL)
40
30
20
10
0
Healthy Control
Parkinson's Disease
Full Length Tau
Full Length Tau (pg/mL)
0.8
0.6
0.4
0.2
0.0
Healthy Control
Parkinson's Disease
Mid Range Tau
Mid-Range Tau (pg/mL)
8
6
4
2
0
Healthy Control
Parkinson's Disease
pSer396 Tau
pSer396 Tau (pg/mL)
1.5
1.0
0.5
0.0
**
Healthy Control
Parkinson's Disease
Neurofilament Light
Neurofilament Light (pg/mL)
6000
4000
2000
0
*
Healthy Control
Parkinson's Disease
DJ-1
DJ-1 (pg/mL)
600
400
200
0
*
Healthy Control
Parkinson's Disease
IL-6
IL-6 (pg/mL)
15
10
5
0
Healthy Control
Parkinson's Disease
CRP
CRP (pg/mL)
40000
30000
20000
10000
0
**
Healthy Control
Parkinson's Disease

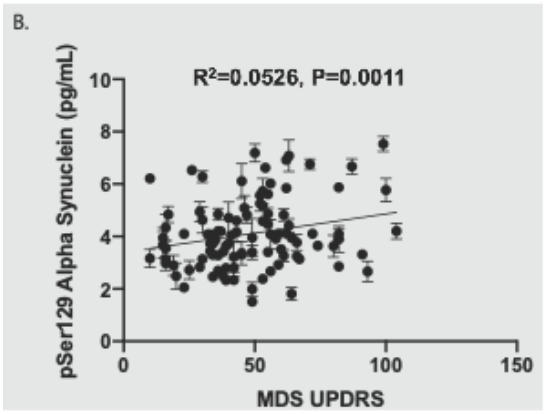
B.
pSer129 Alpha Synuclein (pg/mL)
R²=0.0526, P=0.0011
10
8
6
4
2
0
0
50
100
150
MDS UPDRS

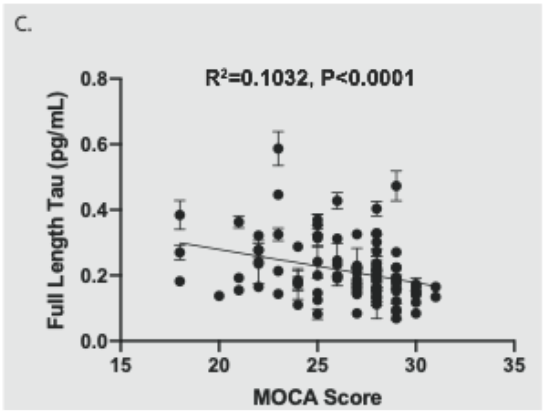
C.
Full Length Tau (pg/mL)
R²=0.1032, P<0.0001
0.8
0.6
0.4
0.2
0.0
15
20
25
30
35
MOCA Score

Figure 6. 4 Assessment of panel in PD and NC cohorts

a. Box plots of Simoa assay values for 100 PD and 100 NC samples. Each sample's value is the average of duplicate measurements fit to the calibration curve in Figure 6.1, multiplied by the dilution factor. Lines represent minimum, mean and maximum values for each group. Mann-Whitney test results are represented with * for values <0.05 and ** for values <0.005.
b. Linear regression analysis between total MDS UPDRS and pSer129 alpha synuclein values. Error bars represent the standard deviation of duplicate measurements.
c. Linear regression analysis between total MOCA score and full length tau values. Error bars represent the standard deviation of duplicate measurements.

Trial	Mean Nested 10x10 Fold Cross Validation AUC for Random Forest Analysis
1	0.6817
2	0.7168
3	0.7038
4	0.6832
5	0.6924
6	0.7052
7	0.7073
8	0.6992
9	0.7077
10	0.7185
Average	**0.7016**

Table 6. 4 Random Forest Analysis of Simoa panel using all 10 markers

Nested 10x10 fold cross-validation Random Forest Analysis using all 10 markers in the Simoa panel.

samples, with low coefficients of variation (CVs) for the samples above the limit of detection (Table 6.1).

6.4 Discussion

With the increasing adoption of fluid biomarkers in clinical trials, the need for rigorously validated measurements of pathological isoforms is growing. Ultrasensitivity is essential to the measurement of PTMs and critical for monitoring small changes in treatment response. In our work we employed Simoa technology, developed in our laboratory, and created highly specific and sensitive assays for PTMs and pathological isoforms relevant to PD pathophysiology. Experiments involving dilution linearity, spike and recovery, and isoform specificity were performed in order to determine the accuracy and precision of the measurements. Thorough assay validation as performed here should be utilized in clinical trials for all isoform specific assays in order for the scientific community to have confidence in the measurements and to rule out matrix effects especially at concentration levels near background.

These initial results for diagnostic applications are promising, but there is room for improvement by including additional targets. The use of a panel and examination of the relationship between different biomarkers is more relevant than simple analysis of the mean value for individual markers. Additionally, investigating these analytes over time is likely to be more informative than assessing a single timepoint in a patient's disease. Upcoming trials for disease modifying agents can utilize the assays described herein to quantify small fluctuations in the levels of these isoforms in order to better understand dose response and drug penetration into the CSF and further elucidate mechanisms of therapeutic efficacy.

6.5 Author Contributions

DRW and MN conceived of the approach. MN performed all experiments and analysis. DRW and MN co-wrote the paper.

Chapter 7: Appendix 2. Ultra high-resolution profiling of early seroconversion in patients with COVID-19[5]

[5] Norman, M, Gilboa, T., Ogata, A.F., Maley, A.M., Cohen, L., Busch, E.L., Lazatovits, R., Mao, C.P., Cai, Y., Zhang, J., Feldman, J.E., Hauser, B.M., Caradonna, T.M., Chen, B., Schmidt, A.G., Alter, G., Charles, R.C., Ryan, E.T., Walt, D.R. 2020. *Nature Biomedical Engineering*. 4, 1180-1187.

Reprinted here with permission from publisher.

7.1 Introduction

Severe acute respiratory syndrome coronavirus-2 (SARS-CoV-2) is a novel beta-coronavirus that has caused the coronavirus disease 2019 (COVID-19) pandemic [143-145]. In order to identify infected individuals and contain the spread of the disease, rapid and accurate population-wide screening is essential. Currently, nucleic acid amplification tests (NAATs) of nasopharyngeal (NP) swabs are the primary method used to identify SARS-CoV-2 infected individuals [144]. These tests can diagnose disease during a narrow window of active infection and have limited clinical sensitivity [146-149]. Thus, additional complementary methods are needed to identify individuals who are or have been infected with SARS-CoV-2. Robust serological assays that detect antibodies against SARS-CoV-2 can fulfill this critical need. These assays could be used to identify symptomatic infected individuals who have tested negative by NAATs. Furthermore, serological assays could be used to identify individuals who have been infected with SARS-CoV-2 and were asymptomatic or had mild symptoms, thereby providing a better understanding of how widespread the virus is within a population. This information can aid epidemiologists in determining a more accurate population prevalence of COVID-19 and contribute to contact tracing operations, key to curbing the pandemic[150]. Finally, antibody testing will be necessary in order to run highly powered and accurate prevention trials[151].

Many serological ELISA have been recently developed to detect anti-SARS-CoV-2 antibodies. However, these assays have important limitations [146,152-162]. First, most assays lack the ability to detect antibodies at early stages of infection. Second, false positive results can occur due to non-specific binding from high levels of pre-existing

antibodies in blood [142]. Finally, these assays lack the resolution to quantify changes in the immune response over time, which may be key in understanding clinical progression.

To address these limitations, we developed an ultra-sensitive, multiplexed Single Molecule Array (Simoa) assay for immunoglobulin isotypes against immunogenic SARS-CoV-2 proteins, providing us with detailed information about the immune response to SARS-CoV-2 at early stages and throughout the course of infection[18]. Simoa provides up to 1,000-fold improvement in analytical sensitivity over standard ELISA [163,164]. This ultra-sensitivity enables samples to be highly diluted resulting in significantly reduced non-specific binding. Additionally, unlike the standard ELISA, Simoa has a wide dynamic range and allows precise quantification of multiple analytes over a concentration range of four orders of magnitude. This feature is particularly important since antibody levels can vary greatly among individuals and may fluctuate significantly during different stages of infection within the same individual, and thus it is advantageous to have a single assay format that can accurately measure antibody levels over a wide concentration range.

7.2 Methods

7.2.1 Plasma samples for the discovery cohort

Clinical samples were obtained from patient presenting to the Massachusetts General Hospital with viral respiratory symptoms. Plasma collection was performed with a variety of tube types. SARS-CoV-2 infection was confirmed by RT-PCR on nasopharyngeal specimen (n=19 RT-PCR negative samples and n=42 RT-PCR positive samples from 21 individuals taken at two timepoints). Additional plasma samples

collected from healthy adults pre-pandemic (January –December 2019) prior to travel internationally were also included in the analysis (n=20). All samples were collected under approval of the Institutional Review Board for Human Subjects Research at Massachusetts General Hospital. Human plasma samples were heat inactivated (56°C for 60 minutes). Samples were diluted in Homebrew Sample Diluent (Quanterix) to their final dilution factor which varied for each experiment, as described in the results section. All sample measurements had two technical replicates which were averaged.

7.2.2 Plasma samples for the training cohort

Clinical samples were obtained from patients presenting to Brigham and Women's Hospital with viral respiratory symptoms (n=172 samples from 91 individuals taken at different timepoints that tested positive and n=100 samples from 95 individuals taken at different timepoints that tested negative). Of the SARS-CoV-2 positive cohort, 10 patients were immunosuppressed encompassing 31 timepoints. SARS-CoV-2 infection was confirmed by RT-PCR on nasopharyngeal specimen. Additional samples were obtained from the Partner's Biobank which includes pre-pandemic samples from before October 1, 2019 from individuals that presented with a recent respiratory infection (n=100), or patients who had no record of viral or bacterial infection in their medical record (n=100). All samples were collected under approval of the Partners Institutional Review Board for Human Subjects Research. In this training cohort, all plasma was collected in purple top tubes and samples were not heat inactivated. Samples were diluted in Homebrew Sample Diluent to their final dilution factor.

7.2.3 Plasma samples for the validation cohort

68 samples were from 28 adults who tested positive for SARS-CoV-2 using NP RT-PCR within the last 5-34 days. The remaining 232 samples were pre-pandemic controls all collected before October 1, 2019 which included (1) 20 patients with bacterial pneumonia in the past 31 days, (2) 20 patients with unspecified pneumonia in the past 31 days, (3) 50 patients with URI within the past 31 days, (4) 42 patients with a confirmed viral respiratory illness within the past 31 days and (5) 100 healthy individuals with no recorded respiratory viruses in their medical history. In this validation cohort, all plasma was collected in purple top tubes and samples were not heat inactivated. Samples were diluted in Homebrew Sample Diluent to their final dilution factor. All samples were collected under approval of the Partners Institutional Review Board for Human Subjects Research.

7.2.4 RBD Expression and Purification

SARS-2 RBD (GenBank: MN975262.1) was cloned into pVRC vector for mammalian expression (FreeStyle 293F or Expi293F suspension cells). The construct contains a HRV 3C-cleavable C-terminal SBP-His_{8X} tag. Supernatants were harvested 5 days post-transfection and passaged directly over Cobalt-TALON resin (Takara) followed by size exclusion chromatography on Superdex 200 Increase (GE Healthcare) in 1x phosphate-buffered saline. Typical yields from FreeStyle 293F cells are approximately 9 mg/liter culture. Affinity tags were removed using HRV 3C protease (ThermoScientific) and the protein repurified using Cobalt-TALON resin to remove the

protease, tag and non-cleaved protein. RBD sequence and purification validation are provided in the Figure 7.1.

7.2.5 Preparation of a stabilized ectodomain of spike protein

To express a stabilized ectodomain of spike protein, a synthetic gene encoding residues 1−1208 of SARS-CoV-2 spike with the furin cleavage site (residues 682–685) replaced by a "GGSG" sequence, proline substitutions at residues 986 and 987, and a foldon trimerization motif followed by a C-terminal 6xHisTag was created and cloned into the mammalian expression vector pCMV-IRES-puro (Codex BioSolutions, Inc, Gaithersburg, MD). The expression construct was transiently transfected in HEK 293T cells using polyethylenimine. Protein was purified from cell supernatants using Ni-NTA resin (Qiagen), the eluted fractions containing S protein were pooled, concentrated, and further purified by gel filtration chromatography on a Superose 6 column (GE Healthcare), following a protocol described previously [165]. Negative stain electron microscopy (EM) analysis was performed as described [166]. Additional information is provided in Figure 7.2.

7.2.6 Bead Coupling & Verification

Recombinant SARS-CoV-2 antigens (nucleocapsid, RBD, S1 and spike) were coupled to four types of dye-encoded 2.7 μm carboxylated paramagnetic beads (Quanterix) using EDC (1-ethyl-3-(3-dimethylaminopropyl)carbodiimide hydrochloride) chemistry (ThermoFisher Scientific 77149). The nucleocapsid and S1 antigens were sourced commercially (nucleocapsid: Ray Biotech 230-30164 and S1: Sino Biological

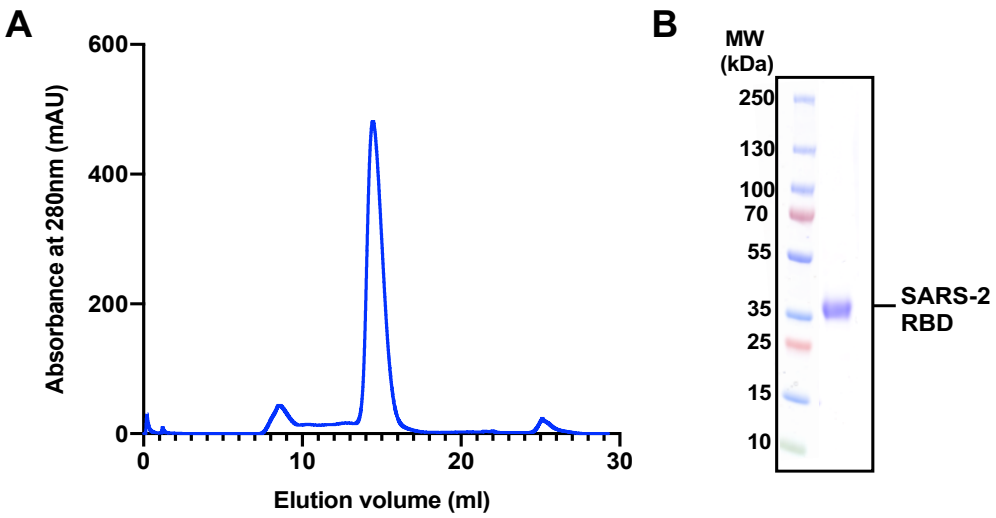

Figure 7. 1 Purification and biochemical characterization of SARS-CoV-2 (SARS-2) RBD.

a) Representative size exclusion chromatography profile of SARS-2 RBD eluting at approximately 14.5 ml.
b) SDS-PAGE analysis (reducing conditions) of the purified SARS-2 RBD.

V0591-V08H). The spike and RBD antigens were produced in the labs of Bing Chen and Aaron Schmidt, respectively, as described above. 2.8×10^8 beads were washed three times with 200 µL of Bead Wash Buffer (Quanterix), three times 200 µL of Bead Conjugation Buffer (Quanterix), and then resuspended in 300 µL of Bead Conjugation Buffer. Immediately prior to use, 10 mg of EDC was reconstituted in 1 mL of Bead Conjugation Buffer. To activate the beads for conjugation, EDC was added to the bead suspension and the beads were agitated on a HulaMixer (ThermoFisher Scientific) for 30 minutes at 4°C. After activation, the beads were washed once with 200 µL of Bead Conjugation Buffer, and then resuspended in 300 µL of Bead conjugation buffer containing the antigen. Beads were agitated on the HulaMixer for 2 hours at 4°C. The antigen-conjugated beads were washed two times with 200 µL of Bead Wash Buffer, and

then blocked with BSA (Bovine serum albumin) for 30 minutes at room temperature in 200 µL of Bead Blocking Buffer (Quanterix). The blocked beads were washed with 200

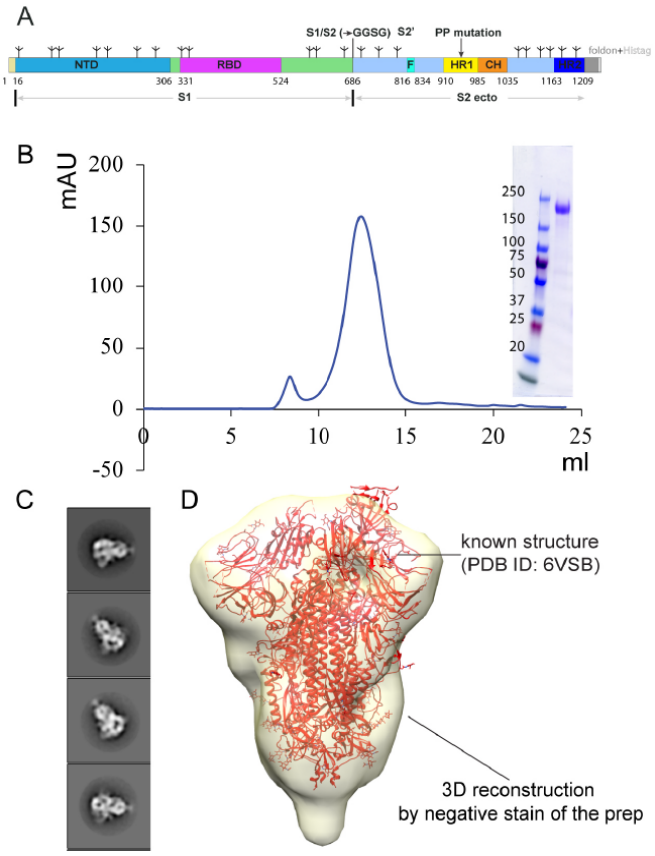

Figure 7. 2 Spike protein sequence and purification validation

Production of a stabilized S ectodomain trimer in the prefusion conformation.
a. Schematic representation of the construct design. Various segments include: NTD, N-terminal domain; RBD, receptor-binding domain; S1/S2, S1/S2 cleavage site; S2', S2' cleavage site; F, fusion peptide; HR1, heptad repeat 1; PP mutation, two proline residues introduced to stabilize the prefusion conformation; CH, central helix region; HR2, heptad repeat 2; foldon trimerization tag and a His tag; and tree-like symbols for glycans.
b. The purified S ectodomain trimer was resolved by gel-filtration chromatography. Inset, fractions of the peak were analyzed by Coomassie stained SDS-PAGE.
c. Negative stain EM of the S trimer showing representative 2D class averages, box size 220 Å.
d. 3D reconstruction showing the defined shape of S trimer, superimposed with the atomic model of S trimer (PDB: 6VSB).

μL of Bead Wash Buffer, 200 μL of Bead Diluent (Quanterix), and resuspended in 200 μL of Bead Diluent. The amount of recombinant protein and EDC used in each reaction are as follows: nucleocapsid (20μg antigen, 2μL EDC), RBD (20μg antigen, 6μL EDC), S1 (20μg antigen, 6μL EDC), and spike (16.67μg antigen, 6μL EDC). nucleocapsid, spike, S1, and RBD were conjugated to 488 nm, 647 nm, 700 nm, and 750nm dye-encoded beads, respectively. Beads were counted using a Beckman Coulter Particle Counter and stored at 4°C.

Antigen coupling to the beads was confirmed by an anti-His tag assay for spike, S1, and nucleocapsid beads and by an anti-RBD assay for RBD beads (Figure 7.3). For spike, S1, and nucleocapsid, confirmation of antigen attachment to the beads was demonstrated by Simoa with His tags experiments using a biotinylated anti-His tag antibody (ThermoFisher MA121315BTI) on the HD-X Analyzer (Quanterix). The anti-His-tag antibody was plated at concentrations of 0.1 pg/mL to 10,000 pg/mL using tenfold dilutions. RBD was provided without a His-tag, therefore RBD beads were used as a control against the anti-His tag antibody assay. RBD conjugation to beads was confirmed by Simoa with an anti-RBD antibody (clone CR3022) and a biotinylated anti human-IgG antibody (Bethyl Laboratories A80-148B). Nucleocapsid beads were used as a control for these experiments due to the ability of anti-RBD antibody binding to RBD, S1, and spike protein but not nucleocapsid.

7.2.7 Biotinylation

Detection antibodies for IgA, IgG and IgM were purchased from Thermo Fisher, Bethyl Laboratories, Abcam, Biolegend, and R&D systems (see Immunoglobulin Simoa

assay format) and were biotinylated for use in Simoa assays as described previously by Cohen et al [167]. Briefly, the antibodies were passed through an Amicon filter three times in Biotinylation Reaction Buffer (Quanterix). Antibody concentrations were determined using NanoDrop One Spectrophotometer. Antibodies were conjugated to biotin using EZ-Link NHS-PEG4 Biotin (Thermo Fisher Scientific) by resuspending NHS-PEG4-Biotin in dionized H_2O. For all immunoglobulins a NHS-PEG4-Biotin was added in 40x molar excess and incubated for 30 min. All biotinylated antibodies were then purified using three washes in an Amicon filter.

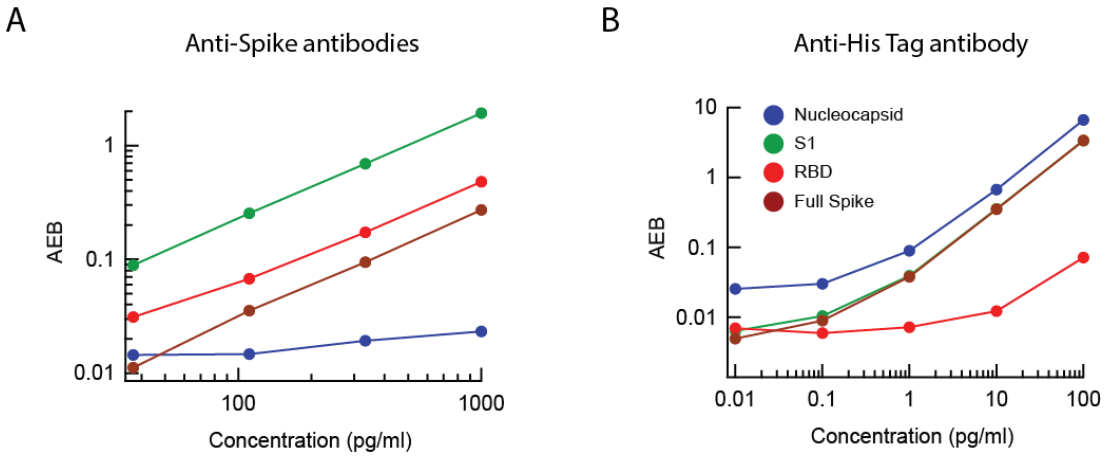

Figure 7. 3 Bead coupling validation

In order to confirm that coupling was successful, we tested the beads in two ways. First, we tested the three proteins which had His tags. To that end we loaded all four beads and used a biotinylated anti-his tag antibody for detection in decreasing quantities. As expected, the three His tagged proteins gave high signal while the RBD protein, which had its His tag removed, gave low signal. Next, to ensure the RBD protein had also been conjugated properly to the bead, we introduced a recombinant human anti-RBD domain antibody (CR3022) and used an anti-human IgG biotinylated detector to complete the immunocomplex. Since the Spike protein and S1 also contain the RBD domain we expected that the antibody would bind to all three, but that it would not bind to the nucleocapsid protein.

In order to identify the highest affinity anti-IgM and anti-IgA antibodies, we screened candidates using a sandwich Simoa immunoassay for detection of the given immunoglobulin. In this screening process a commercially available human-plasma-derived immunoglobulins (IgM Sigma-Aldrich I8260 and IgA Sigma-Aldrich I4036) were used as our protein standard in a sandwich Simoa assay. We then cross-tested each anti-IgM or anti-IgA antibody as a capture antibody against all other candidate IgM or IgA antibodies as detectors in order to establish high binding affinity on the Simoa platform. This was done separately for IgM and IgA. Tight binders were selected for further analysis. Below, are tables indicating signal to noise ratios (SNR) for each antibody pair.

IgA detector	411502	MAB4787	AB214003	AB224184	A80109B	AB128739	AB128731
411502		10.59	41.94	48.74	115.36	14.79	1.25
MAB4787	0.16		121.78	4.81	25.7	64.51	4.13
AB214003	61.49	13.28		28.72	58.25	3.88	1.08

Table 7. 1 IgA detector cross-testing

IgM detector	MII401	MII402	MAB9435	MAB94351	314502	A80-100B
MII401		3.62	1.59	1.29	41.60	NaN
MII402	33.01		1.14	1.30	23.48	NaN
MAB9435	1.04	1.00		1.10	0.19	0.89
MAB94351	0.94	1.04	0.32		NaN	0.35
314502	15.75	2.72	0.80	0.91		5.49

Table 7. 2 IgM detector cross-testing

Since the antibodies to be screened for IgG detection were mouse, rabbit and goat IgGs, we could not screen them using the above method because of species cross-reactivity. Instead, we screened anti-IgG detector antibodies using a mixture of three commercially available recombinant human IgGs to S1 (Creative Biolabs CR3022, CBFYR-0119, CBFYR-0120) and the four viral epitopes coated beads (spike, S1, RBD and nucleocapsid). As expected, the beads that showed high SNR are those that have an RBD domain (RBD, S1, Spike) but not the nucleocapsid. A80-148B was chosen for further analysis due to its high SNR.

IgG Detector	A80-148B	410701	409302
Nucleocapsid bead SNR	**2.68**	1.34	1.44
S1 bead SNR	**216.29**	143.28	10.11
RBD bead SNR	**66.31**	15.77	24.42
Spike bead SNR	**651.27**	4.69	34.34

Table 7. 3 IgG detector cross-testing

7.2.8 Immunoglobulin Simoa assay format

Simoa experiments were performed in an automated three-step assay format onboard the HD-X Analyzer (Quanterix Corp) as described in Rivnak et al [19]. Human plasma samples were diluted in Homebrew Detector/Sample Diluent (Quanterix). Anti-human immunoglobulin antibodies were diluted in Homebrew Detector/Sample Diluent to final concentrations of: IgG (Bethyl Labratories A80-148B): 7.73ng/mL, IgM (Thermo Fisher MII0401): 216ng/mL, IgA (Abcam ab214003): 150ng/mL. Streptavidin-β-galactosidase (SβG) concentrate (Quanterix) was diluted to 30 pM in SβG Diluent (Quanterix). System Wash Buffer 1, System Wash Buffer 2, RGP, and Simoa Sealing Oil

were purchased from Quanterix and loaded onto the HD-X Analyzer per the manufacturer's instructions. In the first step of the assay, 25μL of the four SARS-CoV-2 antigen-coupled multiplex beads were incubated with 100μL of diluted human plasma for 15 minutes. The total number of beads used per reaction was 475,000 (125,000 each of nucleocapsid, RBD, and S1 beads and 100,000 of spike beads). After incubation, six wash steps were performed with System Wash Buffer 1. In the second step, the beads were resuspended in 100 μL of the respective biotinylated anti-human immunoglobulin antibody and incubated for 5.25 minutes, and then washed six times with System Wash Buffer 1. In the third step, the beads were resuspended in 100μL of SβG, incubated for 5.25 minutes and washed six times. The beads were resuspended in 25 μL of RGP before being loaded into the microwell array for analysis. Following bead loading, the microwell array was sealed with oil and imaged in five optical channels. AEB values were calculated by the software in the HD-X Analyzer. The assay was validated as described in the Supplementary Information.

7.2.9 Data Analysis

Duplicate measurements per sample were obtained for each of the twelve immunoglobulin and viral target combinations. The average of duplicate measurements was calculated. For cohort 2, in each run, four calibrators were included for each assay. These calibrators were produced by serial dilution of SARS-CoV-2 positive individuals

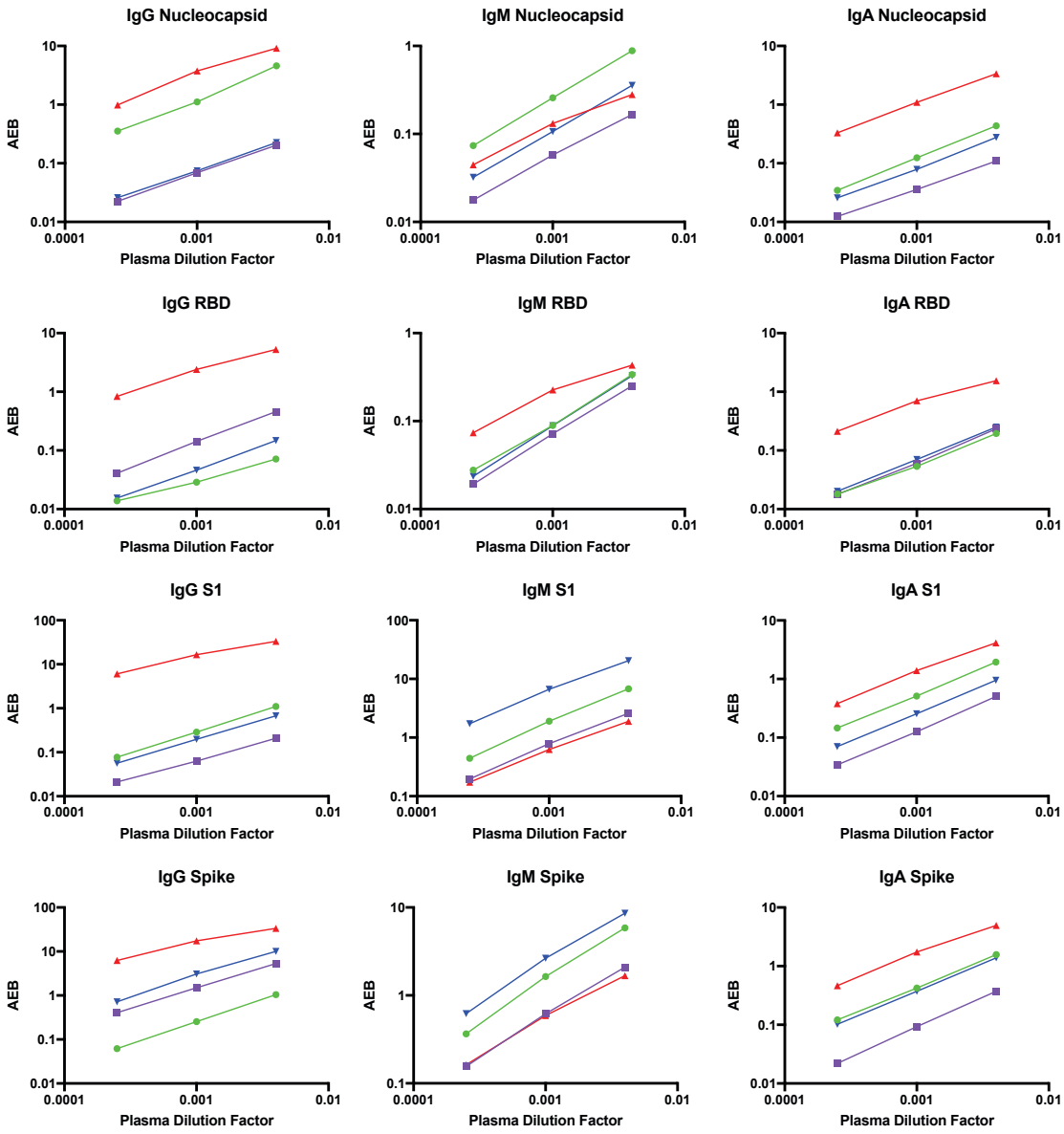

Figure 7. 4 Linearity of dilution for all immunoglobulin assays

Four COVID 19+ patient samples were diluted three times (250x, 1000x & 4000x). Below we demonstrate that in all 12 assays the AEB values (signal) diluted linearly for all patients.

Spiked concentration (pg/ml)	Dilution factor	AEB	Measured concentration (pg/ml)	% Recovery
250	250	0.128359	230.5	92.2
250	500	0.138653	251.1	100.4
250	1000	0.142077	258.1	103.2
1000	250	0.425218	892.7	89.3
1000	500	0.423456	888.1	88.8
1000	1000	0.408272	849.8	85.0

Table 7. 4 Spike and recovery for IgG assay

In order to establish that the assays were accurate and quantitative, we created a calibration curve using three recombinant human IgG antibodies to S1 that we serially diluted (Creative Biolabs CR3022, CBFYR-0119, CBFYR-0120). We then spiked these antibodies into pre-pandemic pooled human plasma (BIOIVT) in order to show good recovery at relevant dilution factors. We did not have recombinant IgM or IgA human antibodies to SARS-CoV-2, so this validation could only be done for IgG.

who were not included in either cohort 1 or 2. These calibrators were used to normalize samples run between batches.

For modeling, the mean of marker duplicate values was calculated and then log-transformed. The logistic regression outcome reference group was all pre-pandemic control samples. In different models, the outcome index group was all SARS-CoV-2 positive cases, early-stage cases, or late-stage cases.

Prior to modeling, five-fold cross validation was performed to identify subsets of predictive markers. Two cross validations were run: first, early-stage cases and pre-pandemic controls, and second, late-stage cases and all controls. For each cross validation, every included participant was randomly assigned to one of five groups. For each of five folds, one group was held out as a test set and the other four groups

combined were the training set. Using PROC ADAPTIVEREG in SAS, each training set started from a model of all 12 markers and worked backwards to an intercept-only model. Of all the models run on a given training set, the one yielding the smallest cross validation error was identified as the fold-specific model. The generalized cross validation criterion (GCV) was the measure of the fold-specific model's predictive accuracy. The contribution of each variable to the fold-specific model was measured by its importance, defined as the square root of the GCV value of the fold-specific model from which all basis functions involving the variable had been removed, minus the square root of the GCV value of the selected model, then scaled to set the largest importance value to 100. To validate the data, in each test set, predicted probabilities of the outcome were calculated using the markers with an importance of at least 60 in the respective training set. Predicted probabilities from the various test sets were then merged together to estimate area under the receiver operating characteristic (ROC) curve across the test sets.

The final markers selected from each cross validation were those with an importance of at least 60 in at least 3 of the 5 training sets. Thus, there were three panels of markers: the "full" model of all 12 markers measured, a subset identified by the cross validation of controls and early stage cases, and a subset identified by the cross validation of controls and late stage cases.

Model discrimination was assessed by the area under the ROC curve. Calibration was evaluated using LOESS-smoothed calibration plots of observed probability (0 or 1) versus estimated probability of the outcome.To assess the classification accuracy of particular models, those with a probability of being a case greater than 50% were

predicted to be cases, while those below 50% were predicted to be controls (Table 7.5). Predicted case status for a given model was then cross-tabulated with observed case status.

Analyses were run using SAS 9.4 (SAS Institute, Cary, NC). ROC curves were calculated using MATLAB. All figures were plotted in Graphpad Prsim 7 and Adobe Illustrator version 2015.

Case Group	Model	Positive Cases	Total Cases	Sensitivity (%)	Negative Controls	Total Controls	Specificity (%)	Overall Accuracy (%)
All	Early-Stage	124	141	88	195	199	98	94
All	Late-Stage	122	141	87	192	199	96	92
All	Full	127	141	90	194	199	97	94
Early-Stage	Early-Stage	74	91	81	195	199	98	93
Early-Stage	Full	77	91	85	194	199	97	93
Late-Stage	Late-Stage	50	50	100	199	199	100	100
Late-Stage	Full	50	50	100	199	199	100	100

Table 7. 5 Classification accuracy of antibody models for various sets of participants

Reference group was always All Controls. Predicted case status was case if model-specific predicted probability was at least 50%, otherwise predicted to be a control if predicted probability was less than 50%.

7.3 Results

Our multiplexed, ultra-sensitive Simoa assay detects the binding of IgG, IgM, and IgA against SARS-CoV-2 to four viral targets: spike protein, S1 subunit, Receptor Binding Domain (RBD), and nucleocapsid, enabling the quantification of 12 binding interactions. In this assay format, four types of dye-encoded paramagnetic beads are each coated with one of the four SARS-CoV-2 targets (Figure 7.5 and Methods section). We used this assay to measure the levels of IgG, IgM, and IgA against four viral targets in

plasma samples from patients who were classified as SARS-CoV-2 negative or positive by NP RT-PCR testing. We also measured these immunoglobulins in samples from patients with respiratory infections and from healthy individuals, collected before the start of the COVID-19 pandemic. We show that these serological assays detect anti-SARS-CoV-2 antibodies with high sensitivity and specificity at both early and late stages of infection.

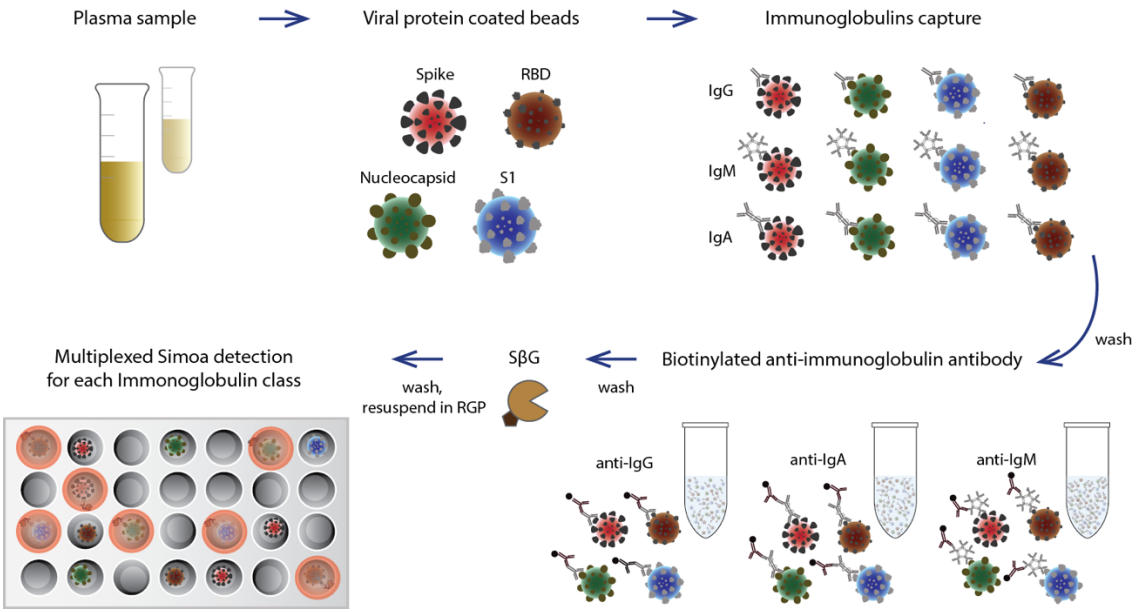

Figure 7. 5 Schematic illustration of the Simoa serological assay

Inactivated plasma is incubated with four types of dye-encoded beads that are each coupled to one of four viral targets (spike, S1, RBD, and nucleocapsid). IgG, IgA, and IgM antibodies specific to the SARS-CoV-2 targets bind to the viral antigen coated beads. After washing, beads are introduced to biotinylated anti-human immunoglobulin antibodies to label either IgG, IgM, or IgA in the different reactions. After additional washes, the enzyme streptavidin-β-galactosidase (SβG), is introduced. The beads are washed, resuspended in fluorogenic RGP and loaded into a 216,000 microwell array for multicolor imaging.

7.3.1 Detection of anti-SARS-CoV-2 antibodies in a training cohort

After testing a small discovery cohort in which our assay showed a clear separation between COVID-19 patients and the pre-pandemic cohort (Figure 7.6), we further validated our method using a training cohort of 472 samples that included pre-pandemic samples collected from patients with other viral respiratory infections prior to October 1, 2019. This cohort is a critical control for validating any SARS-CoV-2 serological assay, as cross-reactivity with other anti-viral antibodies is a likely source of false-positive results in SARS-CoV-2 serological tests. This training cohort consists of four groups: (1) Pre-pandemic plasma samples from healthy adults with no recorded respiratory infection in their medical history at the time of collection (100 individuals). (2) Pre-pandemic samples collected from adults with a documented respiratory infection (including bacterial and viral pneumonia) within the preceding two-month (100 individuals). (3) Samples from adults who tested positive for SARS-CoV-2 by NP RT-PCR (172 samples from 91 individuals taken at multiple timepoints). (4) Samples from symptomatic adults who tested negative for SARS-CoV-2 by NP RT-PCR (100 samples from 95 individuals taken at multiple timepoints).

Figure 7.7 shows IgG, IgM, and IgA normalized mean Average Enzymes per Bead (AEB) levels in SARS-CoV-2 NP RT-PCR positive samples, which were divided into four subgroups based on the number of days after symptom onset. In addition, Figure 7.7 shows the immunoglobulin levels in the pre-pandemic group and the SARS-CoV-2 NP RT-PCR negative group. All measurements were made in duplicate and the coefficient of variation (CV) values are plotted in the Figure 7.8. Normalization was performed using a standard set of calibrators in each run. These calibrators were produced by serially

diluting a large volume of blood from seroconverted patients. All four RT-PCR-confirmed SARS-CoV-2 positive subgroups (0-3 days, 4-7 days, 8-14 days, and >14 days after positive NP RT-PCR) showed higher median IgG, IgM, and IgA levels in SARS-CoV-2 positive samples compared to the pre-pandemic group (see Table 7.7 for all Mann-Whitney U test results). As in the discovery cohort, all twelve antigen-antibody isotype combinations showed an increase in median immunoglobulin levels over the course of the disease for those who tested positive for SARS-CoV-2 by NP RT-PCR but were not considered immunocompromised. Interestingly, some symptomatic individuals who tested negative for SARS-CoV-2 by NP RT-PCR displayed anti-SARS-CoV-2 antibody signals well above those in the pre-pandemic group; these may represent individuals infected with SARS-CoV-2 who falsely tested negative by RT-PCR.

Included in the SARS-CoV-2 validation cohort were four patients who were sampled longitudinally over the course of eight days (Figure 7.9). Within this group, the two patients who survived longer (patient 1: eventual recovery and patient 2: 20-day survival after COVID-19 diagnosis) had on average 10-100 times higher anti-SARS-CoV-2 antibody levels one week following infection compared to the other two patients (8- and 11-day survival after COVID-19 diagnosis). Furthermore, the only patient who ultimately recovered (patient 1) mounted a robust and diverse humoral immune response (characterized by a 10- to 100-fold increase in all immunoglobulin isotypes against all four viral antigens) within the first week of infection, while the immune response in patients who died from COVID-19 appeared substantially weaker in terms of absolute anti-SARS-CoV-2 antibody levels (patients 3 and 4) as well as the rate and diversity of antibody production (patients 2, 3, and 4). These observations suggest that the magnitude

and antibody specificity of the humoral immune response against SARS-CoV-2 may influence disease outcome and highlights the ability of the Simoa assay to profile the dynamics of this response at high resolution throughout the course of infection.

A. Simoa serological assay results using 1000x dilution

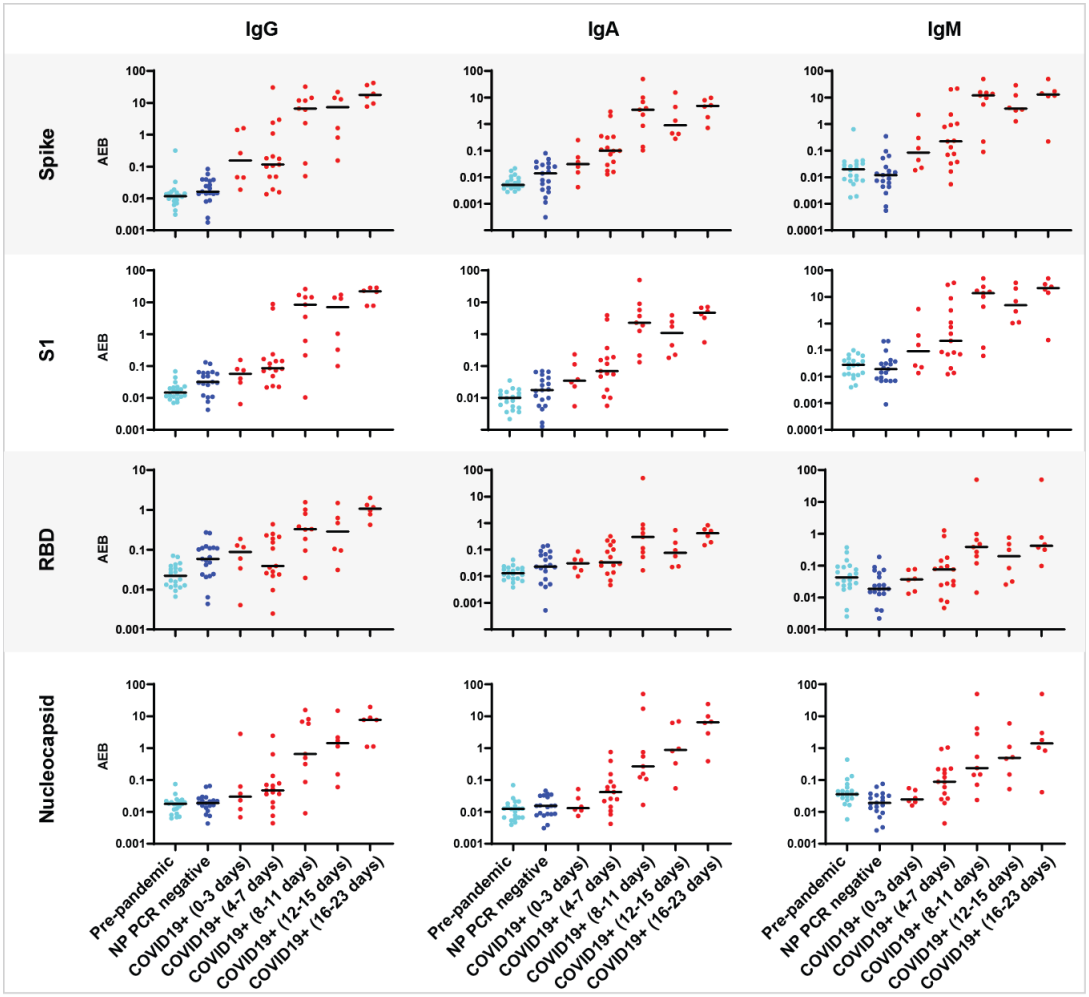

B. Simoa serological assay results using 4000x dilution

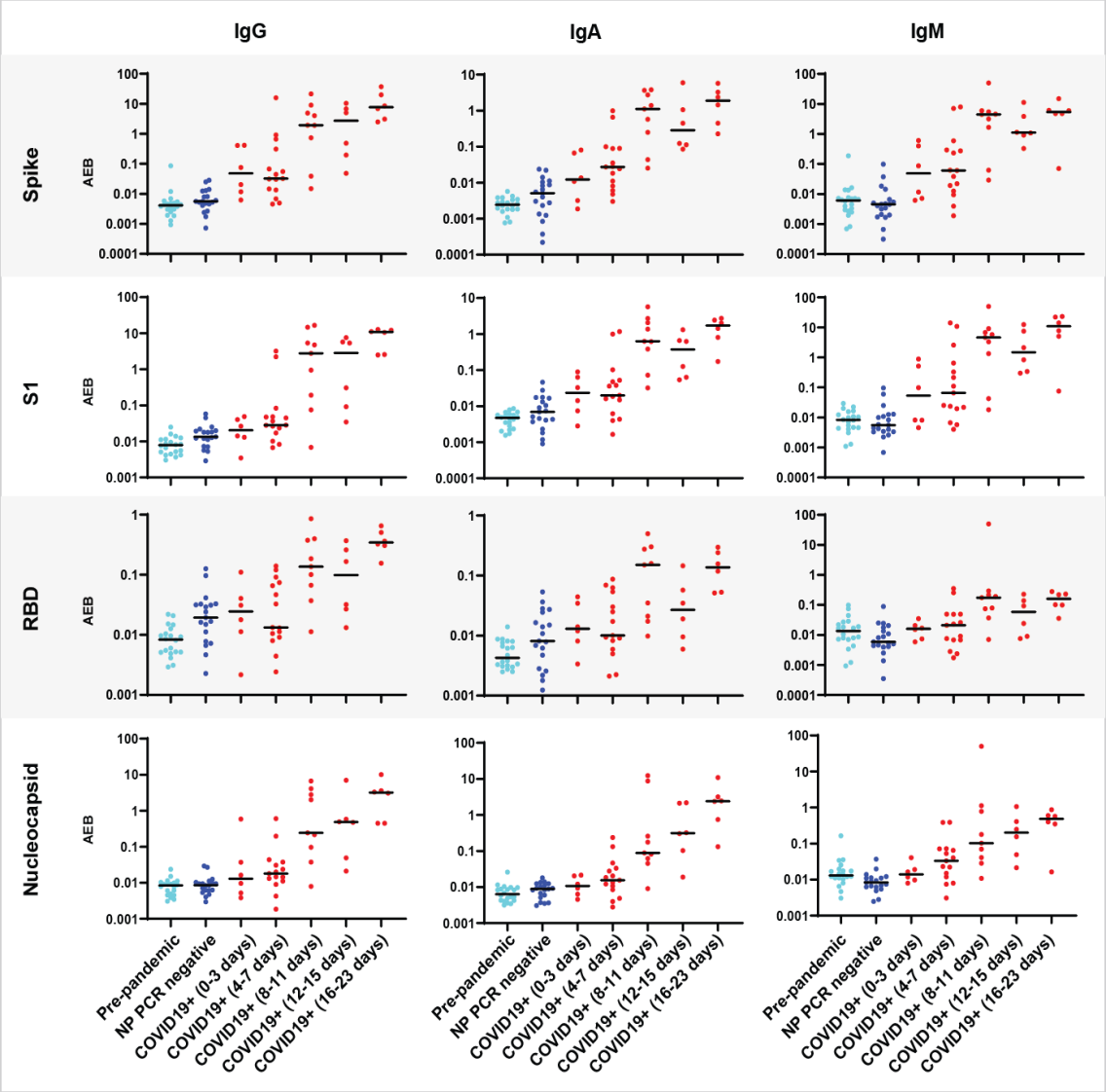

Figure 7. 6 Discovery cohort results

Simoa serological assay results for IgG, IgM, and IgA against the four viral targets: Spike, S1 subunit, Receptor Binding Domain, and Nucleocapsid for pre-pandemic samples (light blue, n=20), NP PCR negative samples (dark blue, n=19) and COVID-19 positive samples (red, n=21, two timepoints each). The COVID-19 positive samples were divided into five groups according to time since symptom onset. Black lines indicate the mean AEB (average enzyme per bead) value of each population.

In order to establish whether our assay detects seroconversion in SARS-CoV-2 infected patients, we initially tested 81 plasma samples from Massachusetts General Hospital

(MGH) in Boston, MA, USA. This sample cohort consisted of three groups: (1) patient plasma collected before the COVID-19 outbreak, (2) plasma collected during the pandemic from patients presenting with symptoms of SARS-CoV-2 at the Emergency Department (ED) with a negative NP RNA test, and (3) serial plasma samples collected during the pandemic from patients who had tested positive for SARS-CoV-2 infection and were hospitalized for COVID-19. Clinical characteristics of each patient group are shown in Table 7.6. Samples were measured at two different dilution factors and similar results were observed. Plasma samples measured at a 4000x dilution factor show that all four viral antigens elicit an IgG, IgM, and IgA immune response in COVID-19 positive patients. All twelve combinations (i.e. each of the four viral targets against each of the three immunoglobulins) show an overall increase in immunoglobulin levels over the course of the disease. Only one patient had a decrease in immunoglobulin levels; this person did not survive their infection with SARS-CoV-2. In addition, a separate patient who displayed low immunoglobulins levels at the late time point was on immunosuppressive medication.

Patient characteristics	**NP PCR Positive (n= 21)**	**NP PCR Negative (n=19)**	**Pre-pandemic control (n=20)**
Age (25^{th}, 75^{th} quartile)	58 (45, 72)	61 (41 ,75)	55 (33, 59)
Male (%)	20 (90.9)	11 (57.9)	8 (40)
Symptoms at presentation (%)			
Fever	16 (72.7)	4 (21)	NA
Cough	17 (77.2)	5 (26.3)	NA
SOB	15 (68.2)	5 (26.3)	NA
Sore throat	0 (0)	1 (5.3)	NA
Myalgia	4 (18.2)	2 (10.5)	NA
Risk Factors			
Diabetes	4 (18.2)	NA	NA
Immunosuppression	2 (9.1)	NA	NA
Lung disease	2 (9.1)	NA	NA
Heart disease	7 (31.8)	NA	NA
Clinical Outcome (%)			
Required Ventilation	12 (54.5)	NA	NA
Discharged from hospital	11 (0.5)	NA	NA
Still admitted	9 (45)	NA	NA
Death	2 (10)	NA	NA
CoV related death	2 (10)	NA	NA

Table 7. 6 Clinical characteristics of the discovery cohort

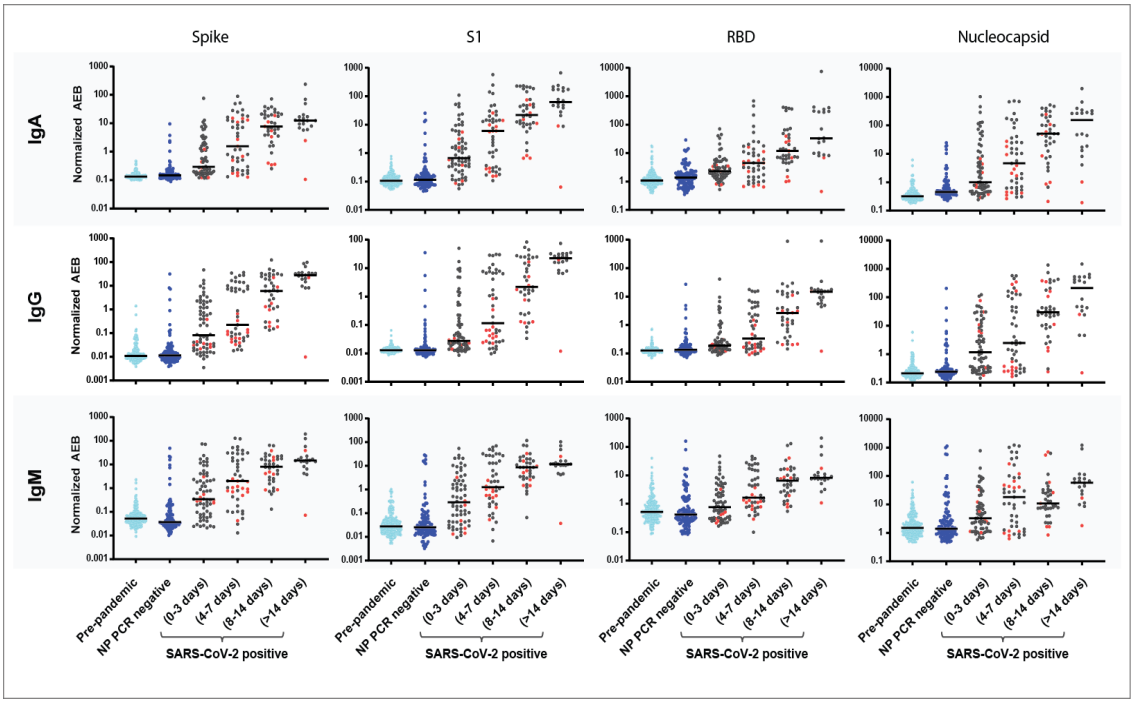

Figure 7. 7 Profiling seroconversion in COVID-19

Simoa serological assay results for IgG, IgM, and IgA against the four viral targets: spike, S1 subunit, RBD, and nucleocapsid for pre-pandemic samples (light blue, n=200), NP PCR negative samples (dark blue, n= 100) and SARS-CoV-2 positive samples (black, immunocompetent n=141 or red, immunosuppressed n=31). The SARS-CoV-2 positive samples were divided into four groups according to time since symptom onset. Black lines indicate the median normalized AEB (average enzyme per bead) value of each population.

To determine the ability of the serological Simoa assays to detect early seroconversion, we separated NP RT-PCR-confirmed COVID-19 patients into two subgroups based on whether samples were collected: (1) within the first week (classified as “early stage”) or (2) after the first week (classified as “late stage”) of a positive NP RT-PCR test. Our findings in the discovery cohort prompted us to exclude

immunocompromised individuals in order to build a more robust seroconversion classification model (31 timepoints, representing 10 patients). We assessed the performance of the Simoa assays using multivariate analyses comparing early-stage cases, late-stage cases, or all positive cases against the pre-pandemic group. A major advantage of this Simoa serological assay is that a single sample provides information on the antibody response to four viral targets, each across three immunoglobulin isotypes. This feature allowed us to train and validate a logistic regression model with all twelve parameters for each of the three case groups.

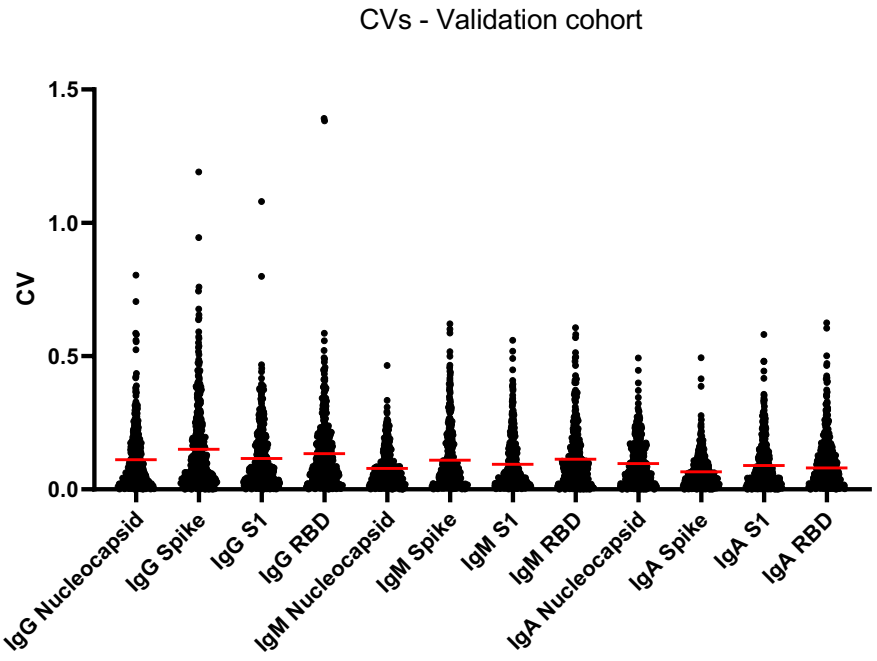

Figure 7. 8 CVs Validation Cohort

Coefficient of Variance (CV) of the duplicate measurements for each of the samples in the validation cohort. Each dot represents the CV of duplicate measurements for each of the 472 datapoints show in Figure 7.7. The red line indicates the median of the CVs. As can be seen all CVs were in an acceptable range indicating that accuracy of the measurements.

	IgG Nuc	IgG Spike	IgG S1	IgG RBD	IgM Nuc	IgM Spike	IgM S1	IgM RBD	IgA Nuc	IgA Spike	IgA S1	IgA RBD
0-3 days	****	****	****	****	****	****	****	*	****	****	****	****
4-7 days	****	****	****	****	****	****	****	****	****	****	****	****
8-14 days	****	****	****	****	****	****	****	****	****	****	****	****
>15 days	****	****	****	****	****	****	****	****	****	****	****	****

Table 7. 7 Mann-Whitney U test results

Mann-Whitney U test results for each of the four subgroups (0-3 days, 4-7 days, 8-14 days, and >14 days after positive NP RT-PCR) against the pre-pandemic control. All U-tests are two-tailed but do not correct for multiple comparisons.

In order to assess the possibility of classifying seroconversion using a smaller set of parameters, two additional models that included only a subset of the parameters, chosen carefully using cross validation were developed (Tables 7.8 & 7.9 and methods section). The final subset of markers selected were IgA S1, IgA nucleocapsid, IgG nucleocapsid, and IgG spike for the early stage model and IgA S1 for the late stage model.

Figure 7.10a shows the receiver operating characteristic (ROC) curves for each of the tested models for all cases, only early stage cases, and only late stage cases. For the early stage group, the area under the curve (AUC) was 0.9732 for the model using the full panel of markers and 0.9675 for the early stage model. The AUC is 1.00 for the late stage

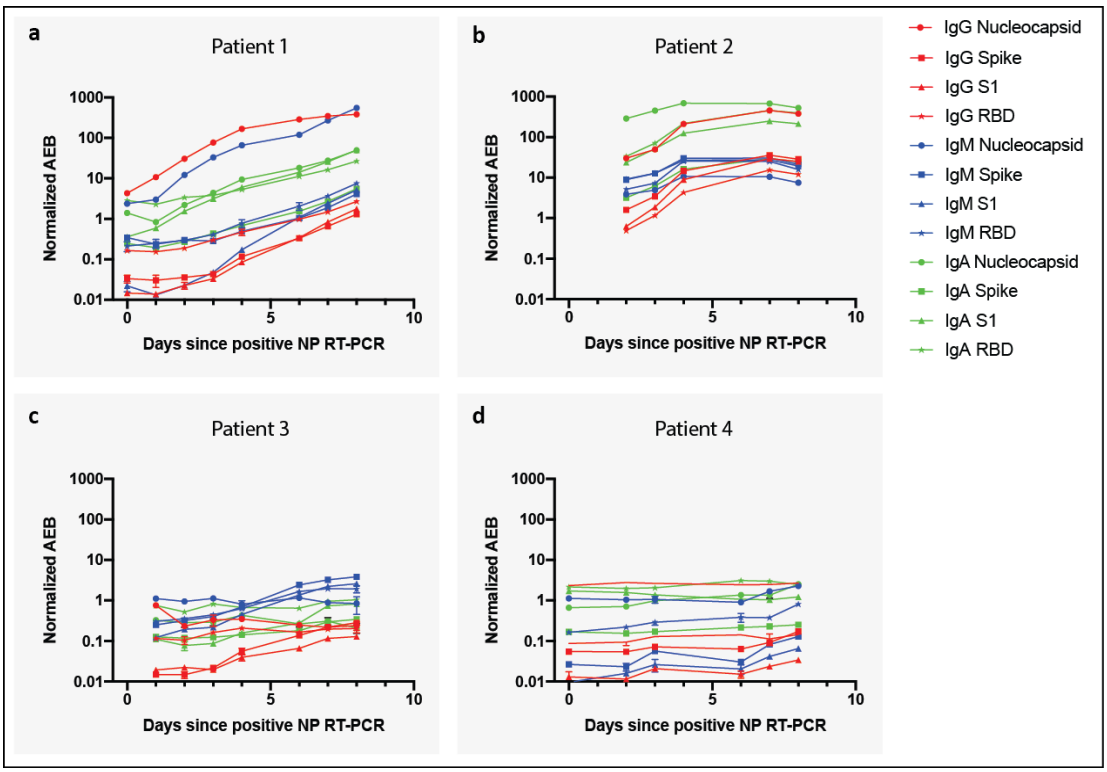

Figure 7. 9 Profiling the seroconversion time course in COVID-19

a. Patient 1 is a 67-year-old man who recovered 10 days after diagnosis with COVID-19.
b. Patient 2 was a 50-year-old man with multiple comorbidities who died from acute respiratory distress syndrome 20 days after diagnosis with COVID-19. He received Remdesivir from days 1-5.
c. Patient 3 was a 50-year-old man with pancytopenia and B-cell acute lymphoblastic leukemia. He died from acute respiratory distress syndrome eight days after diagnosis with COVID-19.
d. Patient 4 was an 89-year-old man who died from hypoxemic respiratory failure eight days after diagnosis with COVID-19. He received hydroxychloroquine from days 1-5.

group, for both the late stage model as well as the full panel of markers. Thus, the twelve-parameter model had a sensitivity of 81% with 100% specificity within the first week of a positive NP RT-PCR test and 100% sensitivity and specificity after the first week of a positive NP RT-PCR test. The lower sensitivity during the first week

	Fold 1		Fold 2		Fold 3		Fold 4		Fold 5	
	Antibody	**VI**	**Antibody**	**VI**	**Antibody**	**VI**	**Antibody**	**VI**	**Antibody**	**VI**
Training Set	IgA S1	100	IgA S1	100	IgA S1	100	IgA S1	100	IgG Spike	100
	IgA Nuc	96	IgG S1	89	IgG Nuc	71	IgG Spike	97	IgA RBD	95
	IgG Nuc	91	IgG Nuc	83	IgA Nuc	68	IgG Nuc	77	IgA S1	85
	IgG Spike	62	IgA Nuc	81	IgG RBD	61	IgA Nuc	56	IgG Nuc	83
	IgG S1	45	IgM RBD	0	IgG S1	52	IgA RBD	54	IgA Nuc	72
	IgG RBD	3	IgG Spike	0	IgA RBD	48	IgG RBD	0	IgG RBD	69
	IgM Spike	1	IgM S1	0	IgG Spike	33	IgG S1	0	IgM RBD	2
	IgM S1	0	IgA RBD	0	IgA Spike	0	IgA Spike	0	IgM Nuc	0
	IgA Spike	0							IgA Spike	0

AUC, All Test Sets Combined: 98% (95% CI 96%, 100%)

Table 7. 8 Five-fold cross validation of early-stage cases and all controls (n=290)

Each of the 290 participants in the cross validation was randomly assigned to one of five groups that included 58 participants. In each of five folds, one group of 58 was set aside as a fold-specific test set and the other four groups were combined to create a training set of 232 participants. For each fold, the model was identified through a backwards-selection process starting with predictors of all 12 antibodies measured. Variable importance rounded to the nearest integer. Variables that dropped out entirely had importance of 0.

undoubtedly stems from a delayed immune response in some individuals. Furthermore, we assessed whether the group of symptomatic patients who were SARS-CoV-2 negative by NP RT-PCR (all of whom were initially tested given clinical suspicion for COVID-19) produced antibodies against SARS-CoV-2. Interestingly, 14 out of 100 patients within this group were above the seroconversion threshold. It is possible that these patients with negative NP RT-PCR results were actually infected with SARS-CoV-2 and in the process of seroconversion.

	Fold 1		Fold 2		Fold 3		Fold 4		Fold 5	
	Antibody	**VI**	**Antibody**	**VI**	**Antibody**	**VI**	**Antibody**	**VI**	**Antibody**	**VI**
Training Set	IgM S1	100	IgA S1	100	IgA S1	100	IgA S1	100	IgA S1	100
	IgA Spike	41	IgA Spike	0			IgG S1	29		
	IgA S1	29					IgM S1	17		
	IgG RBD	5					IgA RBD	13		
	IgM Spike	-8					IgG Nuc	2		
	IgG Nuc	-10					IgG Spike	0		
							IgM RBD	0		

AUC, All Test Sets Combined: 100% (95% CI 100%, 100%)

Table 7. 9 Five-fold cross validation of late-stage cases and all controls (n=249)

Each of the 249 participants in the cross validation was randomly assigned to one of five groups that included 50 participants (one group had only 49 participants). In each of five folds, one group of 50 (or 49 in one fold) was set aside as a fold-specific test set and the other four groups were combined to create a training set of 199 participants (or 200 in one fold). For each fold, the model was identified through a backwards-selection process starting with predictors of all 12 antibodies measured. Variable importance rounded to the nearest integer. Variables that dropped out entirely had importance of 0.

7.3.2 Accuracy of Simoa Serological Assay in a blinded validation cohort

To further evaluate the classification accuracy of the three models, we tested a final independent set of blinded samples. This validation set consisted of 300 samples from: (1) 68 samples from 28 individuals who tested positive for SARS-CoV-2 using NP RT-PCR within the last 5-34 days, (2) 232 pre-pandemic controls all collected before October 1, 2019 including 132 patients with a documented respiratory infection (including bacterial and viral pneumonia) within the preceding 31 days, as well as 100 healthy individuals with no recorded history of viral respiratory infection. Figure 7.10b

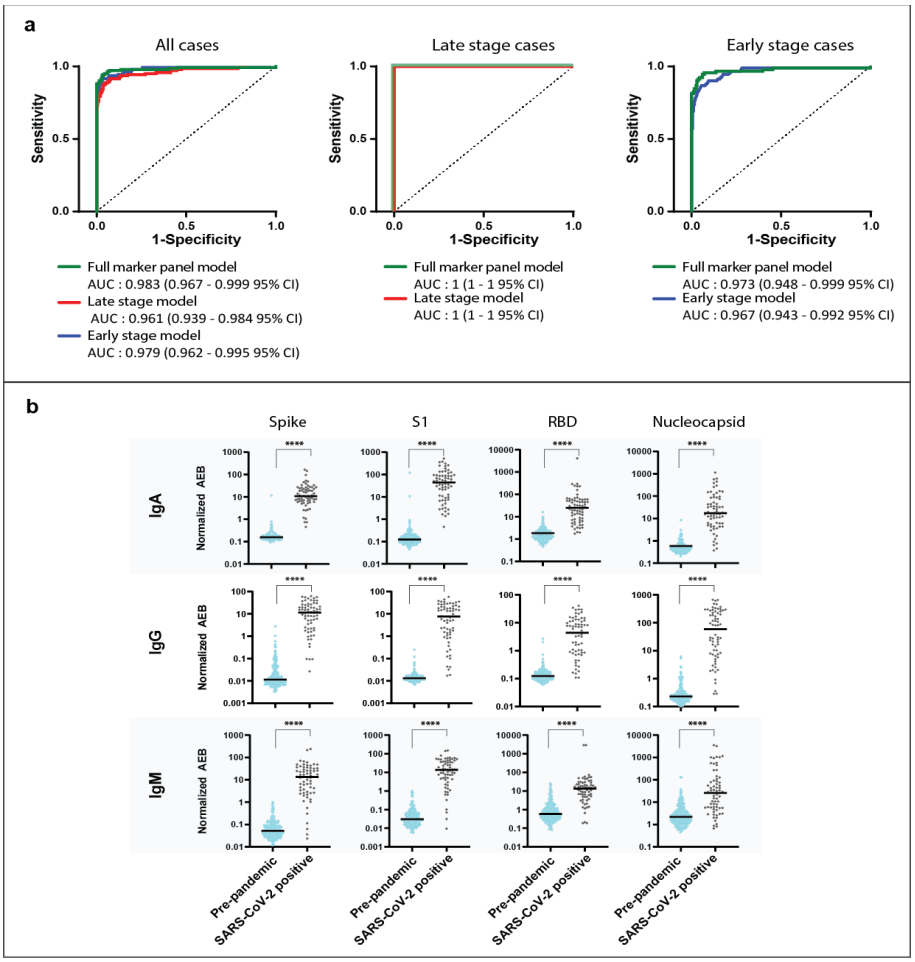

Figure 7. 10 Classification of COVID-19 using Simoa serological assays

a. Receiver Operating Characteristic (ROC) curves for early stage cases (first week after positive NP-PCR test, n=91) in the pre-pandemic cohort (n=199) using either the full marker panel model (green), or the early stage model (blue) (top), Receiver Operating Characteristic (ROC) curves for late stage cases (more than one week after positive NP-PCR test, n=50) in the pre-pandemic cohort (n=199) using either the full marker panel model (green), or the late stage model (red) (middle), Receiver Operating Characteristic (ROC) curves for all positive cases (n=141) in the pre-pandemic cohort (n=199) using either the full marker panel model (green), early stage model (blue), or the late stage model (red) (bottom). AUC values and 95% confidence intervals are shown for each graph.
b. Simoa serological assay results for IgG, IgM, and IgA against the four viral targets: spike, S1 subunit, RBD, and nucleocapsid for pre-pandemic samples (gray, n=232), NP PCR negative samples (light blue, n= 68). Asterisks indicate Mann-Whitney test results.

	Sensitivity	Specificity	PPV	NPV
Early stage model	99%	99%	97%	100%
Late stage model	99%	99%	96%	100%
Full marker panel model	100%	94%	83%	100%

Table 7. 10 Sensitivity, specificity, positive predictive value (PPV) and negative predictive value (NPV) for the validation set using the models created on the training set

shows IgG, IgM, and IgA normalized mean AEB levels in SARS-CoV-2 NP RT-PCR positive samples and the pre-pandemic controls. We classified these samples using the three models we trained on the training set (all cases versus all controls for each model). The signal threshold for a positive test result was determined based on the cutoff that yielded 100% specificity in the training set. Table 7.10 shows the sensitivity and specificity as well as the positive and negative predictive values for a population prevalence of 22.6%. The early model consisting of four parameters performed best with 99% sensitivity and specificity, followed by the late model which used only a single parameter. The full marker panel gave lower accuracy with 100% sensitivity and 94% specificity.

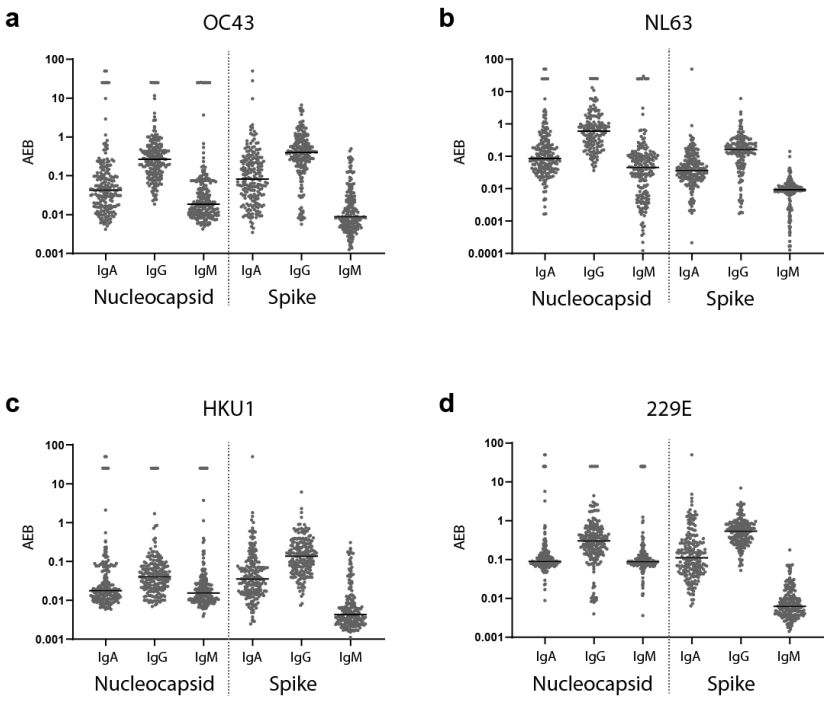

Figure 7. 11 Cross reactivity of the control samples with common human coronaviruses

In order to assess reactivity of pre-pandemic samples with other coronaviruses, which cause the common cold, we developed assays for Nucleocapsid and S1/RBD of the four common human coronaviruses: 229e (alpha coronavirus), NL63 (alpha coronavirus), OC43 (beta coronavirus), HKU1 (beta coronavirus). All antigens were purchased commercially from Sino Biological with the exception of the OC43 RBD, which was produced by the Aaron Schmidt Lab: 229E N Nucleocapsid (40640-V07E), NL63 Nucleocapsid (40641-V07E), OC43 Nucleocapsid (40643- V07E), HKU1 Nucleocapsid (40642-V07E), 229E S1 (40601-V08H), NL63 S1 (40600-V08H), HKU S1 (40602-V08H). We hypothesized that many of the individuals in our pre-pandemic cohort had likely experienced an infection with one or more of these coronaviruses, and we could therefore assess how antibodies to these assays correlated with activity in our SARS-CoV-2 serological assay. To accomplish this, we coupled two sets of multiplex beads, one for the N and one for the S1/RBD antigen. Each of the four multiplex beads (488, 647, 700 and 750) was coupled to the antigen from one of four common human coronaviruses: 229e, NL63, OC43 and HKU1. Using the same assay format as was used for the SARS-CoV-2 serological assay, we tested these two multiplexed assays using detection antibodies to IgG, IgM and IgA yielding 24 values per sample. We tested the 200 pre-pandemic samples for reactivity with these other coronaviruses. Several pre-pandemic control samples had high levels of antibodies for these common coronaviruses, likely indicating prior infection with these species.

7.4 Discussion

Quantitative and sensitive SARS-CoV-2 serological assays are necessary to address unmet needs in the clinical setting, epidemiological studies, as well as therapeutic and vaccine development. Using the Simoa technology, we developed a highly sensitive serological assay for detection of IgG, IgM, and IgA in COVID-19 patients against four SARS-CoV-2 targets in a high-throughput format. The ultra-sensitivity enables plasma to be diluted 4000x greatly reducing the degree of nonspecific circulating immunoglobulin binding. Furthermore, at this dilution factor our dynamic range spans four orders of magnitude, allowing for accurate quantification of the full range of disease from early to late stage. This dilution factor requires a minute sample size of less than 1μL plasma. Although our Simoa serological assay is a powerful analytical tool to understand the host immune response of the COVID-19 pandemic, it requires a specialized instrument that is not widely available.

While the clinical sensitivity of current SARS-CoV-2 NP RT-PCR tests is still under scrutiny, a recent meta-analysis concluded that up to 29% of initially negative tests are false negatives[148]. Therefore, it was crucial to establish a true negative sample group in addition to the negative NP RNA test group when evaluating our serological assay for the COVID-19 pandemic. Our analysis includes samples collected from U.S. adults presenting before October 1, 2019, and thus prior to the introduction of SARS-CoV-2 into the U.S and the first documented case in the world. This cohort included 100 patients presenting with a recent respiratory infection. Although we cannot comment on active non-SARS-CoV-2 coronoviridae infection nor previous exposure to such viruses among these individuals, such viruses are a common cause of respiratory tract infections, and

thus are likely present among the 100 pre-pandemic respiratory infection cohort. Our results suggest no significant cross reactivity of antibodies to our selected target antigens prior to the SARS-CoV-2 outbreak, indicating minimal cross reactivity among coronaviridae, or other respiratory viruses, in our assay.

In the training cohort, we were able to detect seroconversion as early as the day of the first positive NP-PCR test after symptom onset. This early detection of seroconversion is unmatched by current commercial tests or published laboratory data[146,152-162]. In a blinded validation set, which began at five days after a positive RT-PCR, both our one and four parameter models were 99% specific and sensitive while the 12 parameter model was 100% sensitive but only 94% specific. Additionally, the resolution of our method enables us to probe small variations in the immune response between patients and within a single patient.

While antibody testing is clearly key in curbing the COVID-19 pandemic, several limitations of antibody-based testing should be considered[168]. First, serological testing cannot replace NAATs for diagnosis of COVID-19 due to the later onset of seroconversion. Second, until a concrete link between levels of anti-SARS-CoV-2 antibodies and immunity from reinfection can be established, it is not possible to make clinical decisions or to develop public health policy based on this type of testing. Finally, even once a link between antibody levels and immunity can be established, it will need to be determined how long immunity lasts for proper clinical decision-making.

Despite these limitations, the Simoa serological platform provides a powerful analytical tool that will advance the understanding of host immunity to SARS-CoV-2 by enabling the analysis of the antibody response throughout the course of infection with

high resolution. We demonstrated this capability by profiling multiple immunoglobulin isotypes across a panel of SARS-CoV-2 antigens using blood samples collected at serial timepoints from individual COVID-19 patients. This type of comprehensive analysis of the immune response to SARS-CoV-2 can provide critical insights necessary for the development of therapeutics and vaccines. In future studies, we aim to utilize this new method to address important unanswered questions such as which specific antigen-antibody interactions are important and how they relate to long-term immunity, how long these antibodies remain in the bloodstream, and how community immunity can affect the spread of SARS-CoV-2.

7.5 Author Contributions

M.N., T.G., A.F.O., A.M.M., L.C., and D.R.W. conceived the approach. M.N., T.G., A.F.O. and A.M.M. performed the experiments, M.N., T.G., E.L.B, L.C. and R.L. analyzed the data, Y.C., J.Z., J.E.F., B.M.H., T.M.C., B.C., and A.G.S. produced and purified the antigens, R.C.C. and E.T.R. collected the samples for the discovery cohort, C.P.M. assisted in chart review for the training cohort, M.N., T.G., A.F.O., L.C., A.M.M. and D.R.W. co-wrote the paper. All authors were involved in designing experiments, reviewing and discussing data, and commented on the manuscript.

7.6 Competing interests

David Walt has a financial interest in Quanterix Corporation, a company that develops an ultra-sensitive digital immunoassay platform. He is an inventor of the Simoa technology, a founder of the company and also serves on its Board of Directors. Dr. Walt's interests were reviewed and are managed by BWH and Partners HealthCare in accordance

with their conflict of interest policies. The assays in this publication have been licensed by Brigham and Women's Hospital to Quanterix Corporation.

7.7 Supplementary Information is available for this paper

7.8 Data Availability Statement:

The authors declare that the data supporting the findings of this study are available within the paper and its Supplementary information files. Source data for the figures in this study are available in Mendeley data with the identifier: DOI: 10.17632/2f73pzdkr4.2[31]

Chapter 8: Bibliography

1 Arneric, S. P., Kern, V. D. & Stephenson, D. T. Regulatory-accepted drug development tools are needed to accelerate innovative CNS disease treatments. *Biochem Pharmacol* **151**, 291-306, doi:10.1016/j.bcp.2018.01.043 (2018).

2 Saijo, E. *et al.* Ultrasensitive RT-QuIC Seed Amplification Assays for Disease-Associated Tau, alpha-Synuclein, and Prion Aggregates. *Methods Mol Biol* **1873**, 19-37, doi:10.1007/978-1-4939-8820-4_2 (2019).

3 Fairfoul, G. *et al.* Alpha-synuclein RT-QuIC in the CSF of patients with alpha-synucleinopathies. *Ann Clin Transl Neurol* **3**, 812-818, doi:10.1002/acn3.338 (2016).

4 Costamagna, G., Andreoli, L., Corti, S. & Faravelli, I. iPSCs-Based Neural 3D Systems: A Multidimensional Approach for Disease Modeling and Drug Discovery. *Cells* **8**, doi:10.3390/cells8111438 (2019).

5 Makin, S. The amyloid hypothesis on trial. *Nature* **559**, S4-S7, doi:10.1038/d41586-018-05719-4 (2018).

6 Asher, S. & Priefer, R. Alzheimer's disease failed clinical trials. *Life Sci* **306**, 120861, doi:10.1016/j.lfs.2022.120861 (2022).

7 Hansson, O. Biomarkers for neurodegenerative diseases. *Nat Med* **27**, 954-963, doi:10.1038/s41591-021-01382-x (2021).

8 Lang, A. E. Clinical trials of disease-modifying therapies for neurodegenerative diseases: the challenges and the future. *Nat Med* **16**, 1223-1226, doi:10.1038/nm.2220 (2010).

9 Mustapic, M. *et al.* Plasma Extracellular Vesicles Enriched for Neuronal Origin: A Potential Window into Brain Pathologic Processes. *Front Neurosci* **11**, 278, doi:10.3389/fnins.2017.00278 (2017).

10 Doyle, L. M. & Wang, M. Z. Overview of Extracellular Vesicles, Their Origin, Composition, Purpose, and Methods for Exosome Isolation and Analysis. *Cells* **8**, doi:10.3390/cells8070727 (2019).

11 van Niel, G., D'Angelo, G. & Raposo, G. Shedding light on the cell biology of extracellular vesicles. *Nat Rev Mol Cell Biol* **19**, 213-228, doi:10.1038/nrm.2017.125 (2018).

12 de Jong, O. G. *et al.* Cellular stress conditions are reflected in the protein and RNA content of endothelial cell-derived exosomes. *J Extracell Vesicles* **1**, doi:10.3402/jev.v1i0.18396 (2012).

13 Eldh, M. *et al.* Exosomes communicate protective messages during oxidative stress; possible role of exosomal shuttle RNA. *PLoS One* **5**, e15353, doi:10.1371/journal.pone.0015353 (2010).

14 Rupert, D. L. M., Claudio, V., Lasser, C. & Bally, M. Methods for the physical characterization and quantification of extracellular vesicles in biological samples. *Biochim Biophys Acta Gen Subj* **1861**, 3164-3179, doi:10.1016/j.bbagen.2016.07.028 (2017).

15 Hartjes, T. A., Mytnyk, S., Jenster, G. W., van Steijn, V. & van Royen, M. E. Extracellular Vesicle Quantification and Characterization: Common Methods and Emerging Approaches. *Bioengineering (Basel)* **6**, doi:10.3390/bioengineering6010007 (2019).

16 Sidhom, K., Obi, P. O. & Saleem, A. A Review of Exosomal Isolation Methods: Is Size Exclusion Chromatography the Best Option? *Int J Mol Sci* **21**, doi:10.3390/ijms21186466 (2020).
17 Konoshenko, M. Y., Lekchnov, E. A., Vlassov, A. V. & Laktionov, P. P. Isolation of Extracellular Vesicles: General Methodologies and Latest Trends. *Biomed Res Int* **2018**, 8545347, doi:10.1155/2018/8545347 (2018).
18 Rissin, D. M. *et al.* Single-molecule enzyme-linked immunosorbent assay detects serum proteins at subfemtomolar concentrations. *Nat Biotechnol* **28**, 595-599, doi:10.1038/nbt.1641 (2010).
19 Rivnak, A. J. *et al.* A fully-automated, six-plex single molecule immunoassay for measuring cytokines in blood. *J Immunol Methods* **424**, 20-27, doi:10.1016/j.jim.2015.04.017 (2015).
20 Arvanitis, C. D., Ferraro, G. B. & Jain, R. K. The blood-brain barrier and blood-tumour barrier in brain tumours and metastases. *Nat Rev Cancer* **20**, 26-41, doi:10.1038/s41568-019-0205-x (2020).
21 Sweeney, M. D., Sagare, A. P. & Zlokovic, B. V. Blood-brain barrier breakdown in Alzheimer disease and other neurodegenerative disorders. *Nat Rev Neurol* **14**, 133-150, doi:10.1038/nrneurol.2017.188 (2018).
22 Matsumoto, J., Stewart, T., Banks, W. A. & Zhang, J. The Transport Mechanism of Extracellular Vesicles at the Blood-Brain Barrier. *Curr Pharm Des* **23**, 6206-6214, doi:10.2174/1381612823666170913164738 (2017).
23 Ramos-Zaldivar, H. M. *et al.* Extracellular vesicles through the blood-brain barrier: a review. *Fluids Barriers CNS* **19**, 60, doi:10.1186/s12987-022-00359-3 (2022).
24 Alvarez-Erviti, L. *et al.* Delivery of siRNA to the mouse brain by systemic injection of targeted exosomes. *Nat Biotechnol* **29**, 341-345, doi:10.1038/nbt.1807 (2011).
25 Bala, S. *et al.* Biodistribution and function of extracellular miRNA-155 in mice. *Sci Rep* **5**, 10721, doi:10.1038/srep10721 (2015).
26 Skog, J. *et al.* Glioblastoma microvesicles transport RNA and proteins that promote tumour growth and provide diagnostic biomarkers. *Nat Cell Biol* **10**, 1470-1476, doi:10.1038/ncb1800 (2008).
27 Garcia-Romero, N. *et al.* DNA sequences within glioma-derived extracellular vesicles can cross the intact blood-brain barrier and be detected in peripheral blood of patients. *Oncotarget* **8**, 1416-1428, doi:10.18632/oncotarget.13635 (2017).
28 Shi, M. *et al.* Plasma exosomal alpha-synuclein is likely CNS-derived and increased in Parkinson's disease. *Acta Neuropathol* **128**, 639-650, doi:10.1007/s00401-014-1314-y (2014).
29 Fiandaca, M. S. *et al.* Identification of preclinical Alzheimer's disease by a profile of pathogenic proteins in neurally derived blood exosomes: A case-control study. *Alzheimers Dement* **11**, 600-607 e601, doi:10.1016/j.jalz.2014.06.008 (2015).
30 Kapogiannis, D. *et al.* Dysfunctionally phosphorylated type 1 insulin receptor substrate in neural-derived blood exosomes of preclinical Alzheimer's disease. *FASEB J* **29**, 589-596, doi:10.1096/fj.14-262048 (2015).

31 Shi, M. *et al.* CNS tau efflux via exosomes is likely increased in Parkinson's disease but not in Alzheimer's disease. *Alzheimers Dement* **12**, 1125-1131, doi:10.1016/j.jalz.2016.04.003 (2016).
32 Sun, B., Dalvi, P., Abadjian, L., Tang, N. & Pulliam, L. Blood neuron-derived exosomes as biomarkers of cognitive impairment in HIV. *AIDS* **31**, F9-F17, doi:10.1097/QAD.0000000000001595 (2017).
33 Goetzl, E. J., Schwartz, J. B., Abner, E. L., Jicha, G. A. & Kapogiannis, D. High complement levels in astrocyte-derived exosomes of Alzheimer disease. *Ann Neurol* **83**, 544-552, doi:10.1002/ana.25172 (2018).
34 Goetzl, E. J. *et al.* Decreased synaptic proteins in neuronal exosomes of frontotemporal dementia and Alzheimer's disease. *FASEB J* **30**, 4141-4148, doi:10.1096/fj.201600816R (2016).
35 Guix, F. X. *et al.* Detection of Aggregation-Competent Tau in Neuron-Derived Extracellular Vesicles. *Int J Mol Sci* **19**, doi:10.3390/ijms19030663 (2018).
36 Goetzl, E. J. *et al.* Low neural exosomal levels of cellular survival factors in Alzheimer's disease. *Ann Clin Transl Neurol* **2**, 769-773, doi:10.1002/acn3.211 (2015).
37 Suire, C. N. *et al.* Walking speed decline in older adults is associated with elevated pro-BDNF in plasma extracellular vesicles. *Exp Gerontol* **98**, 209-216, doi:10.1016/j.exger.2017.08.024 (2017).
38 Abner, E. L., Jicha, G. A., Shaw, L. M., Trojanowski, J. Q. & Goetzl, E. J. Plasma neuronal exosomal levels of Alzheimer's disease biomarkers in normal aging. *Ann Clin Transl Neurol* **3**, 399-403, doi:10.1002/acn3.309 (2016).
39 Gill, J. *et al.* Higher exosomal tau, amyloid-beta 42 and IL-10 are associated with mild TBIs and chronic symptoms in military personnel. *Brain Inj* **32**, 1277-1284, doi:10.1080/02699052.2018.1471738 (2018).
40 Goetzl, E. J. *et al.* Altered levels of plasma neuron-derived exosomes and their cargo proteins characterize acute and chronic mild traumatic brain injury. *FASEB J* **33**, 5082-5088, doi:10.1096/fj.201802319R (2019).
41 Goetzl, L., Darbinian, N. & Goetzl, E. J. Novel window on early human neurodevelopment via fetal exosomes in maternal blood. *Ann Clin Transl Neurol* **3**, 381-385, doi:10.1002/acn3.296 (2016).
42 Hamlett, E. D. *et al.* Neuronal exosomes reveal Alzheimer's disease biomarkers in Down syndrome. *Alzheimers Dement* **13**, 541-549, doi:10.1016/j.jalz.2016.08.012 (2017).
43 Patterson, S. A., Deep, G. & Brinkley, T. E. Detection of the receptor for advanced glycation endproducts in neuronally-derived exosomes in plasma. *Biochem Biophys Res Commun* **500**, 892-896, doi:10.1016/j.bbrc.2018.04.181 (2018).
44 Winston, C. N. *et al.* Prediction of conversion from mild cognitive impairment to dementia with neuronally derived blood exosome protein profile. *Alzheimers Dement (Amst)* **3**, 63-72, doi:10.1016/j.dadm.2016.04.001 (2016).
45 Winston, C. N., Goetzl, E. J., Baker, L. D., Vitiello, M. V. & Rissman, R. A. Growth Hormone-Releasing Hormone Modulation of Neuronal Exosome Biomarkers in Mild Cognitive Impairment. *J Alzheimers Dis* **66**, 971-981, doi:10.3233/JAD-180302 (2018).

46 Zhao, Z. H. *et al.* Increased DJ-1 and alpha-Synuclein in Plasma Neural-Derived Exosomes as Potential Markers for Parkinson's Disease. *Front Aging Neurosci* **10**, 438, doi:10.3389/fnagi.2018.00438 (2018).
47 Kapogiannis, D. *et al.* Association of Extracellular Vesicle Biomarkers With Alzheimer Disease in the Baltimore Longitudinal Study of Aging. *JAMA Neurol*, doi:10.1001/jamaneurol.2019.2462 (2019).
48 Chawla, S. *et al.* Extracellular vesicles reveal abnormalities in neuronal iron metabolism in restless legs syndrome. *Sleep* **42**, doi:10.1093/sleep/zsz079 (2019).
49 Goetzl, E. J., Peltz, C. B., Mustapic, M., Kapogiannis, D. & Yaffe, K. Neuron-Derived Plasma Exosome Proteins after Remote Traumatic Brain Injury. *J Neurotrauma*, doi:10.1089/neu.2019.6711 (2019).
50 Mullins, R. J., Mustapic, M., Goetzl, E. J. & Kapogiannis, D. Exosomal biomarkers of brain insulin resistance associated with regional atrophy in Alzheimer's disease. *Hum Brain Mapp* **38**, 1933-1940, doi:10.1002/hbm.23494 (2017).
51 Hiramoto, J. S. *et al.* Acute Insulin Resistance and Rapid Alterations in Neuronal Derived Blood Exosome Concentration After Branched Endovascular Aortic Aneurysm Repair. *Eur J Vasc Endovasc Surg*, doi:10.1016/j.ejvs.2019.10.007 (2019).
52 Winston, C. N. *et al.* Assessing Neuronal and Astrocyte Derived Exosomes From Individuals With Mild Traumatic Brain Injury for Markers of Neurodegeneration and Cytotoxic Activity. *Front Neurosci* **13**, 1005, doi:10.3389/fnins.2019.01005 (2019).
53 Cha, D. J. *et al.* miR-212 and miR-132 Are Downregulated in Neurally Derived Plasma Exosomes of Alzheimer's Patients. *Front Neurosci* **13**, 1208, doi:10.3389/fnins.2019.01208 (2019).
54 Rani, K. *et al.* Neuronal exosomes in saliva of Parkinson's disease patients: A pilot study. *Parkinsonism Relat Disord* **67**, 21-23, doi:10.1016/j.parkreldis.2019.09.008 (2019).
55 Si, X. *et al.* Central Nervous System-Derived Exosomal Alpha-Synuclein in Serum May Be a Biomarker in Parkinson's Disease. *Neuroscience* **413**, 308-316, doi:10.1016/j.neuroscience.2019.05.015 (2019).
56 Agliardi, C. *et al.* SNAP-25 in Serum Is Carried by Exosomes of Neuronal Origin and Is a Potential Biomarker of Alzheimer's Disease. *Mol Neurobiol* **56**, 5792-5798, doi:10.1007/s12035-019-1501-x (2019).
57 Jia, L. *et al.* Concordance between the assessment of Abeta42, T-tau, and P-T181-tau in peripheral blood neuronal-derived exosomes and cerebrospinal fluid. *Alzheimers Dement* **15**, 1071-1080, doi:10.1016/j.jalz.2019.05.002 (2019).
58 Kapogiannis, D. *et al.* Insulin-signaling abnormalities in drug-naive first-episode schizophrenia: Transduction protein analyses in extracellular vesicles of putative neuronal origin. *Eur Psychiatry* **62**, 124-129, doi:10.1016/j.eurpsy.2019.08.012 (2019).
59 Katsu, M. *et al.* MicroRNA expression profiles of neuron-derived extracellular vesicles in plasma from patients with amyotrophic lateral sclerosis. *Neurosci Lett* **708**, 134176, doi:10.1016/j.neulet.2019.03.048 (2019).

60 Sun, B., Fernandes, N. & Pulliam, L. Profile of neuronal exosomes in HIV cognitive impairment exposes sex differences. *AIDS* **33**, 1683-1692, doi:10.1097/QAD.0000000000002272 (2019).
61 Athauda, D. *et al.* Utility of Neuronal-Derived Exosomes to Examine Molecular Mechanisms That Affect Motor Function in Patients With Parkinson Disease: A Secondary Analysis of the Exenatide-PD Trial. *JAMA Neurol* **76**, 420-429, doi:10.1001/jamaneurol.2018.4304 (2019).
62 Madhu, L. N. *et al.* Neuroinflammation in Gulf War Illness is linked with HMGB1 and complement activation, which can be discerned from brain-derived extracellular vesicles in the blood. *Brain Behav Immun* **81**, 430-443, doi:10.1016/j.bbi.2019.06.040 (2019).
63 Jiang, C. *et al.* Serum neuronal exosomes predict and differentiate Parkinson's disease from atypical parkinsonism. *J Neurol Neurosurg Psychiatry*, doi:10.1136/jnnp-2019-322588 (2020).
64 Kodidela, S. *et al.* Circulatory Astrocyte and Neuronal EVs as Potential Biomarkers of Neurological Dysfunction in HIV-Infected Subjects and Alcohol/Tobacco Users. *Diagnostics (Basel)* **10**, doi:10.3390/diagnostics10060349 (2020).
65 Mansur, R. B. *et al.* Extracellular Vesicle Biomarkers Reveal Inhibition of Neuroinflammation by Infliximab in Association with Antidepressant Response in Adults with Bipolar Depression. *Cells* **9**, doi:10.3390/cells9040895 (2020).
66 Zou, J. *et al.* Long Noncoding RNA POU3F3 and alpha-Synuclein in Plasma L1CAM Exosomes Combined with beta-Glucocerebrosidase Activity: Potential Predictors of Parkinson's Disease. *Neurotherapeutics*, doi:10.1007/s13311-020-00842-5 (2020).
67 Yuan, Y. *et al.* Exosome alpha-Synuclein Release in Plasma May be Associated With Postoperative Delirium in Hip Fracture Patients. *Front Aging Neurosci* **12**, 67, doi:10.3389/fnagi.2020.00067 (2020).
68 Niu, M. *et al.* A longitudinal study on alpha-synuclein in plasma neuronal exosomes as a biomarker for Parkinson's disease development and progression. *Eur J Neurol* **27**, 967-974, doi:10.1111/ene.14208 (2020).
69 Banack, S. A., Dunlop, R. A. & Cox, P. A. An miRNA fingerprint using neural-enriched extracellular vesicles from blood plasma: towards a biomarker for amyotrophic lateral sclerosis/motor neuron disease. *Open Biol* **10**, 200116, doi:10.1098/rsob.200116 (2020).
70 Bhargava, P. *et al.* Synaptic and complement markers in extracellular vesicles in multiple sclerosis. *Mult Scler*, 1352458520924590, doi:10.1177/1352458520924590 (2020).
71 Nogueras-Ortiz, C. J. *et al.* Astrocyte- and Neuron-Derived Extracellular Vesicles from Alzheimer's Disease Patients Effect Complement-Mediated Neurotoxicity. *Cells* **9**, doi:10.3390/cells9071618 (2020).
72 Ko, J. *et al.* Multi-Dimensional Mapping of Brain-Derived Extracellular Vesicle MicroRNA Biomarker for Traumatic Brain Injury Diagnostics. *J Neurotrauma*, doi:10.1089/neu.2018.6220 (2019).

73 Ko, J. *et al.* Diagnosis of traumatic brain injury using miRNA signatures in nanomagnetically isolated brain-derived extracellular vesicles. *Lab Chip* **18**, 3617-3630, doi:10.1039/c8lc00672e (2018).
74 Ko, J. *et al.* Smartphone-enabled optofluidic exosome diagnostic for concussion recovery. *Sci Rep* **6**, 31215, doi:10.1038/srep31215 (2016).
75 Bhargava, P. *et al.* Synaptic and complement markers in extracellular vesicles in multiple sclerosis. *Mult Scler* **27**, 509-518, doi:10.1177/1352458520924590 (2021).
76 Serpente, M. *et al.* MiRNA Profiling in Plasma Neural-Derived Small Extracellular Vesicles from Patients with Alzheimer's Disease. *Cells* **9**, doi:10.3390/cells9061443 (2020).
77 Hornung, S., Dutta, S. & Bitan, G. CNS-Derived Blood Exosomes as a Promising Source of Biomarkers: Opportunities and Challenges. *Front Mol Neurosci* **13**, 38, doi:10.3389/fnmol.2020.00038 (2020).
78 Yu, Z. *et al.* Reduced oligodendrocyte exosome secretion in multiple system atrophy involves SNARE dysfunction. *Brain* **143**, 1780-1797, doi:10.1093/brain/awaa110 (2020).
79 Goetzl, E. J. *et al.* Cargo proteins of plasma astrocyte-derived exosomes in Alzheimer's disease. *FASEB J* **30**, 3853-3859, doi:10.1096/fj.201600756R (2016).
80 Hirshman, B. R., Kras, R. T., Akers, J. C., Carter, B. S. & Chen, C. C. Extracellular Vesicles in Molecular Diagnostics: An Overview with a Focus on CNS Diseases. *Advances in clinical chemistry* **76**, 37-53, doi:10.1016/bs.acc.2016.05.005 (2016).
81 Tkach, M., Kowal, J. & Thery, C. Why the need and how to approach the functional diversity of extracellular vesicles. *Philosophical transactions of the Royal Society of London. Series B, Biological sciences* **373**, doi:10.1098/rstb.2016.0479 (2018).
82 Shao, H. *et al.* New Technologies for Analysis of Extracellular Vesicles. *Chemical reviews* **118**, 1917-1950, doi:10.1021/acs.chemrev.7b00534 (2018).
83 Coumans, F. A. W. *et al.* Methodological Guidelines to Study Extracellular Vesicles. *Circulation research* **120**, 1632-1648, doi:10.1161/circresaha.117.309417 (2017).
84 Simonsen, J. B. What Are We Looking At? Extracellular Vesicles, Lipoproteins, or Both? *Circulation research* **121**, 920-922, doi:10.1161/circresaha.117.311767 (2017).
85 Sodar, B. W. *et al.* Low-density lipoprotein mimics blood plasma-derived exosomes and microvesicles during isolation and detection. *Scientific reports* **6**, 24316, doi:10.1038/srep24316 (2016).
86 Osteikoetxea, X. *et al.* Improved characterization of EV preparations based on protein to lipid ratio and lipid properties. *PloS one* **10**, e0121184, doi:10.1371/journal.pone.0121184 (2015).
87 Visnovitz, T. *et al.* An improved 96 well plate format lipid quantification assay for standardisation of experiments with extracellular vesicles. *Journal of extracellular vesicles* **8**, 1565263, doi:10.1080/20013078.2019.1565263 (2019).

88 Norman, M. *et al.* L1CAM is not Associated with Extracellular Vesicles in Human Cerebrospinal Fluid or Plasma. *bioRxiv*, 2020.2008.2012.247833, doi:10.1101/2020.08.12.247833 (2020).
89 Cohen, L. & Walt, D. R. Highly Sensitive and Multiplexed Protein Measurements. *Chemical reviews* **119**, 293-321, doi:10.1021/acs.chemrev.8b00257 (2019).
90 Coumans, F. A. W., Gool, E. L. & Nieuwland, R. Bulk immunoassays for analysis of extracellular vesicles. *Platelets* **28**, 242-248, doi:10.1080/09537104.2016.1265926 (2017).
91 Cohen, L. *et al.* Single Molecule Protein Detection with Attomolar Sensitivity Using Droplet Digital Enzyme-Linked Immunosorbent Assay. *ACS nano* **14**, 9491-9501, doi:10.1021/acsnano.0c02378 (2020).
92 Maley, A. M., Garden, P. M. & Walt, D. R. Simplified Digital Enzyme-Linked Immunosorbent Assay Using Tyramide Signal Amplification and Fibrin Hydrogels. *ACS Sens*, doi:10.1021/acssensors.0c01661 (2020).
93 Wu, C., Garden, P. M. & Walt, D. R. Ultrasensitive Detection of Attomolar Protein Concentrations by Dropcast Single Molecule Assays. *J Am Chem Soc* **142**, 12314-12323, doi:10.1021/jacs.0c04331 (2020).
94 Karimi, N. *et al.* Detailed analysis of the plasma extracellular vesicle proteome after separation from lipoproteins. *Cellular and molecular life sciences : CMLS* **75**, 2873-2886, doi:10.1007/s00018-018-2773-4 (2018).
95 Zhang, X., Borg, E. G. F., Liaci, A. M., Vos, H. R. & Stoorvogel, W. A novel three step protocol to isolate extracellular vesicles from plasma or cell culture medium with both high yield and purity. *Journal of extracellular vesicles* **9**, 1791450, doi:10.1080/20013078.2020.1791450 (2020).
96 Lobb, R. J. *et al.* Optimized exosome isolation protocol for cell culture supernatant and human plasma. *J Extracell Vesicles* **4**, 27031, doi:10.3402/jev.v4.27031 (2015).
97 Helwa, I. *et al.* A Comparative Study of Serum Exosome Isolation Using Differential Ultracentrifugation and Three Commercial Reagents. *PloS one* **12**, e0170628, doi:10.1371/journal.pone.0170628 (2017).
98 Baranyai, T. *et al.* Isolation of Exosomes from Blood Plasma: Qualitative and Quantitative Comparison of Ultracentrifugation and Size Exclusion Chromatography Methods. *PloS one* **10**, e0145686, doi:10.1371/journal.pone.0145686 (2015).
99 Soares Martins, T., Catita, J., Martins Rosa, I., O, A. B. d. C. E. S. & Henriques, A. G. Exosome isolation from distinct biofluids using precipitation and column-based approaches. *PloS one* **13**, e0198820, doi:10.1371/journal.pone.0198820 (2018).
100 An, M., Wu, J., Zhu, J. & Lubman, D. M. Comparison of an Optimized Ultracentrifugation Method versus Size-Exclusion Chromatography for Isolation of Exosomes from Human Serum. *Journal of proteome research* **17**, 3599-3605, doi:10.1021/acs.jproteome.8b00479 (2018).
101 Stranska, R. *et al.* Comparison of membrane affinity-based method with size-exclusion chromatography for isolation of exosome-like vesicles from human

plasma. *Journal of translational medicine* **16**, 1, doi:10.1186/s12967-017-1374-6 (2018).
102 Diaz, G. *et al.* Protein Digestion, Ultrafiltration, and Size Exclusion Chromatography to Optimize the Isolation of Exosomes from Human Blood Plasma and Serum. *Journal of visualized experiments : JoVE*, doi:10.3791/57467 (2018).
103 Kalra, H. *et al.* Comparative proteomics evaluation of plasma exosome isolation techniques and assessment of the stability of exosomes in normal human blood plasma. *Proteomics* **13**, 3354-3364, doi:10.1002/pmic.201300282 (2013).
104 Serrano-Pertierra, E. *et al.* Characterization of Plasma-Derived Extracellular Vesicles Isolated by Different Methods: A Comparison Study. *Bioengineering (Basel, Switzerland)* **6**, doi:10.3390/bioengineering6010008 (2019).
105 Gamez-Valero, A. *et al.* Size-Exclusion Chromatography-based isolation minimally alters Extracellular Vesicles' characteristics compared to precipitating agents. *Scientific reports* **6**, 33641, doi:10.1038/srep33641 (2016).
106 Takov, K., Yellon, D. M. & Davidson, S. M. Comparison of small extracellular vesicles isolated from plasma by ultracentrifugation or size-exclusion chromatography: yield, purity and functional potential. *Journal of extracellular vesicles* **8**, 1560809, doi:10.1080/20013078.2018.1560809 (2019).
107 Ludwig, N., Whiteside, T. L. & Reichert, T. E. Challenges in Exosome Isolation and Analysis in Health and Disease. *International journal of molecular sciences* **20**, doi:10.3390/ijms20194684 (2019).
108 Wei, P. *et al.* Plasma extracellular vesicles detected by Single Molecule array technology as a liquid biopsy for colorectal cancer. *Journal of extracellular vesicles* **9**, 1809765, doi:10.1080/20013078.2020.1809765 (2020).
109 Osteikoetxea, X. *et al.* Differential detergent sensitivity of extracellular vesicle subpopulations. *Organic & biomolecular chemistry* **13**, 9775-9782, doi:10.1039/c5ob01451d (2015).
110 Raposo, G. & Stoorvogel, W. Extracellular vesicles: exosomes, microvesicles, and friends. *J Cell Biol* **200**, 373-383, doi:10.1083/jcb.201211138 (2013).
111 Hlavin, M. L. & Lemmon, V. Molecular structure and functional testing of human L1CAM: an interspecies comparison. *Genomics* **11**, 416-423, doi:10.1016/0888-7543(91)90150-d (1991).
112 Angiolini, F. *et al.* A novel L1CAM isoform with angiogenic activity generated by NOVA2-mediated alternative splicing. *Elife* **8**, doi:10.7554/eLife.44305 (2019).
113 Kowal, E. J. K., Ter-Ovanesyan, D., Regev, A. & Church, G. M. Extracellular Vesicle Isolation and Analysis by Western Blotting. *Methods Mol Biol* **1660**, 143-152, doi:10.1007/978-1-4939-7253-1_12 (2017).
114 Shevchenko, A., Wilm, M., Vorm, O. & Mann, M. Mass spectrometric sequencing of proteins silver-stained polyacrylamide gels. *Anal Chem* **68**, 850-858, doi:10.1021/ac950914h (1996).
115 Peng, J. & Gygi, S. P. Proteomics: the move to mixtures. *J Mass Spectrom* **36**, 1083-1091, doi:10.1002/jms.229 (2001).

116 Eng, J. K., McCormack, A. L. & Yates, J. R. An approach to correlate tandem mass spectral data of peptides with amino acid sequences in a protein database. *J Am Soc Mass Spectrom* **5**, 976-989, doi:10.1016/1044-0305(94)80016-2 (1994).
117 Busskamp, V. *et al.* Rapid neurogenesis through transcriptional activation in human stem cells. *Mol Syst Biol* **10**, 760, doi:10.15252/msb.20145508 (2014).
118 Thorvaldsdottir, H., Robinson, J. T. & Mesirov, J. P. Integrative Genomics Viewer (IGV): high-performance genomics data visualization and exploration. *Brief Bioinform* **14**, 178-192, doi:10.1093/bib/bbs017 (2013).
119 Mechtersheimer, S. *et al.* Ectodomain shedding of L1 adhesion molecule promotes cell migration by autocrine binding to integrins. *J Cell Biol* **155**, 661-673, doi:10.1083/jcb.200101099 (2001).
120 Zhou, L. *et al.* The neural cell adhesion molecules L1 and CHL1 are cleaved by BACE1 protease in vivo. *J Biol Chem* **287**, 25927-25940, doi:10.1074/jbc.M112.377465 (2012).
121 Thompson, A. G. *et al.* Extracellular vesicles in neurodegenerative disease - pathogenesis to biomarkers. *Nat Rev Neurol* **12**, 346-357, doi:10.1038/nrneurol.2016.68 (2016).
122 Shi, M., Sheng, L., Stewart, T., Zabetian, C. P. & Zhang, J. New windows into the brain: Central nervous system-derived extracellular vesicles in blood. *Prog Neurobiol* **175**, 96-106, doi:10.1016/j.pneurobio.2019.01.005 (2019).
123 Mustapic, M., Tran, J., Craft, S. & Kapogiannis, D. Extracellular Vesicle Biomarkers Track Cognitive Changes Following Intranasal Insulin in Alzheimer's Disease. *J Alzheimers Dis* **69**, 489-498, doi:10.3233/JAD-180578 (2019).
124 Badhwar, A. & Haqqani, A. S. Biomarker potential of brain-secreted extracellular vesicles in blood in Alzheimer's disease. *Alzheimers Dement (Amst)* **12**, e12001, doi:10.1002/dad2.12001 (2020).
125 Sjostedt, E. *et al.* An atlas of the protein-coding genes in the human, pig, and mouse brain. *Science* **367**, doi:10.1126/science.aay5947 (2020).
126 Gower, H. J. *et al.* Alternative splicing generates a secreted form of N-CAM in muscle and brain. *Cell* **55**, 955-964, doi:10.1016/0092-8674(88)90241-3 (1988).
127 Boyle, L. H., Traherne, J. A., Plotnek, G., Ward, R. & Trowsdale, J. Splice variation in the cytoplasmic domains of myelin oligodendrocyte glycoprotein affects its cellular localisation and transport. *J Neurochem* **102**, 1853-1862, doi:10.1111/j.1471-4159.2007.04687.x (2007).
128 *GTEx Portal*, <http://www.gtexportal.org/home/> (2022).
129 Zhang, Y. *et al.* An RNA-sequencing transcriptome and splicing database of glia, neurons, and vascular cells of the cerebral cortex. *J Neurosci* **34**, 11929-11947, doi:10.1523/JNEUROSCI.1860-14.2014 (2014).
130 Zhang, Y. *et al.* Purification and Characterization of Progenitor and Mature Human Astrocytes Reveals Transcriptional and Functional Differences with Mouse. *Neuron* **89**, 37-53, doi:10.1016/j.neuron.2015.11.013 (2016).
131 Esposito, C. *et al.* Structures and micelle locations of the nonlipidated and lipidated C-terminal membrane anchor of 2',3'-cyclic nucleotide-3'-phosphodiesterase. *Biochemistry* **47**, 308-319, doi:10.1021/bi701474t (2008).

132 Verrier, J. D., Kochanek, P. M. & Jackson, E. K. Schwann Cells Metabolize Extracellular 2',3'-cAMP to 2'-AMP. *J Pharmacol Exp Ther* **354**, 175-183, doi:10.1124/jpet.115.225219 (2015).
133 Kamil, K., Yazid, M. D., Idrus, R. B. H., Das, S. & Kumar, J. Peripheral Demyelinating Diseases: From Biology to Translational Medicine. *Front Neurol* **10**, 87, doi:10.3389/fneur.2019.00087 (2019).
134 Trombetta, J. J. *et al.* Preparation of Single-Cell RNA-Seq Libraries for Next Generation Sequencing. *Curr Protoc Mol Biol* **107**, 4 22 21-24 22 17, doi:10.1002/0471142727.mb0422s107 (2014).
135 Zhou, Z. *et al.* Extracellular RNA in a single droplet of human serum reflects physiologic and disease states. *Proc Natl Acad Sci U S A* **116**, 19200-19208, doi:10.1073/pnas.1908252116 (2019).
136 Fujiwara, H. *et al.* alpha-Synuclein is phosphorylated in synucleinopathy lesions. *Nat Cell Biol* **4**, 160-164, doi:10.1038/ncb748 (2002).
137 Iqbal, K., Liu, F. & Gong, C. X. Tau and neurodegenerative disease: the story so far. *Nat Rev Neurol* **12**, 15-27, doi:10.1038/nrneurol.2015.225 (2016).
138 Wang, Y. *et al.* Phosphorylated alpha-synuclein in Parkinson's disease. *Sci Transl Med* **4**, 121ra120, doi:10.1126/scitranslmed.3002566 (2012).
139 Srivastava, A. *et al.* Identifying the bond responsible for the fluorescence modulation in an amyloid fibril sensor. *Chemistry* **16**, 9257-9263, doi:10.1002/chem.200902968 (2010).
140 Soderbom, G. Status and future directions of clinical trials in Parkinson's disease. *Int Rev Neurobiol* **154**, 153-188, doi:10.1016/bs.irn.2020.02.009 (2020).
141 Paolini Paoletti, F., Gaetani, L. & Parnetti, L. The Challenge of Disease-Modifying Therapies in Parkinson's Disease: Role of CSF Biomarkers. *Biomolecules* **10**, doi:10.3390/biom10020335 (2020).
142 Wild, D. *The immunoassay handbook : theory and applications of ligand binding, ELISA, and related techniques*. 4th edn, (Elsevier, 2013).
143 Zhou, P. *et al.* A pneumonia outbreak associated with a new coronavirus of probable bat origin. *Nature* **579**, 270-273, doi:10.1038/s41586-020-2012-7 (2020).
144 Vashist, S. K. In Vitro Diagnostic Assays for COVID-19: Recent Advances and Emerging Trends. *Diagnostics (Basel)* **10**, doi:10.3390/diagnostics10040202 (2020).
145 Cascella, M., Rajnik, M., Cuomo, A., Dulebohn, S. C. & Di Napoli, R. in *StatPearls* (2020).
146 Liu, R. *et al.* The comparative superiority of IgM-IgG antibody test to real-time reverse transcriptase PCR detection for SARS-CoV-2 infection diagnosis. *medRxiv*, 2020.2003.2028.20045765, doi:10.1101/2020.03.28.20045765 (2020).
147 Bullis, S. S. M., Crothers, J. W., Wayne, S. & Hale, A. J. A Cautionary Tale of False-Negative Nasopharyngeal COVID-19 Testing. *IDCases*, e00791, doi:10.1016/j.idcr.2020.e00791 (2020).
148 Arevalo-Rodriguez, I. *et al.* FALSE-NEGATIVE RESULTS OF INITIAL RT-PCR ASSAYS FOR COVID-19: A SYSTEMATIC REVIEW. *medRxiv*, 2020.2004.2016.20066787, doi:10.1101/2020.04.16.20066787 (2020).

149 Berenger, B. M., Fonseca, K., Schneider, A. R., Hu, J. & Zelyas, N. Sensitivity of Nasopharyngeal, Nasal and Throat Swab for the Detection of SARS-CoV-2. *medRxiv*, 2020.2005.2005.20084889, doi:10.1101/2020.05.05.20084889 (2020).
150 Long, Q. X. *et al.* Antibody responses to SARS-CoV-2 in patients with COVID-19. *Nat Med*, doi:10.1038/s41591-020-0897-1 (2020).
151 Lipsitch, M., Kahn, R. & Mina, M. J. Antibody testing will enhance the power and accuracy of COVID-19-prevention trials. *Nat Med*, doi:10.1038/s41591-020-0887-3 (2020).
152 Pan, Y. *et al.* Serological immunochromatographic approach in diagnosis with SARS-CoV-2 infected COVID-19 patients. *J Infect*, doi:10.1016/j.jinf.2020.03.051 (2020).
153 Okba, N. M. A. *et al.* Severe Acute Respiratory Syndrome Coronavirus 2-Specific Antibody Responses in Coronavirus Disease 2019 Patients. *Emerg Infect Dis* **26**, doi:10.3201/eid2607.200841 (2020).
154 Liu, L., Liu, W., Wang, S. & Zheng, S. A preliminary study on serological assay for severe acute respiratory syndrome coronavirus 2 (SARS-CoV-2) in 238 admitted hospital patients. *medRxiv*, 2020.2003.2006.20031856, doi:10.1101/2020.03.06.20031856 (2020).
155 Zhao, J. *et al.* Antibody responses to SARS-CoV-2 in patients of novel coronavirus disease 2019. *Clin Infect Dis*, doi:10.1093/cid/ciaa344 (2020).
156 Amanat, F. *et al.* A serological assay to detect SARS-CoV-2 seroconversion in humans. *medRxiv*, 2020.2003.2017.20037713, doi:10.1101/2020.03.17.20037713 (2020).
157 Wang, Z. *et al.* Elevated serum IgM levels indicate poor outcome in patients with coronavirus disease 2019 pneumonia: A retrospective case-control study. *medRxiv*, 2020.2003.2022.20041285, doi:10.1101/2020.03.22.20041285 (2020).
158 Lin, D. *et al.* Evaluations of serological test in the diagnosis of 2019 novel coronavirus (SARS-CoV-2) infections during the COVID-19 outbreak. *medRxiv*, 2020.2003.2027.20045153, doi:10.1101/2020.03.27.20045153 (2020).
159 Lou, B. *et al.* Serology characteristics of SARS-CoV-2 infection since the exposure and post symptoms onset. *medRxiv*, 2020.2003.2023.20041707, doi:10.1101/2020.03.23.20041707 (2020).
160 Guo, L. *et al.* Profiling Early Humoral Response to Diagnose Novel Coronavirus Disease (COVID-19). *Clin Infect Dis*, doi:10.1093/cid/ciaa310 (2020).
161 Saijo, M. *et al.* Recombinant nucleocapsid protein-based IgG enzyme-linked immunosorbent assay for the serological diagnosis of SARS. *J Virol Methods* **125**, 181-186, doi:10.1016/j.jviromet.2005.01.028 (2005).
162 Long, Q.-x. *et al.* Antibody responses to SARS-CoV-2 in COVID-19 patients: the perspective application of serological tests in clinical practice. *medRxiv*, 2020.2003.2018.20038018, doi:10.1101/2020.03.18.20038018 (2020).
163 Cohen, L. & Walt, D. R. Single-Molecule Arrays for Protein and Nucleic Acid Analysis. *Annu Rev Anal Chem (Palo Alto Calif)* **10**, 345-363, doi:10.1146/annurev-anchem-061516-045340 (2017).
164 Wu, C., Maley, A. M. & Walt, D. R. Single-molecule measurements in microwells for clinical applications. *Crit Rev Clin Lab Sci*, 1-21, doi:10.1080/10408363.2019.1700903 (2019).

165 Kovacs, J. M. *et al.* HIV-1 envelope trimer elicits more potent neutralizing antibody responses than monomeric gp120. *Proc Natl Acad Sci U S A* **109**, 12111-12116, doi:10.1073/pnas.1204533109 (2012).
166 Shaik, M. M. *et al.* Structural basis of coreceptor recognition by HIV-1 envelope spike. *Nature* **565**, 318-323, doi:10.1038/s41586-018-0804-9 (2019).
167 Cohen, L. & Walt, D. R. Evaluation of Antibody Biotinylation Approaches for Enhanced Sensitivity of Single Molecule Array (Simoa) Immunoassays. *Bioconjug Chem* **29**, 3452-3458, doi:10.1021/acs.bioconjchem.8b00601 (2018).
168 Weinstein, M. C., Freedberg, K. A., Hyle, E. P. & Paltiel, A. D. Waiting for Certainty on Covid-19 Antibody Tests - At What Cost? *N Engl J Med*, doi:10.1056/NEJMp2017739 (2020).